NDOT Research Report

Report No. 047-08-803

TREE CROWN MORTALITY ASSOCIATED WITH ROADS IN THE LAKE TAHOE BASIN: A REMOTE SENSING APPROACH

September 2011

Nevada Department of Transportation

1263 South Stewart Street

Carson City, NV 89712

Disclaimer

This work was sponsored by the Nevada Department of Transportation. The contents of this report reflect the views of the authors, who are responsible for the facts and the accuracy of the data presented herein. The contents do not necessarily reflect the official views or policies of the State of Nevada at the time of publication. This report does not constitute a standard, specification, or regulation.

TECHNICAL REPORT DOCUMENTATION PAGE

1. Report No. 047-08-803	2. Government Accession No.	3. Recipient's Catalog No.
4. Title and Subtitle Tree Crown Mortality Associated with Roads in the Lake Tahoe Basin: A Remote Sensing Approach		5. Report Date September 2011 6. Performing Organization Code
7. Author(s) Peter J. Weisberg, Robert S. Nowak, Yuanchao Fan		8. Performing Organization Report No.
9. Performing Organization Name and Address University of Nevada, Reno 1000 Valley Road Reno, NV 89557-2040		10. Work Unit No. 11. Contract or Grant No. P047-08-803
12. Sponsoring Agency Name and Address Nevada Department of Transportation 1263 South Stewart Street Carson City, NV 89712		13. Type of Report and Period Covered Final Report 03/05/2008-09/30/2011 14. Sponsoring Agency Code
15. Supplementary Notes		

16. Abstract

Tree crown mortality along highways in the Lake Tahoe Basin has been a concern for decades. Increased tree damage near roads is believed to be associated with de-icing compounds used to increase driving safety during winter. Field studies have concluded that de-icing salts applied on the roads are a potential factor for roadside tree crown mortality, but the spatial pattern and temporal trend of de-icing salt damage has not been quantitatively measured. Remote sensing provides a means for assessing potential road-related effects on tree crown mortality in a large-scale and long-term context. This study used remote sensing methods to quantify tree crown mortality, expressed as declines in leaf area index (LAI) at the scale of 4-m pixels for the Nevada portion of the Lake Tahoe Basin, and at the scale of 30-m pixels for the whole basin. The mortality data together with data for salt application, precipitation, traffic, and topography were then statistically analyzed to reveal the component of crown mortality that is road-related. Several relatively novel approaches were developed in this study for processing remote sensing images and utilizing GIS data. A clear trend of increasing mortality with increasing aerial deposition of de-icing salt was revealed in the fine-scale spatial analysis. Aerial deposition played a major role in mortality within 30m of the road and its overall effect was much stronger than that of flow accumulation, although the effect zone of the latter had the potential to extend to 100m from road. The temporal analysis revealed that mortality was strongly correlated with salt application from 1990 to 2010. De-icing salt effects (as suggested by a trend of increased crown mortality closer to the roads) were most distinct in wet years when de-icing salt application was high and other damaging factors were weak. The spatial analysis and temporal analysis together provided convincing evidence that de-icing salt was a significant factor for roadside tree crown mortality. In order to protect the roadside forests from degradation and preserve their aesthetic value to drivers, road management should decrease the amount of de-icing salt used as much as possible, plant salt-resistant species within the 0–30m salt-susceptible zones, and plant taller trees on concave slopes in order to minimize the aerial deposition effect.

17. Key Words	18. Distribution Statement
Tree crown mortality, crown mortality, de-icing salts, Lake Tahoe, Lake Tahoe Basin, remote sensing, salt resistance, roadway salt, de-icing salt effect	No restrictions. This document is available through the: National Technical Information Service Springfield, VA 22161

19. Security Classif. (of this report)	20. Security Classif. (of this page)	21. No. of Pages	22. Price
Unclassified	Unclassified	160	$100,000.00

Form DOT F 1700.7 (8-72) Reproduction of completed page authorized

Tree crown mortality associated with roads in the Lake Tahoe Basin: a remote sensing approach

Agreement No. P047-08-803

Final Technical Report to the Nevada Department of Transportation

September, 2011

Peter J. Weisberg

Robert S. Nowak

Yuanchao Fan

Department of Natural Resources and Environmental Science

University of Nevada – Reno

Background and Overview

Tree crown mortality along highways in the Lake Tahoe Basin has been a concern for decades. Increased tree damage near roads is believed to be associated with de-icing compounds used to increase driving safety during winter. Several field studies have concluded that de-icing salts applied on the roads are a potential factor for roadside tree crown mortality, but monitoring approaches based solely on field sampling only provide information for a particular set of sample sites at discrete time intervals. An efficient large-scale approach is needed that can be repeatedly applied to retrieve historical dynamics, or to monitor future occurrence, of road-related tree crown mortality. Remote sensing provides a means for assessing potential road-related effects on tree crown mortality in a large-scale and long-term context.

We thus conducted a study using remote sensing methods to quantify tree crown mortality, expressed as declines in leaf area index (LAI) at the scale of 4-m pixels for the Nevada portion of the Lake Tahoe Basin, and at the scale of 30-m pixels for the whole Basin. The mortality data together with data for salt application, precipitation, traffic, and topography (Figure 1) were statistically analyzed to reveal the component of crown mortality that was road-related.

The study had two components: methodological development and application. The methodological component addressed remote sensing approaches for deriving tree crown mortality, whereas the application component investigated the influences of road-related effects on tree crown mortality by both spatial and temporal analyses. Specifically, we had the following four objectives:

1) Investigate remote sensing methods for robust processing of remotely sensed data and efficient monitoring of tree crown mortality;

2) Statistically model the effects of de-icing salt on tree crown mortality via two mechanisms: (a) aerial deposition and flow accumulation (uptake of dissolved salts from groundwater) at the fine-scale (6-m resolution), and (b) the interaction effect of distance from road and roadside topography on tree crown mortality over broad scales (30-m resolution);

3) Evaluate how trends in road-related mortality have changed over the last two decades, with special attention to the effects of de-icing salt application and precipitation;

4) Statistically isolate the component of tree crown mortality that is road-related (e.g. de-icing salt damage) from other mortality agents through the complementary evidence from spatial analyses and temporal analyses.

Several relatively novel remote sensing approaches were developed in this study. The Sun-Crown-Sensor (+C) topographic correction model was developed to correct radiometric distortion caused by terrain variability in forest images. LiDAR data were utilized to aid in orthorectifying IKONOS images and extracting projected tree crown shapes from complex earth surface features. Several vegetation indices were compared and the normalized difference vegetation index (NDVI) was consistently found to be the best indicator for leaf area index (LAI), a proxy for the amount of green leaf mass in tree crowns. Interannual change in LAI was found to be appropriate sensitive measure of tree crown mortality, defined as the loss of

photosynthetic material in tree crowns. A field dataset of LAI was collected at 30 plots comprising 120 subplots of 30×30m, which was used to calibrate and transform remote sensing data into LAI that is physically meaningful. A dataset of yearly change detection results as measured by quantitative LAI change was generated using Landsat TM images from 1990 to 2010 (e.g. Figure 2). A 4-year change in LAI from 2005 to 2009 was generated using a pair of IKONOS images (Figure 3). Mortality was defined based on LAI change thresholds. Remote sensing methodological details are available in Yuanchao Fan's M.S. Thesis (Fan 2011).

IKONOS derived mortality was used in fine-scale spatial analysis (Figure 4) to assess the effects of de-icing salt through aerial deposition and flow accumulation mechanisms, which were represented by two spatial proxy variables constructed using high-resolution topographical data. Landsat derived mortality was used in both broad-scale spatial analysis and long-term temporal analysis (Figure 5). The broad-scale spatial analysis was used to confirm IKONOS fine-scale spatial analysis results. The long-term temporal analysis was aimed to provide evidence of how roadside mortality was related to variation in de-icing salt application in the past two decades.

This study demonstrated the utility of applying remote sensing techniques to detect road-related effects on tree crown mortality. Principal results are listed below, divided into the following categories: Remote Sensing Methodology for Monitoring Tree Crown Mortality; Spatial Patterns of Tree Crown Mortality Associated with De-icing Salt; Temporal Patterns of Tree Crown Mortality Associated with De-icing Salt and Precipitation; Implications for Monitoring and Management. For more detailed information about methods, results and discussions, including relevant tables, maps and figures, refer to Fan (2011).

Remote Sensing Methodology for Monitoring Tree Crown Mortality

1) **A new topographic correction method was developed (i.e.the Sun-Crown-Sensor (+C) method).** This is a refinement of existing methods, correcting radiometric distortions caused by terrain in high-resolution satellite images of landscapes dominated by forests, and where tree crowns are the key feature of interest.

2) **LiDAR proved its utility as important ancillary data in this study.** The high resolution and geometric accuracy of LiDAR DEM data greatly improved the accuracy in orthorectifying IKONOS images. An approach was developed for creating a projected tree crown mask from LiDAR DEM and DSM data that helped focus the analyses on tree crowns.

3) **The recommended method for quantifying tree crown mortality in the Lake Tahoe Basin**, using either Landsat or IKONOS imagery, is to first estimate leaf area index (LAI) from NDVI, and then to use the change in LAI among successive years as the tree crown mortality indicator (Figures 2 and 3). Quantitative change detection by LAI differencing using multispectral images was successful in quantifying tree crown mortality, which was then analyzed statistically to describe the likely effects of de-icing salts.

4) **Qualitative change detection by classifying multispectral images was not able to detect the spectral signature of de-icing salt damage on tree crowns directly**. Hyperspectral remote sensing data are needed in future studies if the objective is to

directly classify tree crown mortality caused by de-icing salt. If successful, this would allow improved separation of de-icing salt effects from other tree mortality agents within the remote sensing context.

Spatial Patterns of Tree Crown Mortality Associated with De-icing Salt

1) **The IKONOS analysis showed that tree crown mortality was positively associated with the proxy variable for aerial deposition** (Figure 6, Table 1). **This indicates that the effects of slope steepness, slope curvature and distance from road interact to influence the probability of de-icing salt mortality in a predictable manner.** This effect was greatest within 30 m of the road edge, but was still present when considering all locations within 100 m of the road edge. Interpretation of aerial deposition effects can be partitioned into the relative influences of slope steepness, distance from road and path curvature, i.e., the three components of the aerial deposition proxy variable. For example, a tree on a 60° slope was 1.57 times (95% CI: 1.14 to 2.16) more likely to be damaged relative to a tree on a 30° slope, at 12m from the road. On a 45° slope, a tree at 12m distance from the road was 1.22 times (95% CI: 1.06 to 1.40) more likely to be damaged relative to a tree that was 24m from the road. At 24m from the road, a tree on a concave slope was 2.47 times (95% CI: 1.31 to 4.67) more likely to have mortality than an identical tree on a convex slope. These calculations refer to the particular geometry portrayed in Figure 6, but can be recalculated for any topographic configuration.

2) **Tree crown mortality was only weakly associated with the proxy variable for flow accumulation** (Figure 7, Table 1), confirming results of earlier field studies that the primary mechanism for de-icing salt related tree crown mortality is due to airborne spray rather than plant uptake of salts from the soil solution.

3) The spatial analysis using Landsat TM images revealed that a decreasing trend of mortality with increasing distance from roads mainly existed within 60m of the road and was greatest within 30m of the road (Figure 8). The odds of mortality for the 0–30m zone where the trees are more likely to have de-icing salt contact was estimated to be 2.6 times the odds of mortality for the more distant 30–60m zone, although there was high variability around this relationship (95% CI: 1.1 times to 6.2 times). The effect of every 10-m increase in distance from the road edge was estimated to be a 26.5% (95% *CI*: 4.8% to 43.2%) decrease in probability of mortality, when considering the population of forested pixels within 60m of the road.

Temporal Patterns of Tree Crown Mortality Associated with De-icing Salt and Precipitation

1) **A comparison between years with high salt application (1993 – 1999) and years with low salt application (2003 – 2009) using two pairs of Landsat TM images revealed strong effects of road proximity on tree crown mortality in the years of high salt application.** This pattern was amplified because the time period of greater salt application generally experienced more favorable conditions for tree growth, due to favorable water balance associated with increased snowpack. This increased the contrast between areas of high tree crown mortality near roads and low tree crown mortality away

from roads. When de-icing salt application was low and its effects were negligible in dry years, other damaging agents more strongly influenced the spatial pattern of tree crown mortality throughout the Basin and road-related effects were less distinct (Figure 2).

2) **The long-term temporal analysis (1990 – 2010) using Landsat TM images provided convincing evidence of de-icing salt effects on the probability of mortality.** Mortality increased with increasing amount of salt applied (Figure 9a). This effect was greatest when considering a lagged effect of one year: the previous year's winter de-icing salt application was most strongly correlated with the subsequent year's growing season tree crown mortality. The influence of salt application on tree crown mortality was dependent on precipitation, such that the probability of observing tree crown mortality for trees within 60m of the road increased with increasing salt application for wet years, but actually decreased slightly (or had negligible effect) with increasing salt application for dry years (Figure 9, Table 3). This modeled interaction effect suggests that wetter conditions may be needed for transport of de-icing salt to tree crowns through the mechanism of aerosol spray, although further studies are needed to better understand the details of how airborne spray from de-icing salts interacts with conifer foliage.

3) **The temporal analysis with salt application data complemented the spatial analysis in confirming that both the spatial pattern and temporal pattern of tree crown mortality near the roads were largely related to de-icing salt.**

Implications for Monitoring and Management

Monitoring:

1) Landsat TM images are a useful remote sensing data source for retrieving historical road-related forest mortality and monitoring future tree health change in a broad-scale and long-term context. This has the advantage of being free, relatively easy to process, and collected at regular 16-day intervals, allowing for analysis of tree crown mortality across a continuous time series or an array of time periods. Disadvantages include a lack of spatial precision, and uncertainty concerning whether compatible imagery will be collected in the future once the Landsat satellite becomes no longer functional.

2) Higher resolution imagery, such as IKONOS, is necessary for examining fine-scale patterns of de-icing salt effects, although it is more costly and requires considerable efforts in data preprocessing. However, Worldview-2 multispectral (8-band) satellite imagery has recently been acquired and processed for the Lake Tahoe Basin at 0.5-m resolution, with great potential for future analyses seeking to monitor the influences of roads and de-icing salt application on tree crown mortality and forest health.

3) None of the remote sensing approaches utilized were able to distinguish tree crown mortality due to de-icing salts from tree crown mortality resulting from other causes, based solely on spectral characteristics from satellite imagery. However, there is potential for future studies to develop methods for classifying tree crown mortality due to de-icing salts using hyperspectral imagery from airborne or satellite platforms.

4) Effective remote sensing protocols for monitoring road-related tree crown mortality will adopt a multi-scale approach, adopting imagery from remote sensing platforms with varying spatial and temporal resolution. Our project demonstrates how results from one scale of investigation corroborate and help to explain results from another scale.

Management

1) Aerial deposition of de-icing salt onto tree crowns by moving vehicles appears to have a much stronger effect than does uptake of de-icing salts through surface runoff or the soil solution. Tree health is affected mostly within 30m of the road, but extending in some cases to within 60m. Therefore, tree species that are more resistant to de-icing salt damage (e.g. firs) could be planted as a barrier near the road to protect the forest beyond, particularly on concave or steeper slopes where the effects of de-icing salts extend to further distances from the road.

2) De-icing salt application is a significant factor for roadside tree crown mortality. Road management should continue efforts to decrease the amount of de-icing salt used in winter or to use less deleterious alternative materials.

3) Trees at the roadside are generally healthier, causing salt damage to be more distinct, in wet years than in dry years. Mitigation strategies should be focused on de-icing salt effects in wet years while paying more attention to other damaging factors in dry years, in order to maintain roadside tree health and the ecological and aesthetic values of the Lake Tahoe Basin.

Scientific Products

Fan, Y. 2011. Tree crown mortality associated with roads in the Lake Tahoe Basin: a remote sensing approach. M.S. Thesis, University of Nevada, Reno.

Fan, Y., P. J. Weisberg, and R.S. Nowak. (In preparation). A multi-scale and multi-temporal remote sensing approach to assessing tree crown mortality associated with roads in the Lake Tahoe Basin. (To be submitted to Remote Sensing of Environment).

Fan, Y. (In Preparation). The Sun-Crown-Sensor (+C) topographic correction model for forest imagery. (To be submitted to International Journal of Remote Sensing).

Information Products

- Radiometrically corrected Landsat TM images of late summer or early fall from 1988 to 2011 (Table 4). Remote sensing estimated LAI data and annual LAI change (i.e. tree crown mortality) data at the scale of 30-m pixels for the whole Lake Tahoe Basin from 1988 to 2011.

- Geometrically and radiometrically corrected IKONOS images of 25 September 2005 and 27 September 2009 (Table 4). Remote sensing estimated LAI data and LAI change (i.e. tree crown mortality) data between 2005 and 2009 at the scale of 4-m pixels for the Nevada portion of the Lake Tahoe Basin.

- High accuracy 1-m resolution digital maps of tree crowns either from nadir view angles or from the IKONOS non-nadir view angles produced from LiDAR data.

- Field plot data (number=120, size=30×30m) for leaf area index of conifer forest stands. Precise GPS locations of these plots are included.

- ArcGIS toolbox for radiometric calibration (DN to radiance or reflectance) of IKONOS imagery.

- ArcGIS toolbox for topographic correction models (C-correction, Sun-Canopy-Sensor (+C) correction, and Sun-Crown-Sensor (+C) correction)

- ArcGIS toolbox for calculating vegetation indices (NDVI, SAVI, MSAVI, MKT).

- ArcGIS toolbox for transforming NDVI to LAI for IKONOS imagery and Landsat TM imagery.

Acknowledgements

The Nevada Department of Transportation provided funding and research data (de-icing salt application data and traffic data) for this project. Isabel Munck and Jane Van Gunst helped with field data collection during many summer days in the Lake Tahoe Basin. Many other individuals contributed to this effort too; see Fan (2011) for a more complete Acknowledgement.

Supporting Figures and Tables

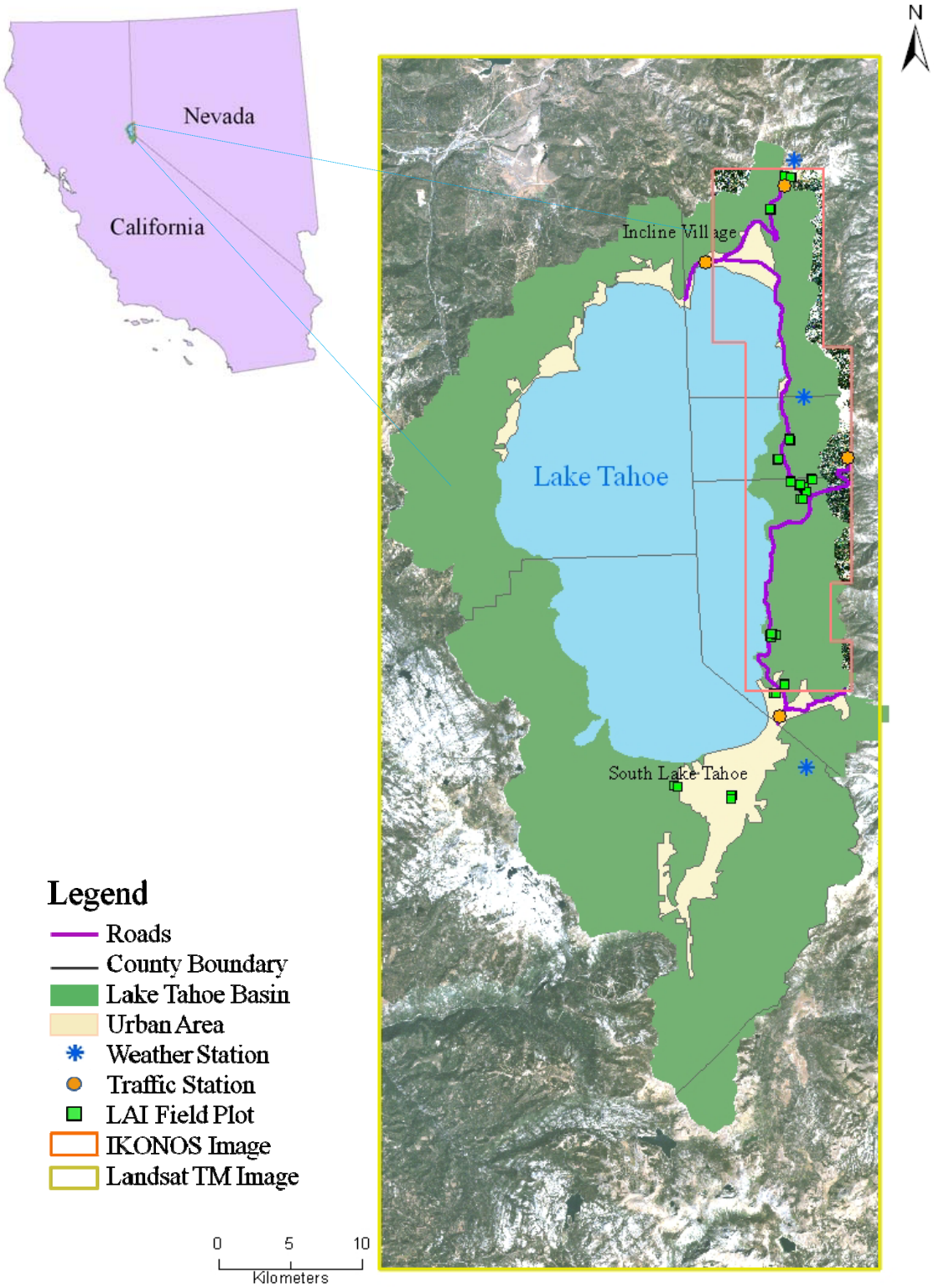

Figure 1. The Lake Tahoe Basin outline, remote sensing data coverage, field plots, weather stations, traffic stations, and the outline of major highways in the Nevada portion of the Basin.

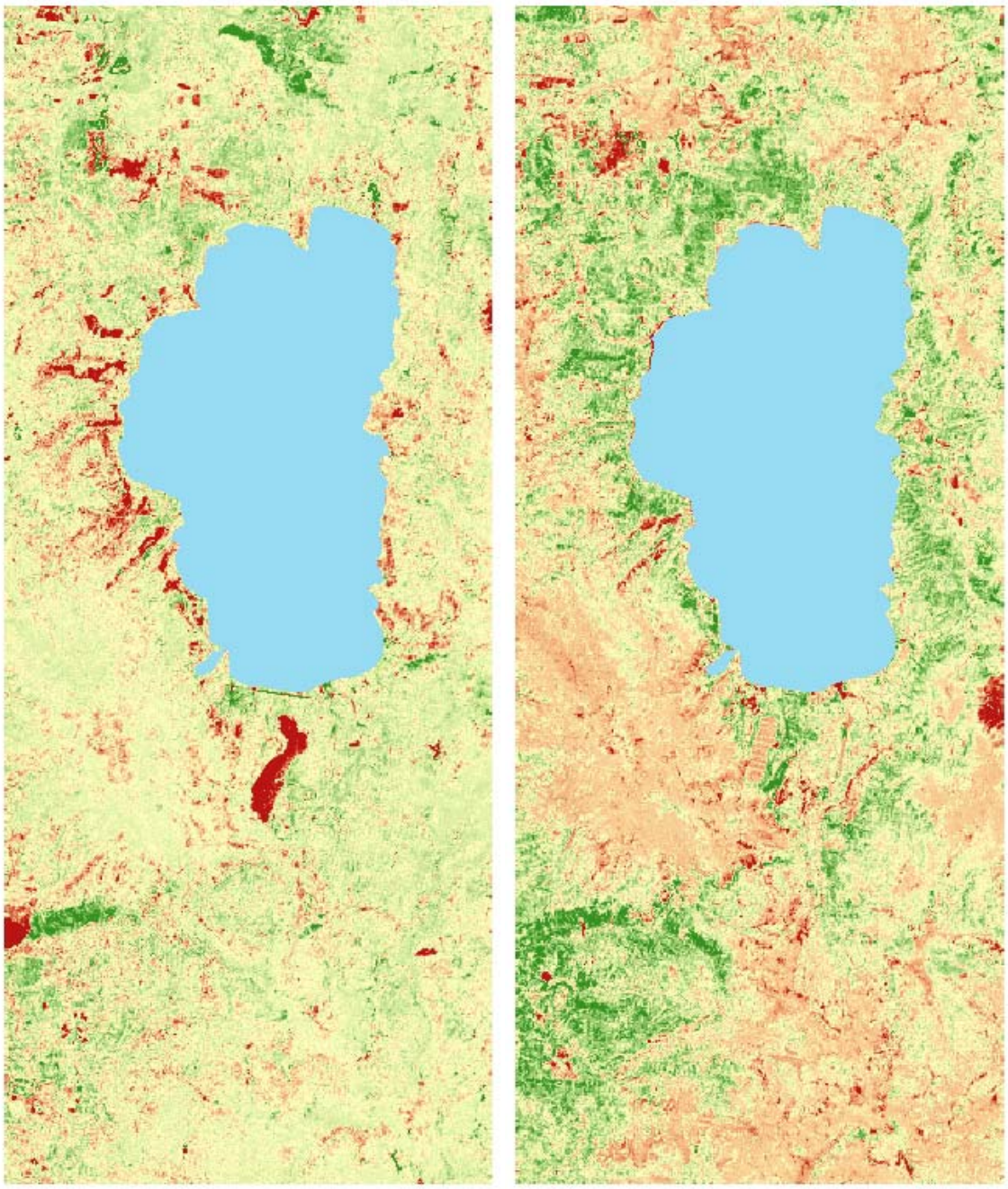

(a) (b)

Figure 2. LAI change: (a) from 25 Sep. 1993 to 26 Sep. 1999 (wet years with high salt application), (b) from 21 Sep. 2003 to 21 Sep. 2009 (dry years with low salt application) for the whole Lake Tahoe Basin using Landsat TM images. Red represents decrease in LAI (i.e. net tree crown mortality) and green represents increase in LAI.

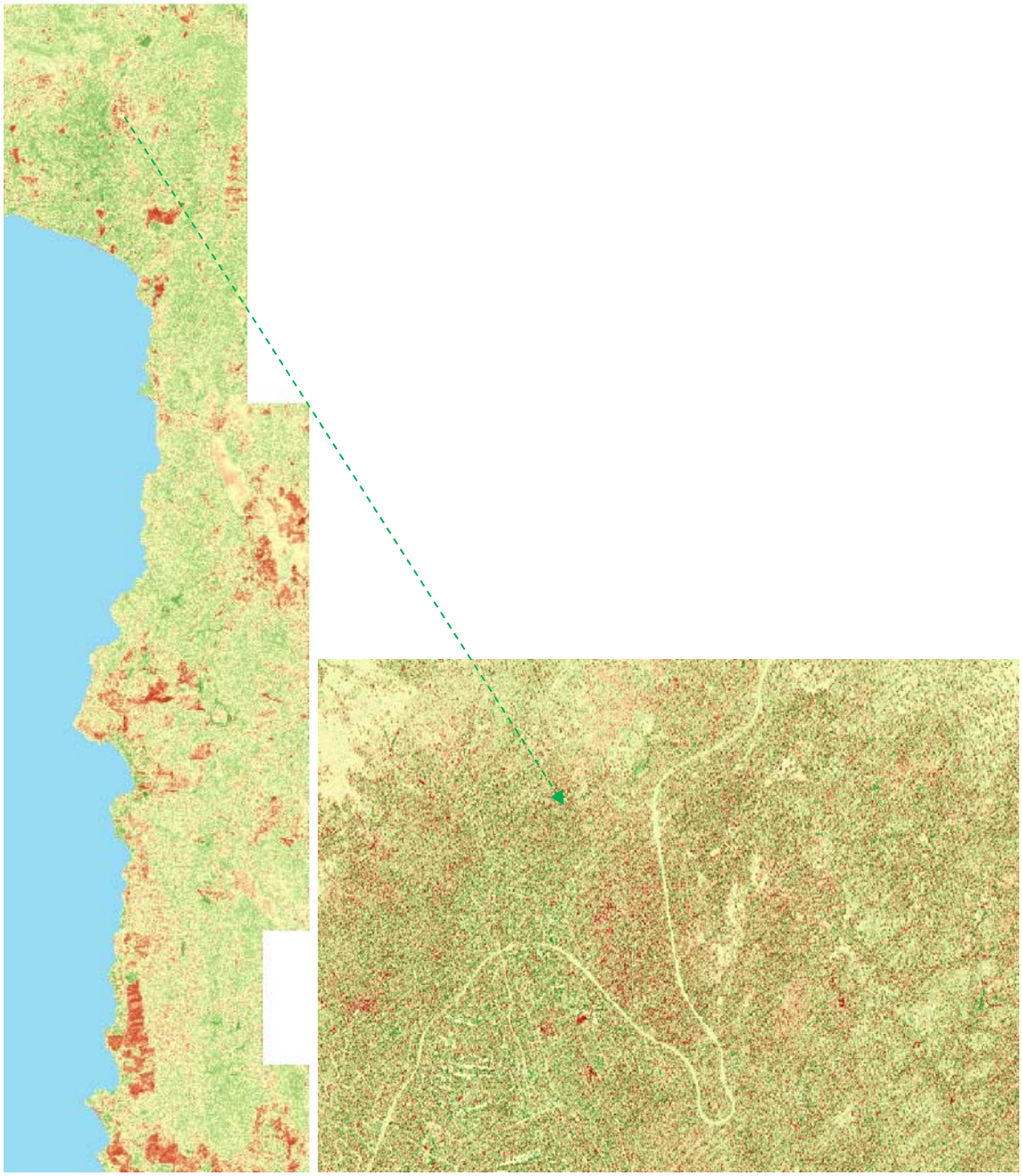

(a) (b)

Figure 3. LAI change from 25 Sep. 2005 to 27 Sep. 2009: (a) for the Nevada portion of the Lake Tahoe Basin using IKONOS images, (b) for the area around Mt. Rose highway near Incline Village. Red represents decrease in LAI (i.e. net tree crown mortality) and green represents increase in LAI.

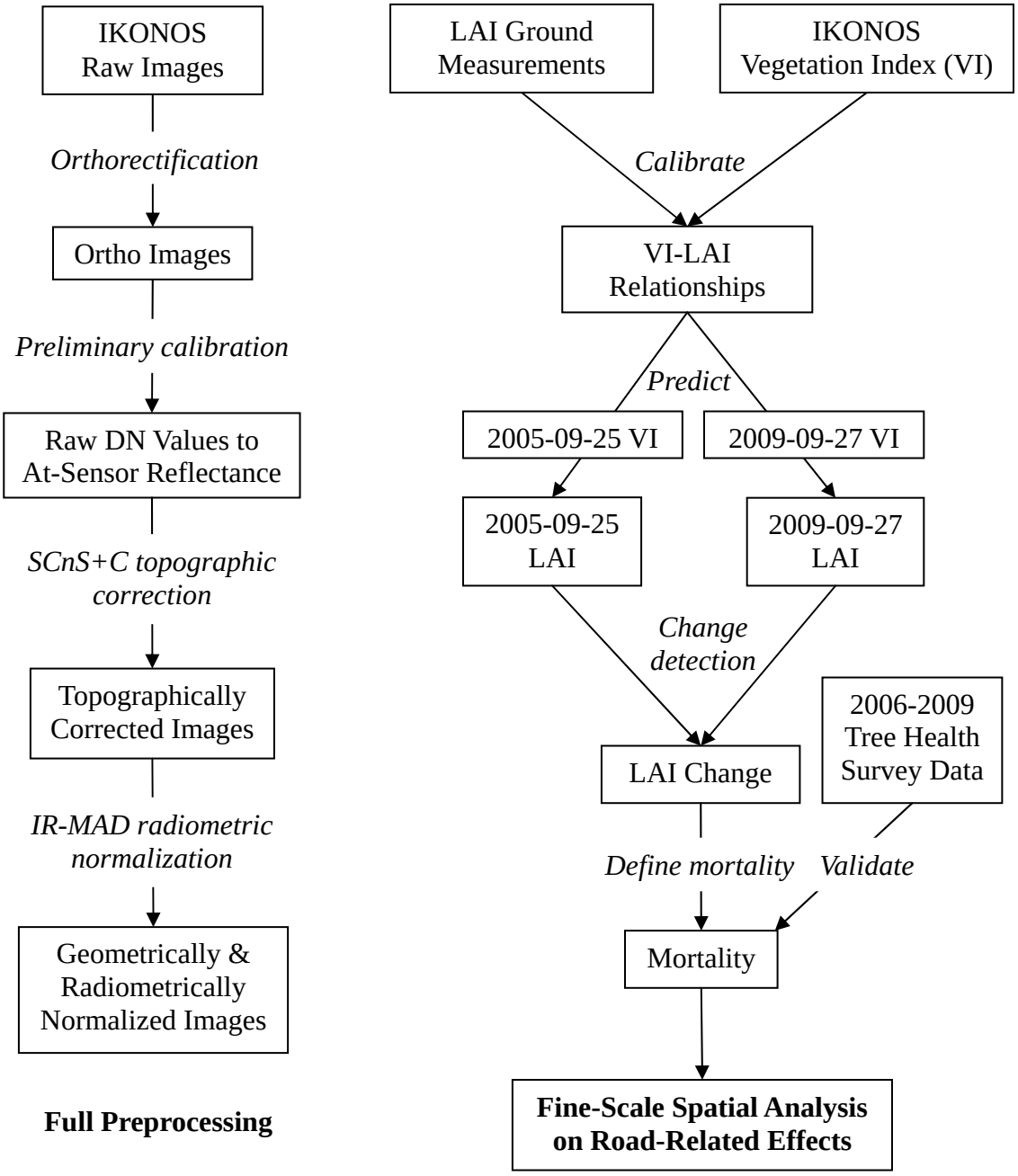

Figure 4. Flow chart of IKONOS image preprocessing, remote sensing change detection, calibration, validation, mortality derivation, and statistical analysis processes.

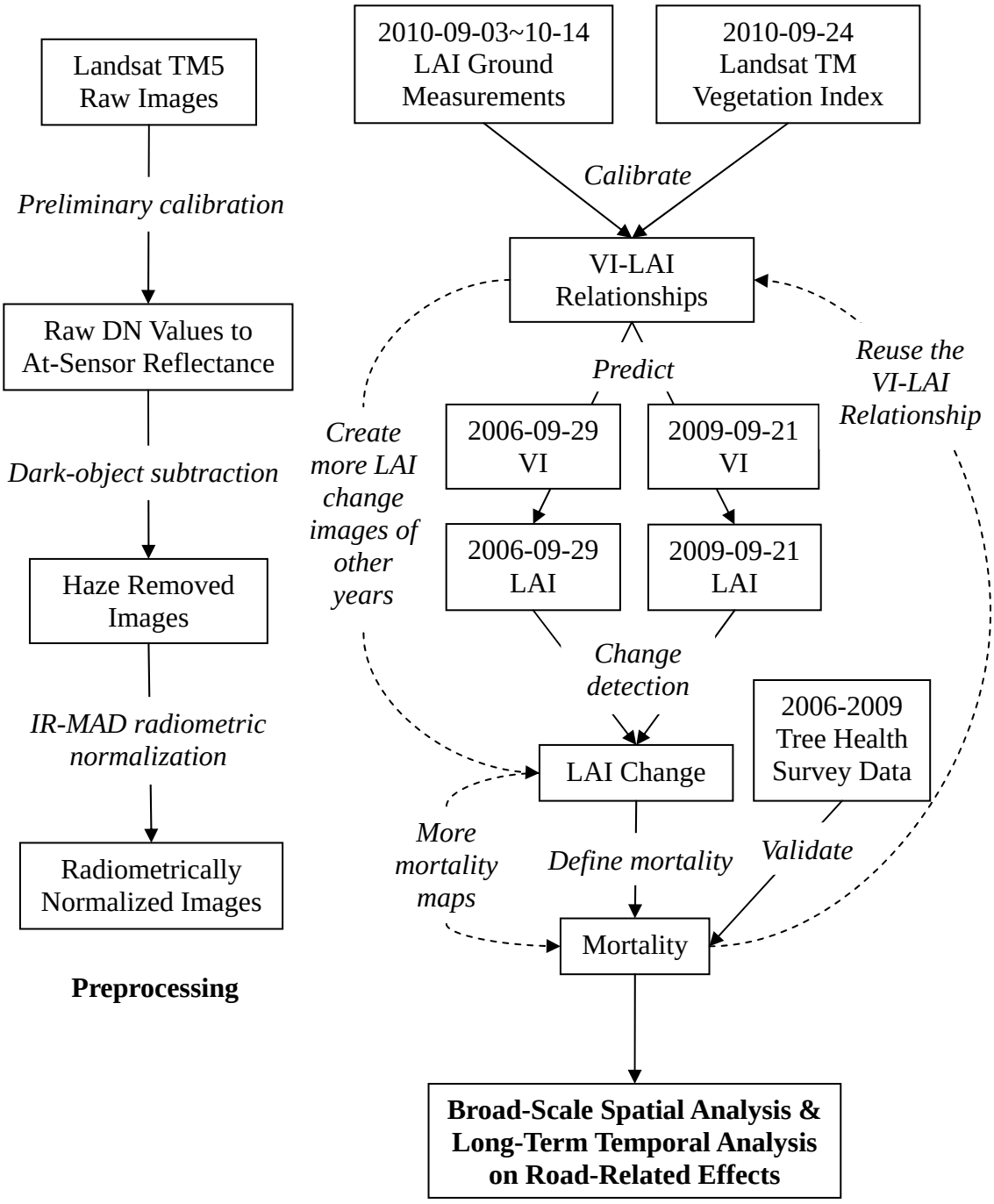

Figure 5. Flow chart of Landsat TM image preprocessing, remote sensing change detection, calibration, validation, mortality derivation, and statistical analysis processes.

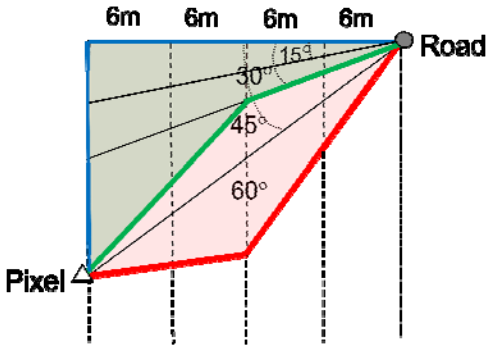

$$Profile\ Area = 6 \times [(n \times Road\ Elevation) - \sum_{1}^{n} Path\ Pixel\ Elevation]$$

$$Path\ Curvature = \frac{Profile\ Area}{Distance^2}$$

$$Aerial\ Deposition\ Probability = \frac{Path\ Curvature}{Distance}$$

Figure 6. The spatial proxy variable for aerial deposition of de-icing salt, showing a pictorial representation and GIS algorithms. The Path Pixel Elevation refers to the elevation (m) of each pixel along the direct path from the focal pixel to the nearest point along the road.

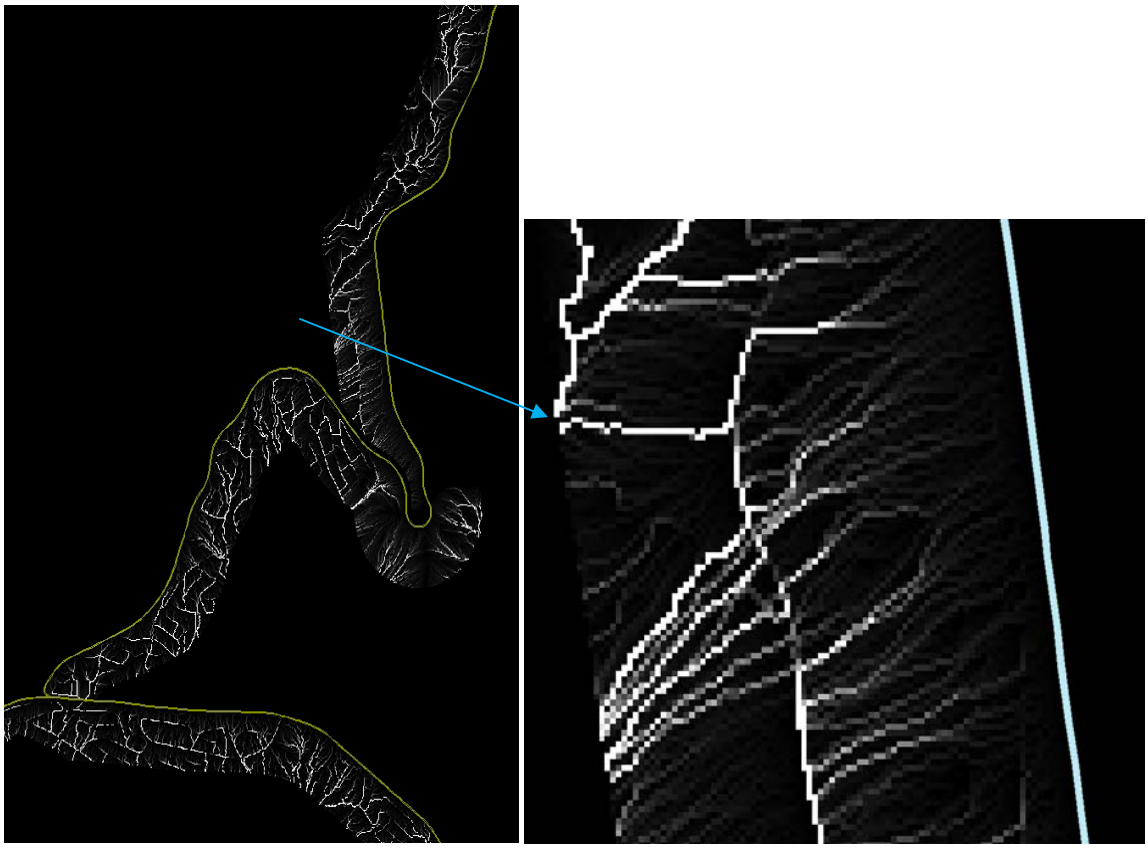

(a)

Figure 7. The spatial proxy variable for flow accumulation of de-icing salt, calculated in ArcGIS as the number of pixels expected to contribute surface or subsurface flow to each pixel in the landscape.

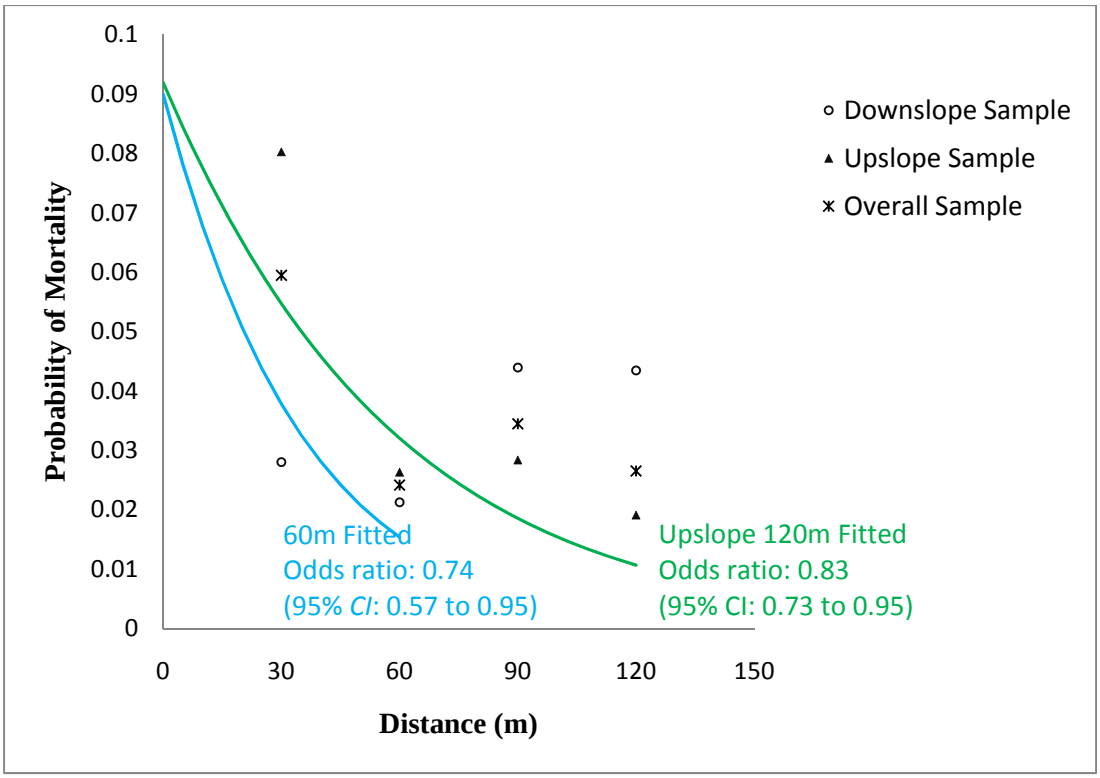

Figure 8. Fits of logistic regression models for probability of mortality at different distance zones and scatterplots of sample mortality probability using 1993–1999 change data.

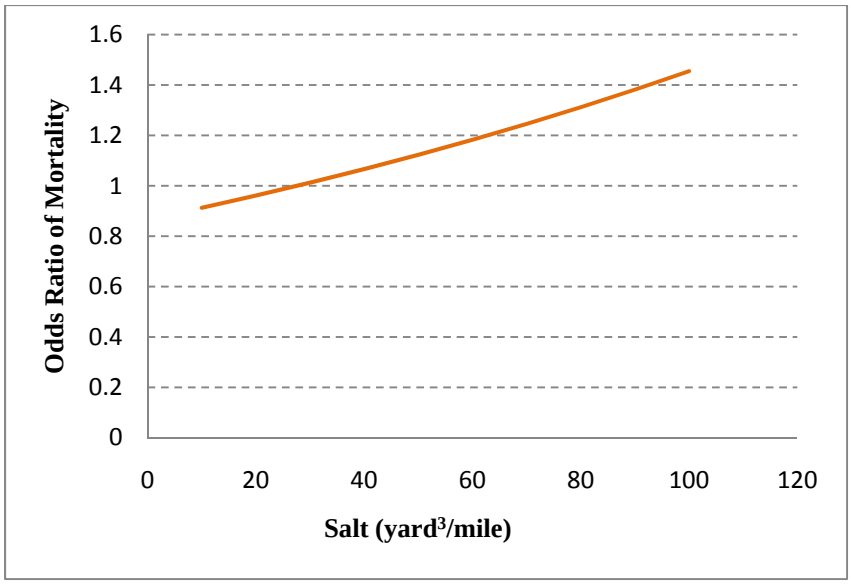

(a)

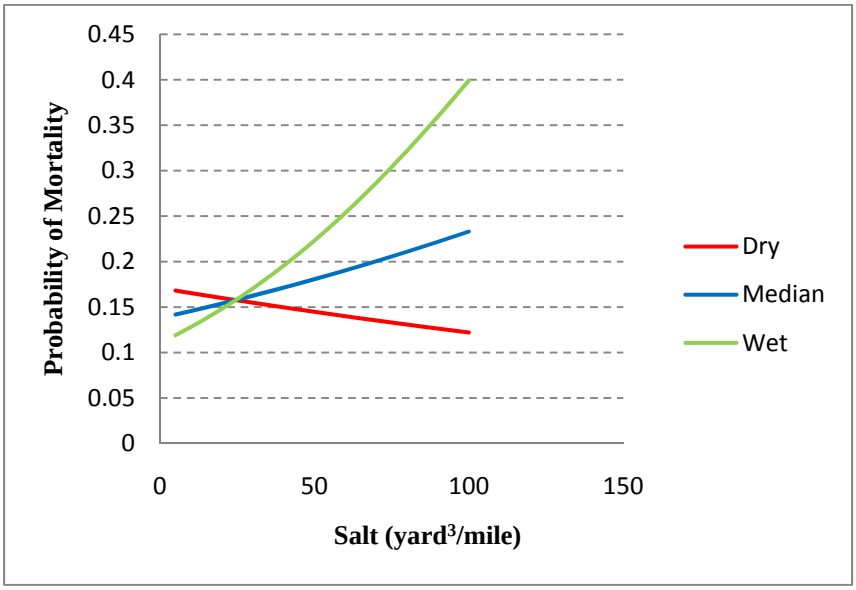

(b)

Figure 9. Interaction effects between salt and precipitation: (a) the odds ratio of mortality with every 10 yard^3/mile increase in salt application; (b) the effects of salt application on the probability of mortality during dry, median and wet years.

Table 1. Logistic regression model to assess de-icing salt effects via two mechanisms on tree mortality within 0–100m downslope zone using 2005–2009 IKONOS data.

Variable	Coefficient	Std. error	*z*-statistic	*p*-value
Intercept	-0.504	0.067	-7.555	0.000
Aerial deposition	0.0094	0.0034	2.789	0.005
Flow accumulation(log)	0.0223	0.0097	2.293	0.011
Deviance = 9910.096		DF = 7293		

Table 2. Logistic regression model to assess the effects of distance (0–60m) and wet (salt=1)/dry (salt=0) years on tree mortality probability using 1993–1999 and 2003–2009 mortality data.

Variable	Coefficient	Std. Error	*z*-statistic	*p*-value
Intercept	-2.299	0.255	-9.025	0.000
distance	0.029	0.006	4.528	0.000
salt	-0.015	0.460	-0.033	0.974
distance×*salt*	-0.060	0.015	-4.085	0.000
Deviance = 795.928		DF = 1196		

salt = 1	logit ($\hat{\pi}$) = -2.314 – 0.031*distance*	odds ratio: 0.74 (95% *CI*: 0.57 to 0.95)
salt = 0	logit ($\hat{\pi}$) = -2.299 + 0.029*distance*	odds ratio: 1.34 (95% *CI*: 1.26 to 1.42)
		(odds ratio per 10m increase in *distance*)

Table 3. The best supported model to test the interaction effects of salt and precipitation in de-icing salt effect prone area (0–60m) using 1990–2010 annual mortality data.

Variable	Coefficient	Std. Error	*z*-statistic	*p*-value
Intercept	-1.326	0.216	-6.148	0.000
salt	-0.014296	0.010152	-1.408	0.159
precipitation	-0.012680	0.005432	-2.334	0.020
salt×*precipitation*	0.000518	0.000227	2.280	0.023
Deviance = 8378.506	DF = 9596	AIC = 8386.506	BIC = 8415.184	

Table 4. All Landsat TM and IKONOS images used in this study.

Image Date	Scene Center Longitude/Latitude	Satellite	Sensor	Image ID
11-Sep-1988	120.1/38.9	Landsat 5	TM	L5043033_03319880911
03-Oct-1990	120.1/38.9	Landsat 5	TM	L5043033_03319901003
06-Oct-1991	120.1/38.9	Landsat 5	TM	L5043033_03319911006
22-Sep-1992	120.1/38.9	Landsat 5	TM	L5043033_03319920922
25-Sep-1993	120.1/38.9	Landsat 5	TM	L5043033_03319930925
15-Sep-1995	120.1/38.9	Landsat 5	TM	L5043033_03319950915
03-Oct-1996	120.1/38.9	Landsat 5	TM	L5043033_03319961003
09-Oct-1998	120.1/38.9	Landsat 5	TM	L5043033_03319981009
26-Sep-1999	120.1/38.9	Landsat 5	TM	L5043033_03319990926
12-Sep-2000	120.1/38.9	Landsat 5	TM	L5043033_03320000912
15-Sep-2001	120.1/38.9	Landsat 5	TM	L5043033_03320010915
02-Sep-2002	120.1/38.9	Landsat 5	TM	L5043033_03320020902
21-Sep-2003	120.1/38.9	Landsat 5	TM	L5043033_03320030921
23-Sep-2004	120.1/38.9	Landsat 5	TM	L5043033_03320040923
12-Oct-2005	120.1/38.9	Landsat 5	TM	L5043033_03320051012
29-Sep-2006	120.1/38.9	Landsat 5	TM	L5043033_03320060929
02-Oct-2007	120.1/38.9	Landsat 5	TM	L5043033_03320071002
18-Sep-2008	120.1/38.9	Landsat 5	TM	L5043033_03320080918
21-Sep-2009	120.1/38.9	Landsat 5	TM	L5043033_03320090921
24-Sep-2010	120.1/38.9	Landsat 5	TM	L5043033_03320100924
25-Sep-2005	-119.9/39.1	IKONOS	IKONOS-2	2005092519042390000010110092
27-Sep-2009	-119.9/39.1	IKONOS	IKONOS-2	2009092718555930000011612413

University of Nevada, Reno

Tree crown mortality associated with roads in the Lake Tahoe Basin: a remote sensing approach

A thesis submitted in partial fulfillment of the requirements for the degree of Master of Science in Natural Resources and Environmental Science

by

Yuanchao Fan

Peter J. Weisberg/Thesis Advisor

August, 2011

University of Nevada, Reno
Statewide • Worldwide

THE GRADUATE SCHOOL

We recommend that the thesis
prepared under our supervision by

YUANCHAO FAN

entitled

Tree crown mortality associated with roads in the Lake Tahoe Basin: a remote sensing approach

be accepted in partial fulfillment of the
requirements for the degree of

MASTER OF SCIENCE

Peter J. Weisberg, Advisor

Robert S. Nowak, Committee Member

Wendy Calvin, Graduate School Representative

Marsha H. Read, Ph. D., Dean, Graduate School

August, 2011

Abstract

Tree crown mortality along highways in the Lake Tahoe Basin has been a concern for decades. Increased tree damage near roads is believed to be associated with de-icing compounds used to increase driving safety during winter. Several field studies have concluded that de-icing salts applied on the roads are a potential factor for roadside tree crown mortality, but the spatial pattern and temporal trend of de-icing salt damage has not been quantitatively measured. Moreover, most previous studies were based on field observations at sampling sites and were limited by temporal and spatial scale. An efficient large-scale approach is needed that can be repeatedly applied to retrieve historical dynamics, or to monitor future occurrence, of road-related tree crown mortality. Remote sensing provides a means for assessing potential road-related effects on tree crown mortality in a large-scale and long-term context. This study used remote sensing methods to quantify tree crown mortality, expressed as declines in leaf area index (LAI) at the scale of 4-m pixels for the Nevada portion of the Lake Tahoe Basin, and at the scale of 30-m pixels for the whole basin. The mortality data together with data for salt application, precipitation, traffic, and topography were then statistically analyzed to reveal the component of crown mortality that is road-related.

Several relatively novel approaches were developed in this study for processing remote sensing images and utilizing GIS data. The Sun-Crown-Sensor (+C) topographic correction approach was developed to correct radiometric distortion caused by terrain variability in forest images. LiDAR data were utilized to aid in orthorectifying IKONOS images and extracting projected tree crown shapes from complex earth surface features. Several vegetation indices were compared and the normalized difference vegetation index (NDVI) was consistently found to be the best indicator for LAI. Interannual change in LAI was also found to be an appropriate

measurement of tree crown mortality, defined as the loss of photosynthetic material in tree crowns. A field dataset of LAI was collected at 30 plots comprising 120 subplots of 30×30m, which was used to calibrate and transform remote sensing data into LAI that is physically meaningful. A dataset of yearly change detection results as measured by quantitative LAI change was generated using Landsat TM images from 1990 to 2010. A 4-year change in LAI from 2005 to 2009 was generated using a pair of IKONOS images, for which mortality was also defined based on LAI change thresholds.

IKONOS derived mortality was used in fine-scale spatial analysis to assess the effects of de-icing salt through aerial deposition and flow accumulation mechanisms, which were represented by two spatial proxy variables constructed using high-resolution topographical data. Landsat derived mortality was used in both broad-scale spatial analysis and long-term temporal analysis. The broad-scale spatial analysis confirmed IKONOS fine-scale spatial analysis results. The long-term temporal analysis provided concrete evidence of how roadside mortality was related to variation in de-icing salt application.

A clear trend of increasing mortality with increasing aerial deposition of de-icing salt was revealed in the fine-scale spatial analysis. Aerial deposition played a major role in mortality within 30m of the road and its overall effect was much stronger than that of flow accumulation, although the effect zone of the latter had the potential to extend to 100m from road. The temporal analysis revealed that mortality was strongly correlated with salt application from 1990 to 2010. De-icing salt effects (as suggested by a trend of increased crown mortality closer to the roads) were most distinct in wet years when de-icing salt application was high and other damaging factors were weak. The spatial analysis and temporal analysis together provided convincing evidence that de-icing salt was a significant factor for roadside tree crown mortality. In order to

protect the roadside forests from degradation and preserve their aesthetic value to drivers, road management should decrease the amount of de-icing salt used as much as possible, plant salt-resistant species within the 0–30m salt-susceptible zones, and plant taller trees on concave slopes in order to minimize the aerial deposition effect.

Acknowledgement

I am grateful to my advisor, Dr. Peter Weisberg, for his attentive advising and communication during my three years' graduate study in the United States. I thank Dr. Robert Nowak and Dr. Wendy Calvin for providing valuable advisement on research design and thesis writing. Dr. Werner Schneider and Dr. Tatjana Koukal at the University of Natural Resources and Life Science, Vienna, Austria also provided much valuable assistance with remote sensing methods during my exchange study in Vienna. I thank Isabel Munck and Jane Van Gunst for collaboration in collecting field data during many summer days in the Lake Tahoe Basin. Thomas Dilts helped enhance my GIS skills. Jian Yang provided valuable feedback on my ideas and analyses. The interactions with other members of the Great Basin Landscape Ecology Lab (Susan Mortenson, Zach Nelson, Nathan Bristow, Sarah Karam, Stephanie Sunderman, Blake Engelhardt, Miles Becker, and Meredith Gosejohan) were also an important part of my time as a graduate student at UNR. I am grateful to my family and friends for their spiritual support. I also thank Nevada Department of Transportation for funding this study.

Table of Contents

List of Tables

List of Figures

1 Introduction

1.1 Background

The scenic Lake Tahoe area attracts ever-increasing residential and recreational development, which in turn has the potential to impair its environmental quality. The expanding road network and traffic within the Lake Tahoe Basin has a significant impact on the ecosystem (Forney, 2001). Issues of road effects on forest health have been drawing attention in this region since 1974, when de-icing compounds such as sodium chloride (NaCl) were observed to cause damage to conifers in the Basin (Scharpf and Srago 1974). The application of de-icing salts on major roads by state highway agencies has a decades-long history. With rising awareness of the need for environmental protection, the managers must achieve a balance between ensuring safe roads during dangerous winter driving conditions and alleviating environmental degradation. Therefore, it is important to assess the potential effects of de-icing salts on forest health and to develop efficient methods for monitoring road-related tree crown mortality.

Several studies have been conducted on de-icing salt effects on vegetation in the Lake Tahoe Basin (Scharpf and Srago 1974, Massoth 1978, Marshall 1984, Kliejunas et al. 1989, RCI 1990, Munck et al. 2010), all based on field surveys. The 1990 study by Resource Concepts Inc. (RCI) was quite extensive, leading to the establishment of 206 permanent plots. They concluded that 15% of the observed trees were apparently affected by de-icing salts, but about one-third of those trees had evidence of other damaging agents including drought, mistletoe, insects, and fungal pathogens. The overall mean zone of influence from de-icing salt was 30.2 feet from the edge of highway pavement, but differed among downslope and upslope positions relative to the highway. The mean zone of salt influence on downslopes was 36.1 feet while that on upslopes was 21.9 feet. They also observed that the degree of salt influence becomes less as the distance

from road increases, with a maximum range of 102 feet. Furthermore, their soil chemical analyses indicated very low salt content, well below the threshold for salt damage to plants. However, their measurements were taken in June and July. Salt leaches rapidly from the soil during and after snowmelt, a factor which may account for the low salt contents when measured in summer.

A follow-up study in 2006-2007 (Munck et al. 2010) re-established plots from the RCI study and added additional control plots, additional sampling of targeted soils and species, and quantitative measurements of all sources of crown damage, to increase statistical rigor and improve the ability to discern the damage due to de-icing salts. One important result from this study was in accordance with that of RCI study: the presence of high Na and Cl content in conifer foliage was symptomatic of salt damage, but the total amount of salts and other ions in soils, even in winter, was well below the threshold for salt damage to even the most sensitive plant species. They considered that aerial deposition of de-icing salts on foliage from salt spray generated by passing vehicle traffic might be the primary cause of tree crown mortality (Bryson and Barker 2002), although they could not rule out uptake of salts from soil. Other results from this study include: (1) a total of 53% of roadside trees in 2006 and 27% in 2007 had salt damage, with approximately 1/5 of these trees having other types of damage in each year, and 12% and 22 % of roadside trees had no salt damage but some other types of damage in 2006 and 2007, respectively; (2) the extent of salt damage within an individual tree tended to be small although a significant proportion of trees displayed salt damage; (3) the presence of other diseases or insects did not appear to negatively interact with salt damage. Instead, salt damage may partially displace or mask disease or insect damage; and (4) distance from the roadside and slope steepness had strong influences on the extent of salt damage observed, while the impact of other

environmental variables such as soil type, elevation and aspect was small. Specifically, 50% of trees with salt damage were within 41 feet from roadside in 2006 and 21 feet in 2007; > 25% of trees in 2006 and ~5% of trees in 2007 had salt damage at distances >101 feet from roadside.

Although previous studies provided important knowledge concerning effects of de-icing salts on forest health, there remained some unsolved questions and room for improvement. The severity and extent of salt damage within the Basin need to be examined in a more quantitative way and at a broader scale. Previous studies usually described salt damage in category or percentage and the results were based on limited field plots where the generalizability to the whole study area was not guaranteed. Also, the functional relationships between salt damage and its underlying causal factors were not modeled statistically. For example, the functional forms of the relationships (e.g. linear vs. non-linear) between road-related factors (e.g. distance from road, roadside topography, and salt application) and severity of salt damage are not yet known. Moreover, long-term changes in road-related tree crown mortality were not thoroughly examined. Although some studies (Scharpf and Srago 1974, Kliejunas et al. 1989, RCI 1990, Munck et al. 2010) compared pairs of years with a long intervening time interval, these field methods did not allow detection of changes within a series of years. Moreover, an efficient monitoring approach that does not require extensive field surveys is still lacking. Studies based on field surveys are limited in their ability to answer these kinds of questions by expense, time and spatial extent.

1.2 Remote Sensing Methodology for Monitoring Tree Crown Mortality

Remote sensing methodology can complement and improve the ability of traditional field-based studies and is commonly used to investigate forest disturbance and tree mortality (Macomber and Woodcock 1994, Clark et al. 2004, Wulder et al. 2006, Guo et al. 2007). It has

the ability to generalize limited findings from field-based forest mortality studies to a much larger scale. Archival satellite imagery allows historical analysis of crown mortality due to road-related and non-road-related factors, and various sources of future imagery can also provide an inexpensive, efficient and repeatable protocol for future monitoring. Remote sensing of forest mortality can be accomplished at different spatial resolutions, from coarse (e.g. >1-km SPOT VGT, MODIS TERRA) to moderate resolutions (e.g. 30-m Landsat TM), and to very fine resolutions such as 1-m or 4-m (IKONOS). In this study, both moderate and fine resolution images (30-m Landsat TM and 4-m IKONOS) were used.

Vegetation indices, classification algorithms and digital change detection methods are generally involved in the remote sensing process of deriving forest mortality information. Normalized Difference Vegetation Index (NDVI) is the most well-known vegetation index used to detect living plant canopies (Rouse et al. 1974). The Kauth-Thomas (Tasseled Cap) transformation is also commonly used, which generates three orthogonal components representing scene features: brightness, greenness and wetness (Kauth and Thomas 1976, Crist and Cicone 1984a). Various other vegetation indices such as Soil-Adjusted Vegetation Index (SAVI, Huete 1988) and Modified Soil-Adjusted Vegetation Index (MSAVI, Qi et al. 1994) have been created to reduce the influence of external factors and to enhance accuracy.

Change detection is the process of identifying differences in the state of an object or phenomenon from different points of time. Using satellite images from different dates, the change of forest canopy cover, greenness or health status can be measured and thus tree crown mortality can be derived. Change detection generally involves the use of vegetation indices or other transformations that are developed by combining two or more spectral bands and are capable of indicating relative abundance and activity of green vegetation. Digital change

detection using multi-temporal imagery can more effectively estimate forest mortality than single-date image analyses (Muchoney and Haack 1994, Coppin et al. 2004, Liu et al. 2006). Most commonly used change detection methods include image differencing (e.g. NDVI Differencing), multi-temporal linear data transformation (e.g. multi-temporal Kauth-Thomas transformation (MKT), multi-temporal principal component analysis (PCA)), multi-date composite image classification, post-classification comparison and spectral change vector analysis (CVA) (Chen et al. 2003). Singh (1989) indicated that the simple technique such as image differencing performed better than much more sophisticated methods such as principal components analysis for tropical deforestation monitoring using Landsat data. Collins and Woodcock (1996), studying forest mortality in the Lake Tahoe Basin (without consideration of road effects), compared three change detection methods: MKT, multi-temporal PCA, and Gramm-Schmidt orthogonalization. They found that MKT was the most efficient and reliable method. MKT is actually the normalized difference of the Tasseled Cap indices. In this study, I tested and compared quantitative change detection methods such as vegetation index differencing as well as qualitative methods such as post-classification comparison.

Calibration and validation of change detection results using field data are a vital part of the remote sensing approach. They relate digital evidence to real vegetation status and generalize findings from limited field surveys (hampered by spatial, temporal and financial considerations) to a much larger scale. The extent of satellite imagery can easily cover the whole study area and archival images permit a long-term analysis.

The remote sensing component of this study was designed to use satellite imagery at multiple scales of spectral, spatial, and temporal resolution to examine road-related tree crown mortality in a multi-scale and long-term context, with a focus on the Nevada portion of the Lake

Tahoe Basin. Tree crown mortality refers to the loss of photosynthetic material in tree crowns, and does not necessarily imply tree death. Photosynthetic material was measured by healthy leaf area index (LAI) in this study. In addition, what I examined was "net mortality" which included mortality and re-growth of photosynthetic material at the tree level (fine-scale) or mortality in some trees and natural growth in other trees at the plot level (broad-scale). A remote sensing methodology for monitoring tree crown mortality was established, including the design and comparison of different image preprocessing methods, vegetation indices, change detection methods, and the calibration and validation of remote sensing results using field data (e.g. leaf area index, tree health surveys). I estimated and spatially modeled tree crown mortality, expressed as declines in leaf area index (quantitative change detection) or changes in tree health status (qualitative post-classification change detection), at the scale of 30-m pixels for the whole Lake Tahoe Basin using Landsat TM imagery, or at the scale of 4-m pixels for the Nevada portion of the Basin using IKONOS imagery. The remote sensing evidence of mortality was used together with road-related information and other datasets in statistical analyses to examine road-related effects.

1.3 Development of Statistical Approaches for Assessing Road-Related Mortality

After retrieving tree crown mortality by remote sensing, I employed statistical approaches to isolate road-related effects on tree crown mortality from non-road-related effects and to analyze the mechanisms of spatial and temporal variations in tree crown mortality associated with roads at different scales.

Road-related effects mainly refer to the de-icing salt effects, taking into account salt application, distance from road edge, roadside topography, and traffic volume. Other potential

road-related effects include automobile emissions, especially ozone. Previous studies showed that a significant proportion (15 – 53%) of observed roadside trees in the Lake Tahoe Basin had de-icing salt damage, and that approximately 20 – 30% of these trees had other types of damage at the same time (RCI 1990, Munck et al. 2010). Isolating de-icing salt effects from other tree mortality factors (climate change, drought, pathogens, insects, parasites, wildfire and fuel reduction treatment) was an important task of this study and it was dealt with primarily by statistical methods. In addition, the previous studies revealed that distance from roadside and topography had strong influences on the extent of salt damage, while other environmental variables such as soil type, elevation and aspect were less important. The influences of these two important variables and their interaction were further modeled statistically, for which the remote sensing component of this study provided abundant and well-distributed statistical data. Moreover, the remote sensing results for the Lake Tahoe area from 1988 to 2010 provided the opportunity to examine long-term dynamics of roadside tree crown mortality associated with de-icing salt application, climate and traffic.

1.4 Objectives

This study had two components: methodological development and application. The methodological component of my study addressed remote sensing approaches for deriving tree crown mortality, whereas the application component investigated the influences of road-related effects on tree crown mortality by both spatial and temporal analyses. Specifically, I had the following four objectives:

(1) Investigate remote sensing methods for robust processing of remotely sensed data and efficient monitoring of tree crown mortality.

(2) Statistically isolate the component of crown mortality that is road-related (e.g. de-icing salt damage) from other mortality agents (e.g. climate change, drought, pathogens, insects, parasites, wildfire and fuel reduction treatment);

(3) Statistically model the interaction effect of distance from road and roadside topography (e.g. steep upslope, gradual upslope, flat, gradual downslope, and steep downslope) on de-icing salt damage;

(4) Evaluate how trends in road-related mortality may have changed over the last two decades, with special attention to the effect of snowfall/drought and road de-icing salt management.

From the results of previous studies (RCI 1990, Munck et al. 2010), I hypothesized that:

(H1) De-icing salt plays a major role in roadside tree crown mortality. Therefore, there should be clear statistical relationships between remote sensing derived tree crown mortality and distance from road, given the two possible salt damage mechanisms: soil uptake and aerial deposition. A decreasing trend of tree crown mortality should be observed with increasing distance from roads.

(H2) Distance from road and roadside topography (e.g. slope steepness and downslope versus upslope) codetermine the degree of salt damage to tree crowns, no matter whether the mechanism is salt uptake from soil or direct aerial deposition on foliage. Down slopes should be exposed to salt damage, whereas up slopes should have less or no de-icing salt effects. A broader zone of salt influence should be observed on a steeper down slope than flatter ones.

(H3) Road effects on tree crown mortality have spatial limits. The above relationships will no longer exist beyond a certain distance from road.

(H4) Temporal variation in road-related tree crown mortality is best explained by the combination of de-icing salt application, traffic, and climate variables. An increasing trend of roadside tree crown mortality should be associated with increasing amount of salt applied, after accounting for climate and traffic.

2 Methods

2.1 Study Area

The Lake Tahoe Basin is located in the Sierra Nevada Mountains, along the border between California and Nevada (Figure 1). Elevation ranges from 1897 m at lake level to 3320 m at Freel Peak in the south end of the watershed. The Basin was formed by geologic block faulting about 2 million years ago, with uplifted blocks creating the Carson Range on the east and the Sierra Nevada on the west and down-dropped blocks creating the basin in between. This geologic history determines its complicated topography that has to be considered in understanding. My study focused on the Nevada portion of the Basin (east side).

Mean annual precipitation ranges from about 660 mm near the lake on the east side of the basin to over 1,400 mm in watersheds on the west side of the basin. Most precipitation falls as snow between November and April. Snowpack often persists more than 200 days at higher elevation and more than 130 days at lake level. Maximum temperatures exceed 90 °F (32.2 °C) on an average of 2.0 days annually. Minimum temperatures of 32 °F (0 °C) or lower occur on an average of 231.8 days annually, and minimum temperatures of 0 °F (-17.8 °C) or lower occur on an average of 7.6 days annually (WRCC 2008).

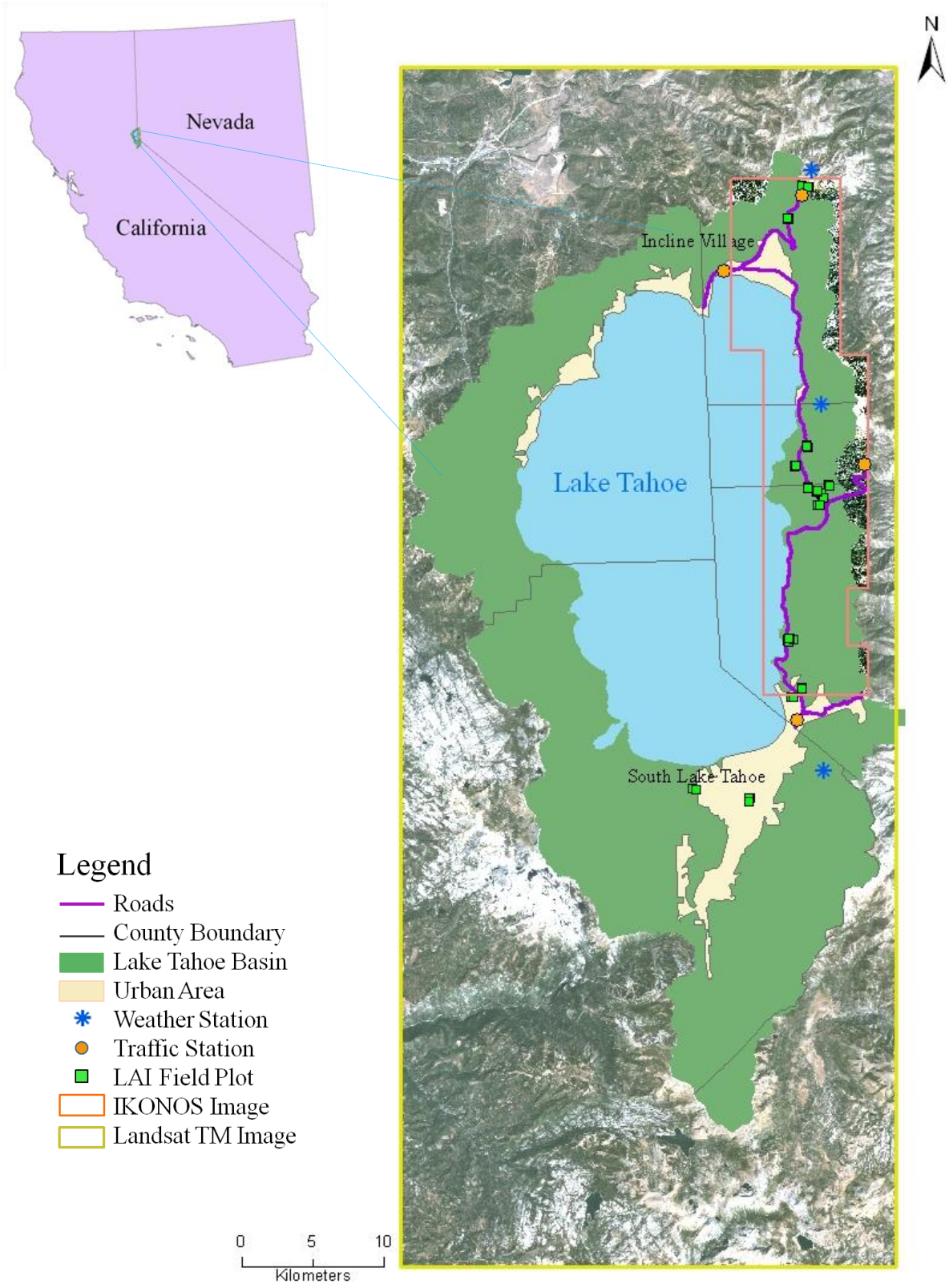

Figure 1. The Lake Tahoe Basin outline, remote sensing data coverage, field plots, weather stations, traffic stations, and the outline of major highways in the Nevada portion of the Basin.

Climate change such as global warming has changed the precipitation pattern in the region. Less snowfall in recent winters (2000–2004 and 2007–2009) has the potential to reduce forest water reserves and impact forest ecosystem dynamics. Snowfall directly influences the amount of de-icing salt applied on the highways, whose potential effects on roadside tree crown mortality are of major concern in this study. Drier years have significantly less salt application (2000–2009) relative to wet years (1993–1999).

Vegetation in the Lake Tahoe Basin is dominated by different types of coniferous forests at different elevation levels, which are described in detail by Manley et al. (2000). Most common species are Jeffrey pine, lodgepole pine, ponderosa pine, white fir, red fir, and incense cedar. Other conifers include western white pine, sugar pine, whitebark pine, singleleaf pinyon pine, limber pine, hemlocks, and junipers. Hardwood species such as aspen and alder occur more locally in moist environments. In addition, the Basin contains significant areas of wet meadows and riparian wetlands, dry meadows, brush fields of sagebrush and chaparral species such as Manzanita, and rock outcrop areas, especially at higher elevations. In recent decades, drought, pathogens, insects, parasites, fuel reduction treatments, wildfires and de-icing salt effects have caused high levels of tree damage and mortality throughout the Basin (Walker et al. 2007). However, little quantitative data are available on the incidence and severity of such damaging agents.

Residential development and recreational use (i.e. winter sports, water sports, hiking, bicycling, and gambling) within the Basin have experienced dramatic increases since the construction of gambling casinos in the Nevada part of the Basin during the mid-1950s and the completion of the interstate highway links for the 1960 Winter Olympics held at Squaw Valley. Since the 1980s, development has slowed down due to controls on land use. The overall

residential population of the Tahoe Region increased gradually from 46,887 in 1987 to 62,894 in 2000. Although the year-round population between 2000 and 2005 decreased by 7,662, in consequence of a dramatic increase in residential home price starting in 2001, prediction models still incorporate assumptions for long-term population growth in the Basin (TRPA 2008).

The transportation network in the Nevada portion of the Lake Tahoe Basin mainly consists of four highways: Nevada Highway 431 (SR-431), Nevada Highway 28 (SR-28), US Highway 50 (US-50), and Nevada State Route 207 (SR-207). They are divided into six sections by Washoe, Carson City and Douglas counties. De-icing salt application is maintained separately on these six route sections. Traffic is monitored by four continuous Automatic Traffic Recorder (ATR) count stations on highways SR-431, SR-28 and US-50 in the Nevada portion of the Basin. Demographic and economic changes have caused dynamic shifts in winter traffic, which influence the amount of de-icing salts applied and the extent of de-icing salt spray onto roadside tree crowns.

2.2 Data Collection

2.2.1 Field Data

2.2.1.1 Tree morphologic and pathological survey

A recent project (Munck et al. 2010) provided detailed field survey data (216 plots) from 2006 and 2007 on tree crown severity of salt damage and other agents such as insects and pathogens. My study used these data in conjunction with newly collected field data to validate remote sensing change detection analyses. The field plots were 100ft × 100ft (30.48m × 30.48m) squares, which are very close to the 30m × 30m pixels of Landsat TM5 images. The locations of the corners of these plots were recorded by Garmin GPSMAP 60CSx GPS. By overlapping those

coordinates on Landsat images, 70 of the 216 plots were observed to have more than 80% overlap with Landsat pixels. These plots were chosen to be re-surveyed in 2009.

From Aug. 15, 2008 to Sep. 10, 2008, we additionally surveyed 35 field plots, including 1347 trees. Each plot is a 30m × 30m square, exactly representing a single pixel on Landsat TM image. Each square was located on the field by the coordinates of four corners of corresponding pixel using sub-meter precision GPS (Trimble GeoXT GPS). All trees with DBH>10 cm within the square were surveyed and tagged. We recorded plot center coordinates, elevation, slope, number of trees, and canopy cover (by densiometer) for each plot, and tree species, DBH, salt damage rating, needle damage rating, pathogen ID, disease severity, insect ID, insect severity, dieback, and overall tree health rating for each tree. Detailed field survey methods were described in Munck et al. (2010).

From Sep. to Oct., 2009, the 35 plots sampled in 2008 were resurveyed using the same methods. In addition, 42 plots of 2006 and 29 plots of 2007 from Munck et al. (2010) which have more than 80% overlap with Landsat pixels were re-located by Trimble GeoXT GPS and were adjusted to correspond to those 30m×30m pixels. Trees outside of the pixel were excluded and only those inside the pixel were re-surveyed.

These ground reference data including tree DBH and health status were compiled and transformed to healthy canopy cover or foliage biomass for each plot (Section 2.3.7), which were then used to validate remote sensing change detection results.

2.2.1.2 Ground-based leaf area index (LAI) measurements

In order to collect more accurate tree crown information, additional field measurements of leaf area index (LAI) were collected from Sep. 3 to Oct 14, 2010 using LI-COR LAI-2000 Plant Canopy Analyzer (LI-COR Inc., Lincoln, Nebraska). This equipment calculates leaf area index and other canopy structure attributes from diffuse radiation measurements made with a "fish eye" optical sensor. Its optical sensor is filtered to reject radiation above 490 nm, which minimizes the influence of radiation scattered by the foliage. Measurements made above and below the canopy are used to determine canopy light interception in five angular bands about the zenith (0.0 – 12.3°; 16.7 – 28.6°; 32.4 – 43.4°; 47.3 – 58.1°; 62.3 – 74.1°). The light interception information is then used to compute LAI with a model of radiative transfer in vegetative canopies (LI-COR 1992). The measured LAI directly represents the actual abundance and status of live vegetation on a per-plot basis. Thus it is more closely related to vegetation indices derived from remote sensing than is canopy cover.

Sampling plots were selected based on the criteria described in Appendix A. Thirty 60m×60m plots were located and surveyed. Each plot contains 4 sub-plots, corresponding to 4 Landsat TM pixels. Pixel corners and centers were marked by flags. A 90 degree azimuth view cap was used, so that unwanted objects including the surveyor were blocked from the sensor. The 90 degree view also facilitated the sampling design as follows. Ten measurements were made for each pixel, including 2 reference readings at the open site, 4 below canopy measurements at four pixel corners, and 4 at the center of pixel facing four corners. The estimated view distance of LAI-2000 is approximately 20m. So, 8 below canopy readings should fully comprise the pixel and allow some overlap for minimizing noise (Figure 2). These multiple measurements were integrated into a single LAI for the pixel using the software FV2200 (LI-COR Inc., Lincoln,

Nebraska) designed for processing data generated by LAI-2000 Plant Canopy Analyzer. The field LAI data were used to calibrate vegetation indices from satellite imagery (Section 2.3.4).

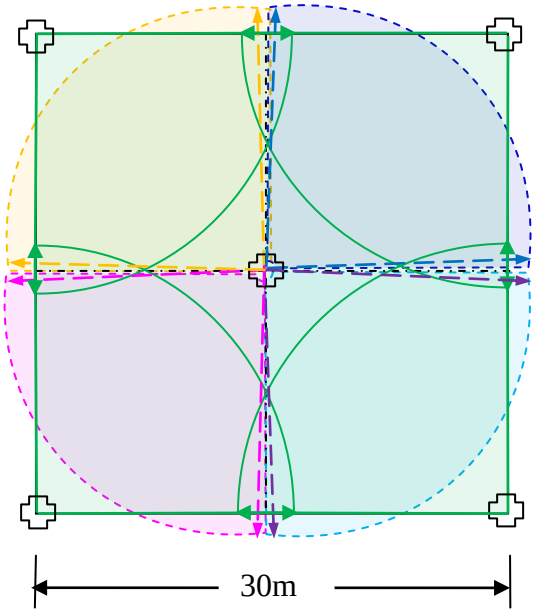

Figure 2. LAI sampling design for each pixel. The square is a 30m×30m pixel. Four below canopy measurements are made at the four pixel corners (the four green 90° fan-shaped sectors). At the pixel center, four below canopy measurements are made facing four corners (the four different color 90 degree fan-shaped sectors starting from the center).

2.2.2 Remote Sensing Data

a) Landsat TM

Landsat TM images for each year from 1988 to 2010 were acquired from the USGS Earth Resources Observation and Science Center (EROS) website (http://landsat.usgs.gov/, October, 2008). In order to minimize potentially confounding spectral influences from understory vegetation, images were selected from late summer or early fall (before first snowfall), at which season deciduous trees (primarily aspen), herbs and shrubs are dormant, but conifers are still

photosynthetically active. Mid-September was the preferred acquisition date and near anniversary images were selected to minimize confounding effects from plant phenological change or other unmeasured factors (Appendix B). Images of 1989, 1994, and 1997 were excluded because no suitable acquisitions were available due to cloud or snow cover. Landsat TM imagery consists of seven spectral bands with a spatial resolution of 30 meters for band 1 (0.45 – 0.52 µm), band 2 (0.52 – 0.60 µm), band 3 (0.63 – 0.69 µm), band 4 (0.76 – 0.90 µm), band 5 (1.55 – 1.75 µm), and band 7 (2.08 – 2.35 µm). Band 6 (thermal infrared, 120-m resolution) was not used. The images have been processed as Level 1T, which provides systematic radiometric and geometric accuracy by incorporating ground control points, while also employing a Digital Elevation Model (DEM) for topographic accuracy (USGS 2008).

b) IKONOS

A pair of IKONOS images with similar solar angles and satellite collection angles for 25 September 2005 and 27 September 2009 was used in this study (Appendix B). The near-anniversary dates minimize variation in plant phenology and focus the analysis on between-year tree physiological changes. The similar sun angles ensure similar shadows cast by tree crowns and other tall objects. This is important because IKONOS data are prone to shadow effects (Asner 2003). Satellite collection angles for these two dates are also similar but not identical. The effects of difference in collection angles are discussed in the later sections. The IKONOS images encompass a buffer of approximately 2 – 4km adjacent to the main highway traversing the east shore of Lake Tahoe, with a total coverage of 102 km2. The imagery consists of blue (445 – 516 nm), green (506 – 595 nm), red (632 – 698 nm) and near-infrared (757 – 853 nm) bands with spatial resolution of 4 meters and a panchromatic band (526 – 929 nm) with 1-meter resolution. The 1-meter resolution of the panchromatic band enables visual recognition of single tree

crowns. The 11-bit data depth of IKONOS imagery provides higher radiometric resolution than Landsat (8-bit) for change detection and classification.

2.2.3 GIS Data

a) LiDAR

Light Detection and Ranging (LiDAR) data for the lands surrounding Lake Tahoe were collected by Watershed Sciences, Inc. (WSI) from August 11th to August 24th, 2010. The LiDAR survey used two Leica ALS50 Phase II laser systems mounted in a Cessna Caravan 208B. The Leica systems were set to acquire ≥ 83,000 – 105,900 laser pulses per second (i.e., 83 – 105.9 kHz pulse rate) and flown at 900 – 1300 meters above ground level (AGL) depending on weather and terrain, capturing a scan angle of ±14° from nadir. These settings were developed to yield points with an average native pulse density of >8 pulses per square meter over terrestrial surfaces. The resulting average first-return density of delivered dataset is 11.82 points per square meter with an average ground point density of 2.26 points per square meter. The vertical accuracy was estimated at 3.5 cm RMSE (OpenTopography Facility 2011).

LiDAR data were generated and downloaded from the NSF OpenTopography Facility website (http://www.opentopography.org/index.php, April, 2011). All return point classes: Ground, Water, and Unclassified (Vegetation & Structures) were chosen so that both the first return surface (i.e. Digital Surface Model (DSM) including tree crown surface) and ground surface (i.e. Digital Elevation Model (DEM)) were more accurately generated. These two data sources were utilized to generate several useful datasets for multiple purposes as discussed in the remote sensing methodology section (2.3).

b) NED

The National Elevation Dataset (NED) for the Lake Tahoe Basin was obtained from the USGS website (http://ned.usgs.gov/, September, 2009). The resolution is 1 arc second (i.e. 30 m). NED is developed by merging the highest-resolution and best-quality elevation data (e.g. DEM) available across the United States into a seamless raster format (USGS 2009a). Topographic and hydrological variables used for road effect analysis were initially derived from NED. After LiDAR data became available from April, 2011, NED was used as the supplementary elevation dataset for the locations outside of LiDAR data coverage.

c) DOQ

Digital Orthophoto Quadrangle (DOQ) imagery of 1998 with 1-meter resolution from Lake Tahoe Data Clearinghouse (http://tahoe.usgs.gov/, August, 2008) was acquired for auxiliary uses, such as checking the quality of IKONOS orthorectification.

d) Vegetation Data

A digital map of vegetation composition and structure with 30-meter resolution in GRID format for the Lake Tahoe Basin was downloaded from USGS National Map LANDFIRE website (http://landfire.cr.usgs.gov/viewer/, December, 2009). Every pixel contains detailed information about vegetation species, structure and classification (USGS 2009b).

e) Road Data

A detailed transportation shapefile including roads of all levels for the whole Basin was downloaded from Lake Tahoe Data Clearinghouse (http://tahoe.usgs.gov/, December, 2009). However, for fine-scale analyses, I digitized a high-precision road shapefile based on orthorectified IKONOS panchromatic images, on which the central lines and edges of roads are resolved. Different widths of roads were considered. Up and down slopes along the major roads

were also delineated in detail with the aid of topographic data (e.g. slope and aspect images) and hydrological data (drainage basin, stream lines and range lines maps) derived from LiDAR DEM. Buffer zones of 0 to 500 meters from road edge with 10-m interval were generated and the intersections with the up-and-down slope shapefiles were used for road effects analysis.

2.2.4 Salt Application Data

I acquired de-icing salt application data from 1988 to 2010 per fiscal year (from July 1st to June 30th of the following year) from the Nevada Department of Transportation (NDOT) (Appendix C). Data include the amount of salts and sand applied in cubic yards at a ratio of 5:1 (this ratio was recently changed to 3:1 in fall 2006), straight salt applied in cubic yards, salt brine applied in gallons, and total amount of salt applied in cubic yards. The average amount of salt applied per mile on six major route sections (SR-431 WA, SR-28 WA, SR-28 CC, SR-28 DO, US-50 DO, SR-207 DO) was used as a predictor variable.

2.2.5 Traffic Data

Traffic count information was obtained from NDOT (Appendix D) (NDOT 2010). There are four continuous Automatic Traffic Recorder (ATR) count locations on highways SR-431, SR-28, and US-50 in the Nevada portion of the Lake Tahoe Basin. Monthly Average Daily Traffic (*MADT*) data in the winter snow season were obtained from these ATR stations. Unfortunately, the ATR locations are not representative of the traffic in the major route sections in the forested area. Therefore, only the basin-wide mean *MADT* in the winter snow season was used. Specific traffic speed information on snow-covered roads or at the time of de-icing salt application was not available, and therefore was not considered.

2.2.6 Climate data

Historical precipitation (including snowfall) data (Appendix E) for the Nevada side of Lake Tahoe were obtained from archives of three weather stations (SNOTEL sites) maintained by the USDA Natural Resource and Conservation Service (NRCS) National Water and Climate Center. The three SNOTEL sites are: (1) Marlette Lake, Nevada, latitude: 39°10'N, longitude: 119°54'W, elevation: 7880 feet; (2) Mt. Rose Ski Area, Nevada, latitude: 39°19'N, longitude: 119°54'W, elevation: 8801 feet; and (3) Heavenly Valley, California (very close to the state line of Nevada and California), latitude: 38°55'N, longitude 119°55'W, elevation: 8582 feet. These sites nearly represent the northernmost, middle and southernmost locations in the study area.

2.3 Remote Sensing Methodology

Remote sensing data were thoroughly preprocessed and then used to derive tree crown mortality information according to the flow of operations outlined in Figures 3 and 4. Remote sensing derived mortality provided the data source for statistical analyses on road-related effects. LiDAR data were processed to be used for several purposes including IKONOS orthorectification, topographic and hydrological variables generation, tree crown projection and delineation, and estimation of tree height. For IKONOS images, a full preprocessing procedure was conducted including orthorectification, preliminary radiometric calibration, the SCnS+C topographic correction and the IR-MAD radiometric normalization (Figure 3). These processes will be described in detail in the following sections. For Landsat TM images, the preprocessing was simpler because geometric correction had already been completed to a high level by USGS. The preliminary calibration tool for Landsat TM imagery was also available in ENVI software. Dark-object subtraction was performed to minimize haze effects and IR-MAD method was used

to radiometrically normalize the whole stack of Landsat TM images (from 1990 to 2009) to the reference image of 2010 (Figure 4). After the satellite data were preprocessed, different vegetation indices were calculated using the multispectral bands and were compared based on their ability to predict field-measured LAI. The most suitable vegetation index (VI) was selected to calibrate a VI-LAI relationship, which was used to transform remote sensing VI values to LAI data. Tree crown mortality was derived by the change in LAI of different years in quantitative change detection or by the "from-to" change class in post-classification change detection. A separate dataset of field surveyed mortality was finally used to validate the remote sensing derived mortality, which was then analyzed statistically in the application component of this study to assess road-related effects on tree crown mortality in the Lake Tahoe Basin.

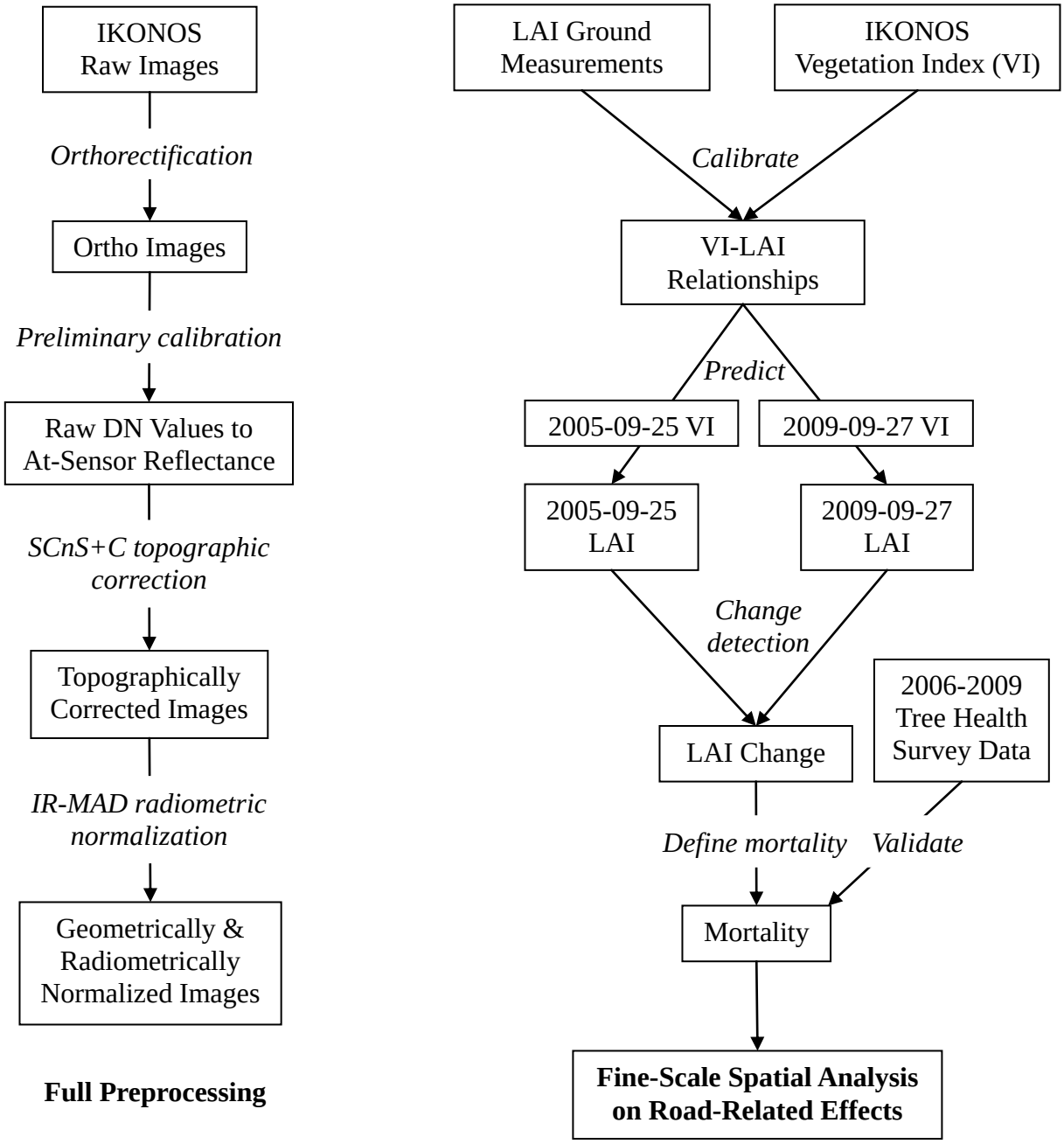

Figure 3. Flow chart of IKONOS image preprocessing, remote sensing change detection, calibration, validation, mortality derivation, and statistical analysis processes.

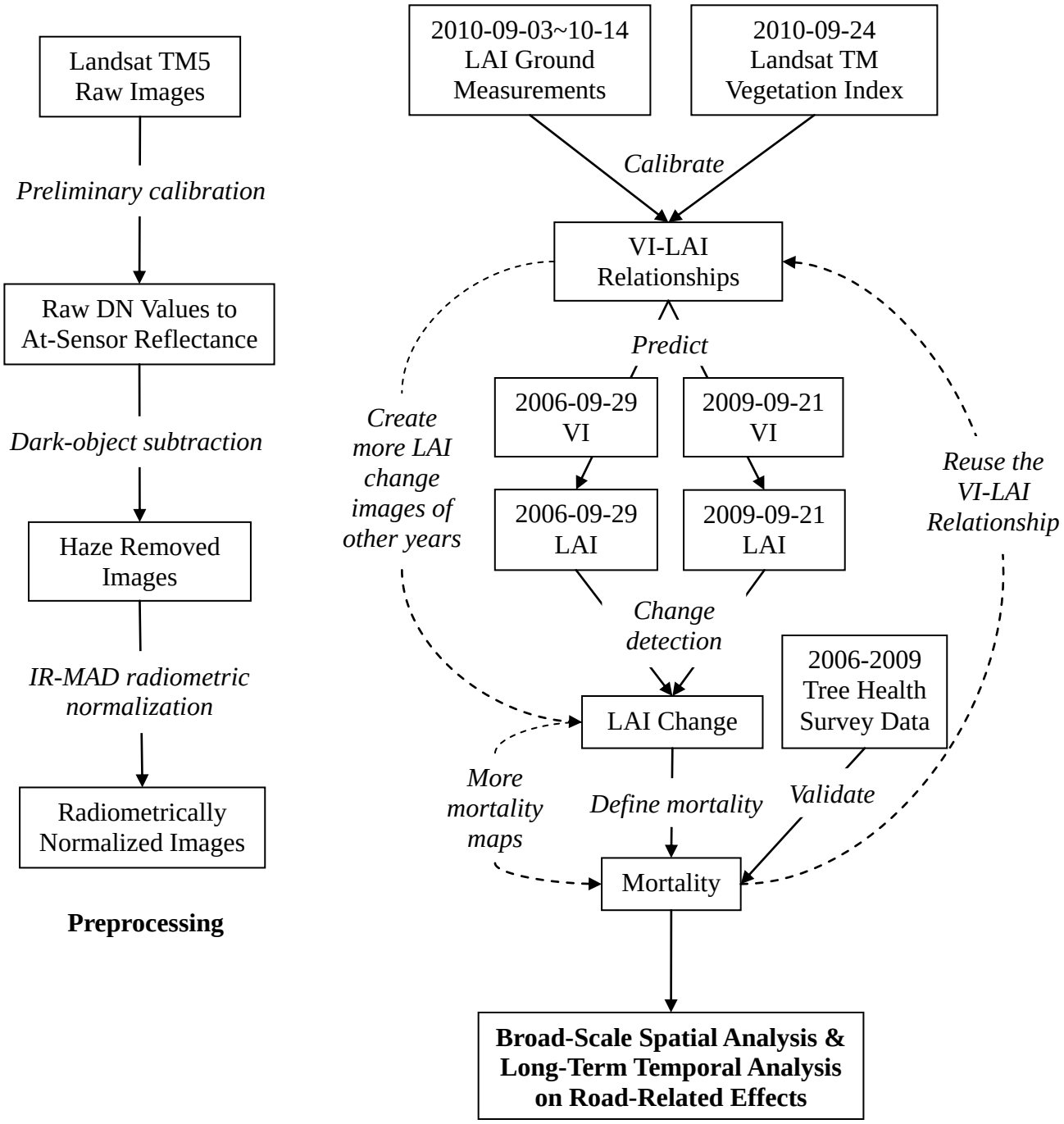

Figure 4. Flow chart of Landsat TM image preprocessing, remote sensing change detection, calibration, validation, mortality derivation, and statistical analysis processes.

2.3.1 LiDAR Data Processing

A novel method in the utilization of LiDAR data was to create binary raster images of tree crown shapes as viewed from different positions of the IKONOS sensor. These images were used as masks in many steps involving distinguishing tree crowns from other, potentially confounding land cover types. A simple image of tree crowns can be derived from LiDAR data by differencing its DSM and DEM. A lower threshold of 3 m difference in height was used to differentiate tree crowns from other land cover types on this DSM-DEM difference image. Yet there was an average of 6 m offset between the tree crowns on LiDAR derived image and the corresponding tree crowns on IKONOS image, because LiDAR records true spatial locations of round-shaped tree crowns by laser pulses whereas IKONOS records optically projected oval-shaped crowns given its non-nadir view angles. Therefore, a projection method using the Hillshade tool of ArcGIS and LiDAR DSM (including tree crown height) was employed to create an image of tree crown shapes that match those on IKONOS images. In this projection, the inputs of sun elevation angle and sun azimuth angle, as typically used in applications of the Hillshade tool, were substituted by IKONOS satellite collection angles so that the modeled tree "shadows" were actually the projected tree crowns on the IKONOS image plane (Figure 5).

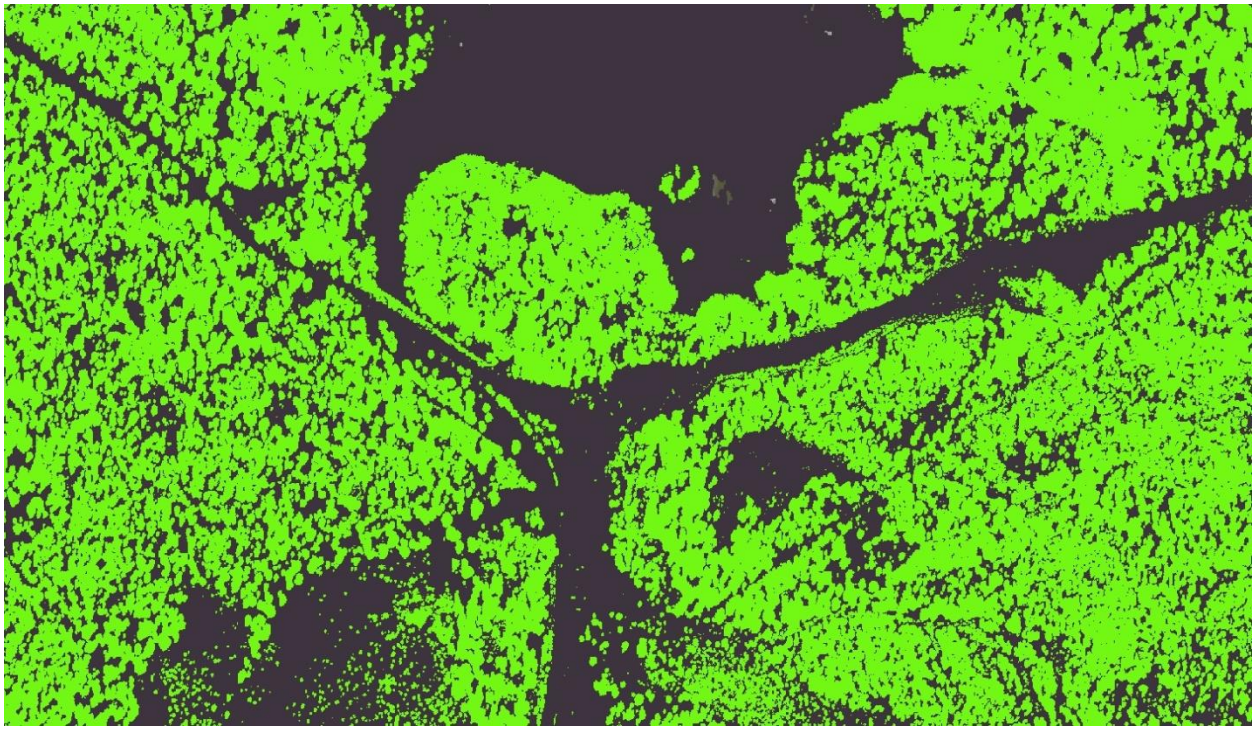

Figure 5. LiDAR tree crown mask that matches 2005-09-25 and 2009-09-27 IKONOS image projection.

2.3.2 Satellite Imagery Processing

2.3.2.1 Geometric Correction

Geometric correction of multi-temporal satellite images is necessary for remote sensing change detection. This study related remote sensing-derived information to field survey data and other thematic information in a geographic information system (GIS). Therefore, high geometric accuracy within image and between images was needed. Orthorectification and image-to-image registration are two common geometric correction procedures. Landsat TM5 images from USGS were collected with near nadir view angles and have already been processed to Level 1T, which provides systematic radiometric and geometric accuracy by incorporating ground control points (GCP), while also employing a Digital Elevation Model (DEM) for topographic accuracy. After comparison with a DOQ image, most of the archive Landsat TM5 images were found to have

high geometric accuracy and were consistent with each other (within half-pixel uncertainty). The geometric accuracy was further validated by GCPs collected with high precision Trimble GeoXT GPS and LiDAR. Thus, no further geometric correction was performed on Landsat images.

IKONOS raw images purchased from GeoEye were collected with non-nadir view angles and were preprocessed only to the Geo level (GeoEye 2011), which provides standard geometric correction with 15 meter CE90 accuracy. Geometric distortion caused by the terrain was apparent in these images. Objects (e.g. tree crowns) on different images were not matched. In order to perform pixel-based change detection and co-register tree crowns (with a similar size to a 4-m pixel) on different images, as well as to relate individual trees from the field plots to the images, further geometric correction by orthorectification was necessary. The IKONOS images were accompanied by Rational Polynomial Coefficients (RPC) files that enabled orthorectification using an RPC model with a DEM and additional GCPs (Lutes 2004).

To achieve high accuracy, two orthorectification approaches were compared: 1) a two-step approach combining generic RPC orthorectification and image-to-image registration using ENVI, and 2) a one-step approach using ERDAS IMAGINE, in which the original RPC correction model was refined with a 0 order polynomial adjustment using GCPs and then the refined model was applied to orthorectify the image in one step. In the two-step approach, terrain effects were first eliminated in the resulting RPC-orthorectified image, but there was still horizontal offset in the X and Y dimensions relative to the standard DOQ, due to a lower degree of accuracy of the rational polynomial camera model than the physical camera model. A 0 order polynomial correction in image-to-image registration was then applied to eliminate this offset using GCPs from reference image. Comparing these two approaches, it was discovered that even though the two-step approach

had similar results to that of the one-step approach, they were not identical. The one-step approach is theoretically more reasonable and accurate. The following graph illustrates their difference.

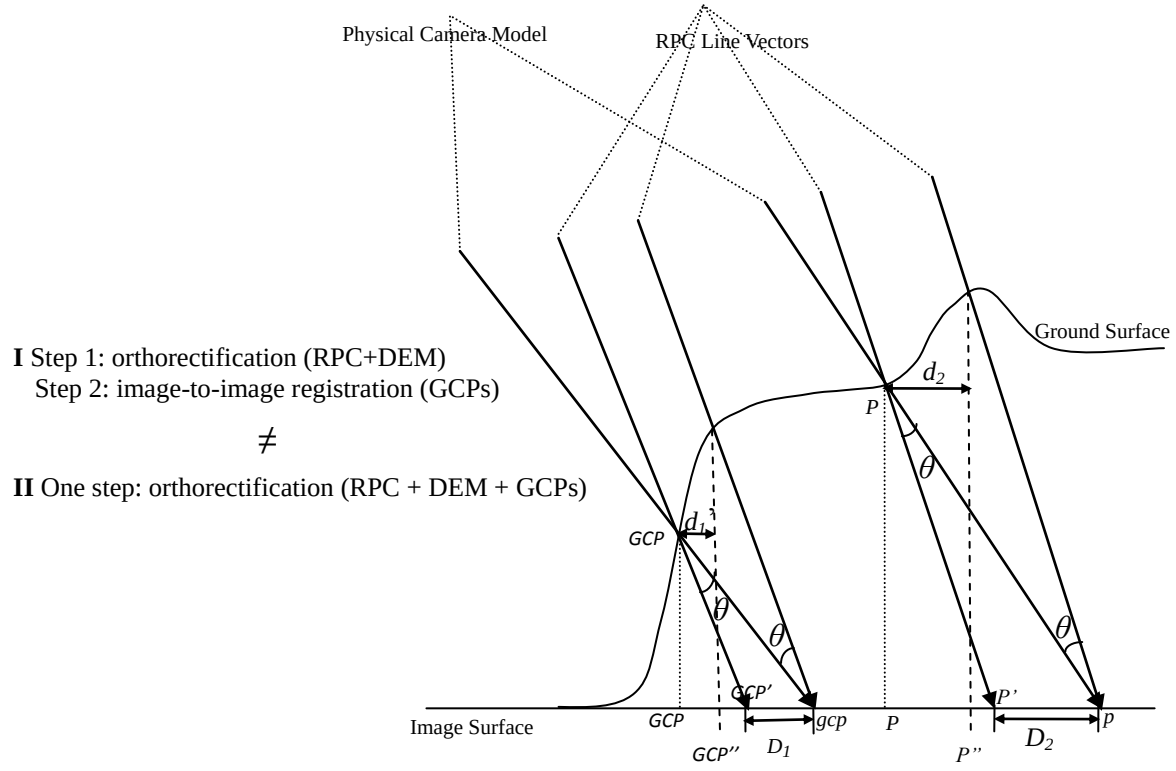

Figure 6. Difference between two orthorectification approaches. *D* refers to distance. *GCP* is the ground control point. *P* is the uncorrected image point.

On the above graph, assuming a 0 order polynomial adjustment (i.e. a simple shift to image x and y coordinates), RPC is used in two ways in the orthorectification process of method **II**. First, RPC is used to compute the model solution by projecting the 3D reference *GCPs* (i.e. X, Y, Z coordinates of *GCP*) onto a 2D image surface (i.e. x, y coordinates of *GCP'*) and determining polynomial adjustment (i.e. value of D_1) by relating the transformed 2D coordinates of *GCP'* to the coordinates of image tie-point *gcp* (i.e. uncorrected pixel position corresponding to the *GCP*). The D_1 adjustment is then applied to adjust all image points (e.g. from *p* to approximately *P'*, $D_1 \approx D_2$). Another role of RPC is to transform in the final stage, in an opposite

direction, all the image coordinates (*p*) after polynomial adjustment (*P'*) into orthorectified locations (*P*) using elevation information from the DEM.

Method **I** works by transforming *gcp* to *GCP"* and *p* to *P"* using RPC and DEM in the first step, and then adjusting *GCP"* to *GCP* by d_1 ($d_1 \neq D_1$) in the second step, image-to-image registration. The d_1 adjustment derived from *GCPs* is finally applied to register all image points. *P"* cannot be adjusted to *P* by the d_1 adjustment ($d_1 \neq d_2$) due to the variation in topography. Moreover, for method **II** the effect of *GCP* location on the correction of other pixels depends only on the elevation (bias = $|D_2 - D_1|$; D_1 and D_2 are proportional to elevation) because RPC bias angle θ is the same for small ground region and the image surface is level. This effect is minimized when multiple *GCPs* with different elevations are used; whereas for method **I**, the bias in correcting other pixels depends on the slope as well as the elevation around *GCPs* and other pixels (bias = $|d_2 - d_1|$; d_1 and d_2 are determined by both elevation and slope) because of the uneven ground surface, even though θ keeps the same. In the situation shown in the above graph, the bias of method **I** ($|d_2 - d_1|$) is larger than that of method **II** ($|D_2 - D_1|$). They can only be equal to each other when the terrain is flat. Therefore, in rugged terrain, method **II** has less random error than method **I** and thus can generate more accurate orthoimages.

Based on the above findings, the one-step approach was taken to orthorectifying IKONOS images, with the aid of the high accuracy LiDAR DEM and GCPs collected from the field using sub-meter precision Trimble GPS. LiDAR first return surface DSM provides accurate elevation information of tree crowns, instead of bare terrain elevation. If this DSM is used in the orthorectication of IKONOS images, tree crowns can be orthorectified to the true spatial position. However, resampling the projected oval-shaped tree crowns (because of non-nadir satellite view angles) into round-shaped crowns (because LiDAR records true spatial locations by laser pulses)

causes drop of tree crown pixels, because the orthorectified round-shaped crowns generally have less area compared to the projected oval-shaped crowns. Tree crown pixels in the IKONOS image can be considered as tree crowns projected together with their below canopy ground surface along the viewing direction onto the image surface. In other words, since all the materials within the sensor's instantaneous field of view (IFOV) are finally projected onto a single surface, the tree crowns can be considered as lying on the ground along the sensor's viewing direction. Therefore, in order to achieve high geometric accuracy as well as preserve the shape and original pixels of tree crowns, the LiDAR DEM of continuous and smooth bare terrain surface was used to orthorectify IKONOS images. As long as the DEM surface is continuous and smooth, the tree crown geometry on raw image will be preserved. The accuracy and smoothness of LiDAR DEM surface can minimize the errors of duplication (on terrain surfaces facing away from the sensor) and omission (on terrain surfaces facing the sensor) of tree crown pixels.

In order to achieve accurate co-registration between different images and between panchromatic and multispectral images of the same imagery, several guidelines were followed:

(1) Choose GCPs with accuracy < 1m, whose tie points are clearly identifiable on the image;
(2) Once the GCP tie points on the image were located with confidence, they should not be moved in order to decrease the RMS error;
(3) Locate each GCP tie point for all the images at the identical pixel (by carefully comparing the pixel patterns around each tie point on different images) and always at the pixel center/corner or pixel edge center on the panchromatic image by precise coordinates, so that it has the effect of bundle adjustment to ensure co-registration between images.

(4) Preserve the co-registration between panchromatic and multispectral images of the same imagery, by setting correct upper-left origin X and Y coordinates of the 4-m multispectral image in the output resampling configuration, according to those of the 1-m panchromatic image. If using the calculated defaults by the program, the original co-registration between raw panchromatic and multispectral images will be lost.

(5) Choose 0 order polynomial adjustment which is adequate for the images within 100km and requires only a few precise GCPs.

The 2005-09-25 and 2009-09-27 images were the only pair selected for change detection for their closest collection angles and sun angles. The overall RMS errors were 0.1502 and 0.2077 pixel for 2005-09-25 and 2009-09-27 panchromatic images, and 0.0376 and 0.0519 pixel for their multispectral images, respectively. Pixels of 2005-09-25 and 2009-09-27 panchromatic images were precisely matched after orthorectification. Their panchromatic and multispectral images were kept matched as well. But unfortunately, the multispectral images have 2-m offset, because the original multispectral images of these two dates were scanned and sampled from different origins which have 2-m difference in latitude. This 2-m offset was a true offset during image collection and remained after orthorectification if the same pixel size (4m) was used as resampling size. Considerations of different resampling methods and resampling sizes in the output configuration in order to deal with this offset are discussed in the following section.

2.3.2.2 Resampling

Two resampling methods were employed in the orthorectification, nearest neighbor and cubic convolution. Nearest neighbor resampling was used in orthorectifying each IKONOS multispectral image with reference to the respective true origin. This maintained the spectral

characteristics of the data without smoothing across extreme values, which is important for deriving the relationship between LAI and vegetation index and for image classification.

Cubic convolution resampling was used to match the 2005 multispectral image with the 2009 reference multispectral image. Because of the 2-m (half-pixel) difference in their original scan and sample origins, this resampling using the same grid origin (upper left corner X and Y coordinates) was necessary for co-registering pixels for pixel-based change detection between 2005 and 2009. However, it alters the original radiometric information in the pixels and thus can be problematic for image classification (Meyer 1992).

Another reason to use cubic convolution was that due to the slight difference in view angles between 2005-09-25 and 2009-09-27 images (2.44° in zenith and 17.31° in azimuth), there was a shift of 1.6 m Easting and 1 m Northing in projected tree crown top position between these two images for trees with average height of 14.7 m (derived from LiDAR) in the Nevada portion of Lake Tahoe Basin. A downgrading of resolution to 6 m was used to accommodate this spatial difference in tree crown projection on the images, which also corresponds to the default resampling pixel size suggested by ERDAS software as the optimum resolution that neither oversamples nor undersamples the input image space (ERDAS 2010). The IKONOS images resampled in this way were used in the quantitative change detection method (Section 2.3.6).

2.3.2.3 Preliminary Radiometric Calibration

Raw DN values were initially calibrated to at-sensor reflectance for each image band. Calibrated reflectance is recommended for any analysis that involves quantitative comparison of different scenes. It standardizes the bands, accounts for drift in the multispectral scanner, and

normalizes daily variation in sunlight (Key and Benson 2004). Calibrated at-sensor radiance and at-sensor reflectance are defined as

$$L_\lambda = \frac{DN_\lambda \times 10}{CalCoef_\lambda \times Bandwidth_\lambda}, \quad (1)$$

$$\rho_\lambda = \frac{\pi \times L_\lambda \times d^2}{ESUN_\lambda \times cos\theta_z}, \quad (2)$$

where,

L_λ = at-sensor radiance (W/m^2/μm/sr),

ρ_λ = at-sensor reflectance,

DN_λ = raw digital number,

d = earth-sun distance in astronomical units,

$CalCoef_\lambda$ = radiometric calibration coefficient [DN/(mW/cm^2-sr)],

$Bandwidth_\lambda$ = Bandwidth of spectral band λ (μm),

$ESUN_\lambda$ = band-dependant mean solar exoatmospheric irradiance (W/m^2/μm),

θ_z = solar zenith angle.

For Landsat images, ENVI provides all the parameters and can automatically transform raw DN values to at-sensor reflectance.

For IKONOS images, there was no software available for the transformation. A transformation model was constructed in ArcMap model builder using the above equation. The values for parameters $CalCoef_\lambda$, $Bandwidth_\lambda$, and $ESUN_\lambda$ were from Taylor (2011). Earth-sun distance was calculated using the Sun-Earth Distance Applet developed by Giesen (2011). At the center of image: Latitude: 39.13, Longitude: -119.93, d=1.0021016 AU for 2009-09-27 18:55 GMT; d=1.0026352 AU for 2005-09-25 19:04 GMT.

This transformation is necessary for the following steps of topographic correction and radiometric normalization. In Key and Benson (2004), the “reflectance incorporating topography” is actually the Cosine Correction method using at-sensor reflectance values instead of raw DN values. Collins and Woodcock (1996) apparently used at-sensor radiance as input for normalization and then transformed matched radiance to reflectance, which involved potential error because what should be normalized is the stable reflectance of invariant features, but not their radiance which is not constant even for the most invariant features because of solar variation. At-sensor radiance is the spectral radiance recorded by the sensor. At-sensor reflectance is calculated using at-sensor radiance and accounts for the variance caused by differences in exoatmospheric solar irradiance arising from spectral band differences, the cosine effect of different solar zenith angles, the approximate cosine effect of different view angles and small differences in the sun-earth distance. Calibrated reflectance standardizes the spectral bands within a scene as well as normalizes variation in sunlight and viewing geometry between scenes. This allows the bands to be compared directly and allows more accurate vegetation indices to be derived.

Compared to Landsat TM data, retrieving at-sensor reflectance for multitemporal IKONOS imagery is complicated by its off-nadir view angle. The magnitude of radiance recorded by the IKONOS sensor is dependent on several factors (Mather 1999): (1) reflectance of the target; (2) atmospheric effects; (3) topographic (terrain slope and aspect) effects; (4) solar zenith angle and exoatmospheric solar irradiance; and (5) view angle (zenith and azimuth) of the sensor.

Vegetation indices and change detection are based on examining the target reflectance (factor 1) and its change at different points of time. Therefore, factors 2-5 have to be corrected or normalized in order to derive unbiased reflectance. Since I took separate steps for atmospheric

correction and topographic correction, I can assume the absence of an atmosphere and a flat terrain. In addition, the terms: d^2, $ESUN_\lambda$, and $\cos\theta_z$ in equation (2) already normalize incoming solar irradiance received at a pixel. The magnitude of at-sensor radiance still varies with sensor view angle (zenith and azimuth), given that vegetated land cover is not Lambertian. The effect of off-nadir viewing geometry on observed radiance is termed the Bidirectional Reflectance Distribution Function (BRDF) (Mather 1999, Jenson 2000). For forested land, this issue is complicated by many factors such as tree species, canopy structure, and understory background.

The variation associated with BRDF due to slight difference in view angles between the 2005-09-25 and 2009-09-27 images (2.44° in zenith and 17.31° in azimuth) can be further normalized in the following topographic correction and radiometric normalization processes but it cannot be completely eliminated. Different change thresholds were set in the later steps in order to exclude this effect and other unexplained variation from statistical analyses.

2.3.2.4 Radiometric Correction of Topographic Effect

Because of the complex topography (steep slopes and various aspects) in the study area, topographic distortions on the radiometric property of the imagery (both Landsat TM and IKONOS) are evident. The same canopies on different slopes will have different radiometric information recorded by the raw imagery. Topographic correction is necessary to normalize sloped pixels to horizontal pixels so that they have equivalent radiance on the image if there are equivalent actual materials of interest on the ground within their instantaneous fields of view (IFOVs) (Colby 1991). Many topographic correction methods have been created. This study developed a new Sun-Crown-Sensor (+C) model for correcting topographic effects in forest imagery. The derivation of this model and comparison with other models are presented as follows.

(1) Previous methods

Through comparison of two common topographic correction methods: Cosine Correction and C-Correction (Jensen 2005), I found the latter to be a significant improvement over the former one which showed obvious overcorrection. The C-Correction algorithm is defined as:

$$\rho_0 = \rho\ (\frac{cos\ \theta z + C}{cos\ i + C}), \tag{3}$$

where ρ_0 is the topographically corrected reflectance as if on horizontal terrain; ρ is the uncorrected reflectance; i is the solar incidence angle defined as the angle between the normal to the pixel surface and the solar zenith direction; θz is the solar zenith angle; and C is a parameter analogous to the general additive effects of diffusive sky irradiance (Teillet 1982). Without C, equation (3) is the Cosine Correction. C is calculated from an empirical-statistical regression model

$$\rho_k = b_k + m_k\ cos\ i, \tag{4}$$

$$C_k = b_k / m_k, \tag{5}$$

where ρ is the raw image reflectance, m and b are the slope and intercept of the regression line, and the subscript k specifies band k. If the whole image is used to derive C_k, the method is called *general C-Correction;* if a specific land cover type is used to derive C_k, the method is called *specific C-Correction* (Kobayashi and Sanga-Ngoie, 2009). *Specific C-Correction* can significantly enhance the accuracy of topographic correction for forested pixels. My method was to use the tree crown mask created by LiDAR data (Figure 3) in the above regression to derive *specific* C_k for forest land cover type.

The *Sun-Canopy-Sensor* (SCS) model was developed by Gu and Gillespie (1998) using the following formula

$$\rho_0 = \rho \frac{\cos \alpha \cos \theta z}{\cos i}. \quad (6)$$

where all the parameters are the same as in equation (3), with the addition that α is the terrain slope. This equation normalizes sun-canopy-sensor geometry instead of Sun-Terrain-Sensor (STS) geometry on which many traditional topographic correction methods such as Cosine Correction and C-Correction are based. The SCS method normalizes the sunlit area within a pixel without changing the sun and sensor positions or the orientation, geometry, and structure of the canopy. It is thought to be a more appropriate framework for topographic correction in forested areas. However, even the SCS model overcorrects the radiance for certain terrain features, because it does not characterize diffuse radiation properly, a problem in common with the other methods. Soenen et al. (2005) made a modification to the SCS model to better characterize diffuse irradiance by introducing a semi-empirical moderator C to account for diffuse radiation. This is very similar to the way in which C-Correction improves upon the Cosine Correction. The formula for the SCS+C correction is

$$\rho_0 = \rho \left(\frac{\cos \alpha \cos \theta z + C}{\cos i + C}\right). \quad (7)$$

(2) Modified method of deriving C parameter for SCS+C model

Deriving C from equation $\rho_k = b_k + m_k \cos i$ (4) is suitable only for C-correction, which is based on the STS model and assumes a significant correlation between incoming illumination (i.e. cosine of incidence angle) and observed radiance or reflectance. Equation (4) can be transformed to $\frac{\rho_k}{m_k} = C_k + \cos i$, where the denominator m_k normalizes the image data DN, radiance or reflectance, and then obviously $\cos i$ is the single controlling factor of pixel values with a constant slope 1. The constant $C_k = b_k/m_k$ is analogous to the general additive effect of indirect illumination from the sky.

However, for SCS+C, the understanding of the relationship between incoming solar illumination and observed signal is based on the SCS model but not the STS model. C parameter, therefore, should be derived using another equation representing the correct correlation of observed signal to Sun-Canopy-Sensor geometry. As found by Gu and Gillespie (1998), both the average irradiance hitting on and the average radiant exitance from the sunlit part of the canopy are largely independent of topography because of the geotropic character of trees, and the total radiance from the sunlit part of the canopy is proportional to its area:

$$\frac{\rho}{\rho_0} = \frac{L}{L_0} = \frac{A}{A_0} = \frac{cos\, i}{cos\, \alpha\, cos\, \theta z}. \quad (8)$$

Given a fixed solar zenith angle θ_z, sensor recorded radiance is further influenced by terrain factor $\frac{\cos i}{\cos \alpha}$. Therefore, the following equation describes the correlation between the terrain-controlled incoming illumination on forest canopy and observed radiance in each band.

$$\rho_k = b_k + m_k \frac{cos\, i}{cos\, \alpha}, \text{ or}$$

$$\frac{\rho_k}{m_k} = C_k + \frac{cos\, i}{cos\, \alpha}. \quad (9)$$

Equation (9) should be used instead of equation (4) to derive the *C* parameter in the context of the forest canopy and Sun-Canopy-Sensor model. The equation $C_k = b_k/m_k$ still holds and emulates the general additive effect of diffusive sky irradiance on tree canopies, but the independent variable changes from $\cos i$ to $\frac{\cos i}{\cos \alpha}$ in the regression. This new method of deriving the C parameter should be used in equation (7) for *Sun-Canopy-Sensor + C* topographic correction.

(3) Sun-Crown-Sensor model

For IKONOS imagery, the topographic effects are not likely to correlate well with the Sun-Terrain-Sensor geometry (Gu and Gillespie 1998), because IKONOS has 4-m spatial resolution, whereas the mean diameter of tree crowns in the Lake Tahoe Basin is 10 to 15 m. Moreover, the Sun-Canopy-Sensor topographic correction model by Gu and Gillespie (1998) should be further modified to characterize the tree crown's, instead of canopy's, sunlit area within IKONOS sensor's non-nadir instantaneous field of view (IFOV) as a function of sun, crown and sensor geometry (Sun-Crown-Sensor). Topography takes on a different importance from the Sun-Canopy-Sensor model to the Sun-Crown-Sensor model. According to Gu and Gillespie (1998), topography controls the relative positioning of trees that are geotropic and thereby regulates mutual shadowing and the total area of sunlit portions of canopy within Landsat TM's IFOV, which is viewed from near-nadir. For IKONOS, topography does not affect either the irradiance or exitance related to direct illumination on sunlit portions of individual tree crowns, but it does affect mutual shadowing and thus the total area of sunlit portions of crown in each pixel/IFOV in continuous canopy.

The aim of topographic correction is to normalize sloped pixels to horizontal pixels so that they have equivalent radiance information on the image as well as equivalent actual materials of interest on the ground within their IFOVs. For this study, the materials of interest are green leaves, in terms of LAI. This was measured from a base area parallel to the slope surface, instead of from horizontal. In theory, a pixel on slope and a pixel on flat ground, having the same LAI (dimensionless), should contain the same amount of radiance after topographic correction, free from the effects of varying sun-crown-sensor geometry and varying IFOV area on the ground, so that they are comparable both on the ground and on the image.

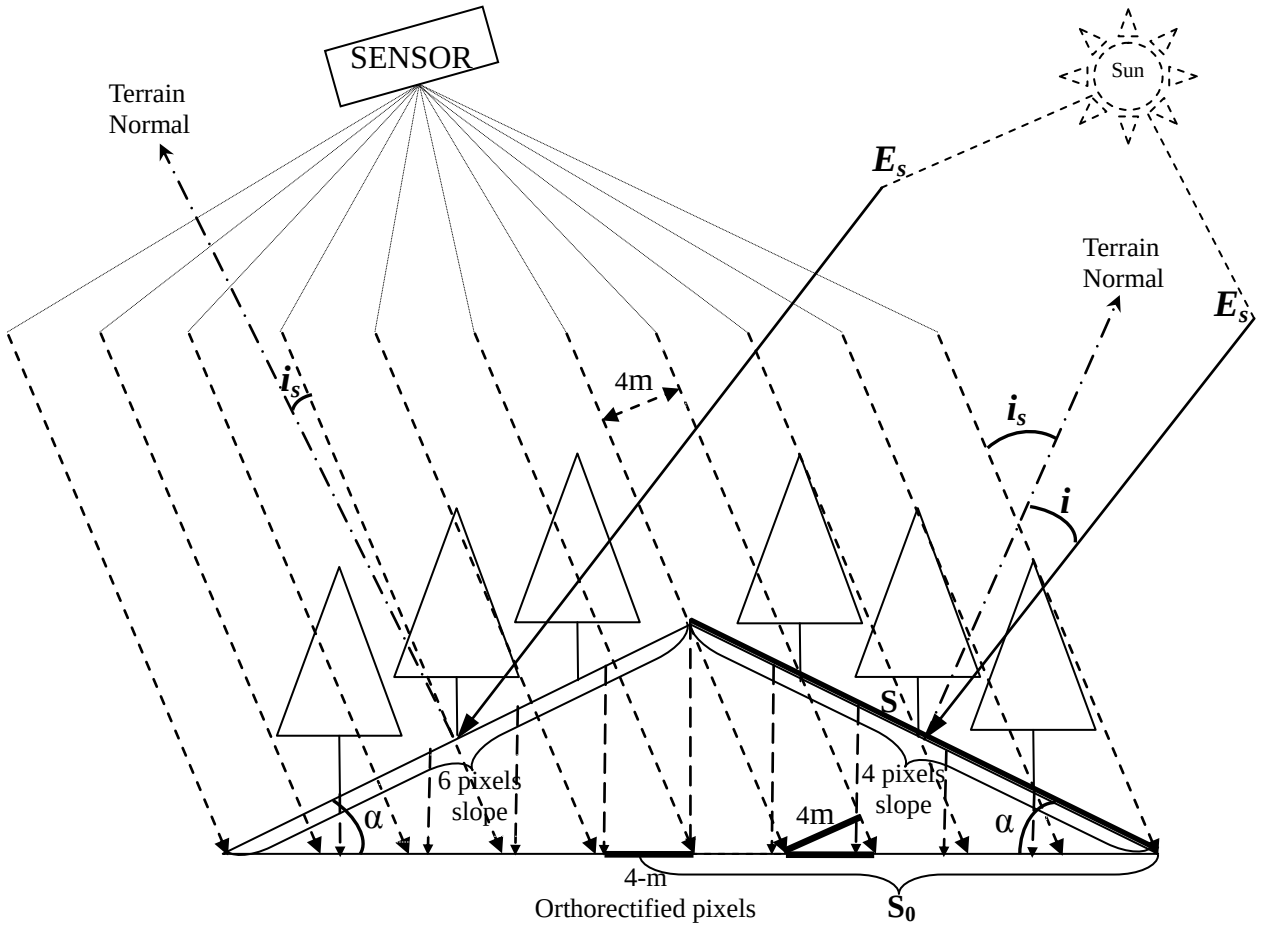

Figure 7. The Sun-Crown-Sensor topographic correction model.

Based on the above understanding, considering a continuous canopy with area *S* and mean *LAI* on sloped terrain consisting of *n* pixels, and ignoring the complication of varying tree species, tree density, tree height and tree crown shape, the total sunlit canopy area in these pixels is

$$A = \frac{E_s S \cos i}{I}, \tag{10}$$

where E_s is the incoming solar irradiance, and *i* is the solar incidence angle over the terrain surface (Figure 7). The numerator of equation (10) is the total solar radiation energy intercepted by the surface element covered by canopy *S*. The denominator *I* is the average irradiance on the sunlit part of the canopy that is largely topography-independent. Assume an equivalent canopy S_0 on

horizontal terrain, which has the same mean and standard deviation of *LAI* within its pixels. Tree crown properties of this canopy are unchanged except that the relative distance and position between the upright (geotropic) tree crowns changes from sloped to horizontal terrain. Therefore, S_0 should approximate but not be identical to *S*, given the same frequency distribution of *LAI*. Then the total sunlit area of the canopy becomes

$$A_0 = \frac{E_S S_0 \cos\theta_z}{I}, \tag{11}$$

where θ_z is the solar zenith angle. The number of pixels to cover this canopy becomes n_0, and

$$\frac{n_0}{n} = \frac{S_0 \cos\theta_s}{S \cos i_s}, \tag{12}$$

where θ_s is the sensor zenith angle and i_s is the angle between the normal to the pixel surface and the sensor zenith direction. Therefore, in each canopy pixel the average sunlit crown area on sloped terrain A_p and on horizontal terrain A_{p0} are related to each other through

$$\frac{A_p}{A_{p0}} = \frac{A/n}{A_0/n_0} = \frac{\cos i \cos\theta_s}{\cos i_s \cos\theta_z}. \tag{13}$$

If I neglect the BRDF effect and given the same *LAI*, the average radiance reflected from the sunlit part of the crown in a pixel is also largely independent of topography. If I further ignore the relatively small amount of radiance from the shadowed portion of the crown, the average total radiance *L*, and the reflectance ρ, recorded by each pixel is proportional to the average sunlit area of crown within each pixel's IFOV, that is,

$$\frac{\rho}{\rho_0} = \frac{L}{L_0} = \frac{A_p}{A_{p0}} = \frac{\cos i \cos\theta_s}{\cos i_s \cos\theta_z}, \text{ or} \tag{14}$$

$$\rho_0 = \rho \frac{\cos i_s \cos\theta_z}{\cos i \cos\theta_s}, \tag{15}$$

where ρ is the uncorrected reflectance value on any terrain and ρ_0 is the topographically corrected reflectance value as if on horizontal terrain. I refer to equation (15) as the Sun-Crown-Sensor (SCnS) topographic correction model (Figure 7). Although it is derived for the average of pixels of a canopy, it can be used to topographically correct every specific pixel of canopy *S* on sloped terrain. Since the numbers of pixels covering canopy *S* and S_0 are different and there are varying mutual shadowing effects among adjacent pixels, I cannot identify an equivalent pixel from canopy S_0 for every specific pixel of canopy *S*. So I can only assess the mean and standard deviation of pixels of canopy *S* and S_0 before and after correction. After this model is applied to all pixels, not only the mean reflectance of canopy *S* is adjusted to the same as canopy S_0 but the standard deviation of reflectance of corrected pixels of canopy *S* also matches that of canopy S_0. This meets the objective of topographic correction (Civco 1989, Riano et al. 2003).

The method of deriving Sun-Canopy-Sensor model based on coarse-resolution pixels from Gu and Gillespie (1998) cannot be directly applied to a high-resolution image especially with continuous canopy, because the total solar radiation energy intercepted by a pixel surface element is not only controlled by the pixel's area projected in the direction of sun radiation but also affected by shadowing from adjacent pixels when the pixel is smaller than a tree crown. Thus, the equation used in Gu and Gillespie (1998), $\varepsilon = E_s S_p \cos i$, where S_p is the area of a pixel on slope, does not hold for continuous forest pixels on IKONOS image. Therefore, the logical flow presented above beginning with the consideration of a canopy consisting of *n* pixels is theoretically well-founded and is necessary for deriving the Sun-Crown-Sensor model in this study. It also allows the derivation and consideration of other models and factors as in the following sections (4) and (5).

As for isolated tree crowns or sparse canopy, the corresponding individual pixels (containing mainly tree crowns in their IFOV) are free from shadows and the equation $\varepsilon = E_s S_p \cos i$ largely holds. Equations (10) and (11) can be adopted and modified to

$$A_p = \frac{E_s S_p \cos i}{I}, \tag{16}$$

$$A_{p0} = \frac{E_s S_{p0} \cos \theta_z}{I}, \tag{17}$$

where $S_p = {}^{4}/_{\cos i_s}$ and $S_{p0} = {}^{4}/_{\cos \theta_s}$. Therefore,

$$\frac{\rho}{\rho_0} = \frac{L}{L_0} = \frac{A_p}{A_{p0}} = \frac{\cos i \cos \theta_s}{\cos i_s \cos \theta_z}, \tag{18}$$

which is the same as equation (14). This means, the Sun-Crown-Sensor model is generally applicable to both continuous and sparse canopies, as long as the pixels are covered mainly by tree crowns.

Compared to the Sun-Canopy-Sensor model in Gu and Gillespie (1998) which does not consider varying sensor geometry, this Sun-Crown-Sensor model can be considered as a full model involving all aspects of the Sun-Crown/Canopy-Sensor geometry. It is developed in the context of high resolution (sub-crown) imagery with non-nadir view angles, but it is also applicable to other forest imagery with different resolutions and different view angles (including nadir). For example, for Landsat TM5 imagery, the sensor has nadir view and thus $\theta_s = 0$ and $i_s = \alpha$ (terrain slope). Therefore, equation (15) becomes equivalent to equation (6) in this situation.

To further incorporate the function of C-correction into this newly derived Sun-Crown-Sensor model, I follow the same theory in previous section (2). From equation (14), I know that sensor recorded radiance is controlled by terrain factor $\frac{\cos i}{\cos i_s}$, when the solar zenith angle θ_z and

sensor zenith angle θ_s are fixed. Therefore, the following equation describes the correlation between the terrain-regulated incoming illumination on tree crowns and the observed radiance in each band.

$$\rho_k = b_k + m_k \frac{cos\, i}{cos\, i_s} \tag{19}$$

Equation (19) should be used instead of equations (4) and (9) to derive the *C* parameter in the context of forest image and Sun-Crown-Sensor model. $C_k = b_k/m_k$ still holds and emulates the general additive effect of diffusive sky irradiance on tree crowns. Therefore, the Sun-Crown-Sensor + C topographic correction model is formulated as:

$$\rho_0 = \rho \frac{\cos i_s \cos \theta_z + C}{\cos i \cos \theta_s + C}. \tag{20}$$

(4) Normalize solar angle and sensor angle effects

Equations (15) and (20) normalize topographic effects of varying terrain slopes and aspects within a scene. Following the same theory and procedure in deriving equation (15), I can devise another formula to normalize between-scene variance caused by different solar angles and sensor view angles. After topographic correction, all pixels can be considered as if on horizontal terrain. Therefore, equations (10), (12), (13), (14) and (15) can be written as follows:

$$A_{0\prime} = \frac{E_{s\prime} S_0 \cos \theta_{z\prime}}{I}, \tag{21}$$

$$\frac{n_0}{n_{0\prime}} = \frac{S_0 \cos \theta_s}{S_0 \cos \theta_{s\prime}} = \frac{\cos \theta_s}{\cos \theta_{s\prime}}, \tag{22}$$

$$\frac{L_{0\prime}}{L_0} = \frac{A_{p0\prime}}{A_{p0}} = \frac{A_{0\prime}/n_{0\prime}}{A_0/n_0} = \frac{E_{s\prime} \cos \theta_{z\prime} \cos \theta_s}{E_s \cos \theta_{s\prime} \cos \theta_z}, \tag{23}$$

$$\frac{\rho_{0\prime}}{\rho_0} = \frac{{L_{0\prime}}/{E_{s\prime}\cos\theta_{z\prime}}}{{L_0}/{E_s\cos\theta_z}} = \frac{\cos\theta_s}{\cos\theta_{s\prime}}, \quad (24)$$

$$\rho_0 = \rho_{0\prime}\frac{\cos\theta_{s\prime}}{\cos\theta_s} \quad (25)$$

where subscripts *0'*, *s'* and *z'* specify the pixels on horizontal terrain (topographically corrected) of the image to be normalized and *0*, *s* and *z* specify those of the reference image. *Es* is the incoming solar irradiance at-sensor ($E_s = \frac{ESUN}{\pi d^2}$) which has already accounted for variation in *d* the earth-sun distance in astronomical units. ρ_0 in equation (25) is the normalized reflectance. Comparing equation (23) and (24), it is more convenient to normalize at-sensor reflectance ρ than at-sensor radiance *L*, because the between-scene variance in incoming solar irradiance has already been normalized in the preliminary radiometric calibration. Although equation (23) is developed to normalize both the sensor view angle and solar angle effects, equations (24) and (25) are sufficient to minimize the remaining portion of image-to-image variance in at-sensor reflectance caused only by different sensor zenith angles, after the previous steps of preliminary radiometric calibration and topographic correction have been performed.

(5) Sun-Crown-Sensor model incorporating orthorectification

After orthorectification and resampling have been accounted for, it remains to reconsider the formulation of the Sun-Crown-Sensor model. The orthorectification process transforms an image with terrain distortion from an off-nadir-viewing system into an orthoimage with relief displacements removed as if viewed from nadir. However, orthorectification can only correct for geometric distortion caused by terrain and view angle effects, while the Sun-Crown-Sensor (+ C) topographic correction normalizes the radiometric distortion caused by terrain, canopy, sun angle

and sensor view angle effects. It can, therefore, be labeled a radiometric-topographic correction to be distinguished from geometric corrections.

I used two resampling methods: Nearest Neighbor and Cubic Convolution. Nearest Neighbor resampling alters the number of pixels to cover the canopy *S* or S_0, because of duplication of pixels (e.g. same pixel size) on slopes facing away from the sensor and dropping of pixels on slopes facing the sensor after orthorectification, as illustrated in Figure 7. Nevertheless, the radiance recorded by each pixel is unaltered. Therefore, the Sun-Crown-Sensor model as expressed by equations (13), (14), and (15) should be maintained.

Cubic Convolution interpolates pixel values based on a 4 × 4 window of neighbors. It has an effect analogous to averaging out the radiance of pixels covering the canopy *S* or S_0. The number and values of pixels covering the canopy are altered after orthorectification. However, the mean and standard deviation of the output pixels match the mean and standard deviation of the input pixels closely with this resampling method (ERDAS 2010). Therefore, the average radiance in pixels of either canopy *S* or S_0 is unchanged after orthorectification. Equations (13), (14), and (15) still hold.

(6) Model evaluation

First, the alternative approaches were performed to derive the C parameter using equation (4), (9) and (19). The correlation between observed radiance from the tree crowns and terrain-controlled illumination on the tree crowns, that is, $\cos i$, $\frac{\cos i}{\cos \alpha}$, or $\frac{\cos i}{\cos i_s}$ based on the understanding of STS, SCS, and SCnS models respectively, was an indicator of the performance of these models.

Second, following the same procedure as Gu and Gillespie (1998), the Sun-Crown-Sensor model, Sun-Canopy-Sensor model and Sun-Terrain-Sensor model were applied to the test site and statistically evaluated by comparing four parameters:

1. The modeling efficiency (EF) statistic represents the proportion of data variance explained the line of perfect fit (Y = X) when plotting Y against X. The EF is similar to the r^2 statistic but was proposed by Mayer and Butler (1993) as a better overall measure of fit between observed and model simulated values.

2. The squared correlation coefficient (r^2) indicates the proportion of data variance explained by the fitted regression line ($Y = \alpha + \beta X$).

3. The root-mean-square error (*RMSE*) is a measure of the differences between modeled values (X) and observed values (Y). The smaller the *RMSE*, the better the model fit.

4. δ_ρ is the relative error of model-predicted reflectance on horizontal terrain, $\delta_\rho = (\hat{\rho}_0 - \rho_0)/\rho_0$, which directly measures the accuracy of the models. ρ_0 is the observed reflectance on horizontal terrain as estimated by the mean reflectance of the selected flat pixels. $\hat{\rho}_0$ is the topographically corrected reflectance using each correction model.

I used an IKONOS image from 27 September 2009 and its Band 3 (red), which is less affected by atmospheric scattering than Bands 1 and 2 and less affected by soil background than the near-infrared Band 4, was selected for the evaluation. The image was orthorectified and transformed to at-sensor reflectance. The test sites are located in the east side of Lake Tahoe Basin, and comprise 7 relatively uniform conifer stands including 12899 pixels, with a sufficiently large range of terrain relief for examining topographic effects and testing the topographic correction models. Some flat pixels ($\alpha <= 5°$) were selected as control points and the average reflectance (ρ_0 =

0.048) of these pixels was used to normalize the reflectance at each pixel of the test site on the image. Normalized reflectance was used for testing the topographic correction models using the above equations.

2.3.2.5 Radiometric Normalization

After preliminary radiometric calibration and radiometric correction of topographic effects, there remain radiometric distortions caused by other factors, especially the atmospheric effects. Atmosphere absorbs and scatters radiation reflected from the ground before it reaches the satellite sensor, and the variation in atmospheric conditions across years affects multitemporal remote sensing data (Jensen 2005). Further radiometric correction is necessary for change detection using multitemporal images (e.g. IKONOS and Landsat TM) (Song et al. 2001, Du et al. 2002).

I took a relative radiometric normalization approach which requires neither atmospheric properties nor ground spectral measurements and is often more operational to minimize atmospheric effects for change detection purposes (Collins and Woodcock 1996). Canty and Nielsen (2008) proposed an automatic relative radiometric normalization method based on the iteratively re-weighted multivariate alteration detection (IR-MAD) transformation theory. Computer programs for IR-MAD (Nielsen 2007) and for automatic relative radiometric normalization (Canty and Nielsen 2008) in the form of IDL extensions to ENVI were used in this study to normalize multi-temporal images.

For Landsat TM, the 24 September 2010 scene was selected as the reference to which images of all other years were normalized. I initially collected 32 spectrally invariant features, also referred to as *radiometric ground control points* (RGCP), from the field. The pixel values of RGCPs from each band of the reference image and target image were used to calibrate a regression

equation: y (reference image) = a*x (target image) + b. The resulting equation was applied to normalize the target image (x). In this method, the RGCPs were carefully collected throughout the Tahoe Basin including deep water bodies as well as invariant land features such as bare soil, roads, large rooftops, parking lots, sand, and large rock outcrops, to ensure a long enough spectral gradient. However, the limited number of field collected RGCPs were likely subject to change when the time span is long between the target image and the reference image. Therefore, the IR-MAD tools were used to statistically identify no-change pixels and to normalize a whole stack of images spanning 24 years. Dark-object subtraction (Chavez 1988) was applied to the 24 September 2010 reference image to correct for first-order atmospheric scattering effects. An experiment confirmed that regardless of whether dark-object subtraction was applied to the target image, IR-MAD identified the same number of no-change pixels and produced exactly the same normalized image. A mask band was used to mask out the large water body of Lake Tahoe which can constitute a false no-change background due to waves and solar glare (Canty 2011).

IKONOS imagery is very sensitive to collection angles, sun angles, and atmospheric effects, and thus the radiometric variation between different images can be large and the noise to signal ratio can be high. The preliminary radiometric calibration already accounted for solar illumination variations. The BRDF effects due to the difference in view angles (2.44° in zenith and 17.31° in azimuth between 2005-09-25 and 2009-09-27 images) and atmospheric effects were further normalized based on the same relative normalization theory as above by identifying spectrally invariant pixels, using the iMAD tool developed by Canty and Nielsen (2007). Topographic correction was done in advance of iMAD normalization because the spectrally invariant pixels found by iMAD may be on different slopes and thus the varied topographic effects should be corrected in order to identify true spectrally invariant pixels.

2.3.3 Vegetation Indices

There are many vegetation indices (VIs) used to estimate the health status of vegetation with remotely sensed data. Vegetation indices are based on the principle that significant differences exist in the reflectance of healthy vegetation, senesced vegetation, and bare soil as a function of wavelength. Information contained in a single spectral band/wavelength is usually hard to interpret and insufficient to characterize vegetation status. Thus a variety of vegetation indices have been developed by combining two or more spectral bands in certain mathematical formulations, in order to estimate relative abundance and activity of green vegetation, which can be described by such parameters as leaf area index (LAI), percentage green cover, green biomass, chlorophyll content, and photosynthetic activity or absorbed photosynthetically active radiation (APAR) (Jensen 2005). The vegetation index data can be further used in various classification and change detection processes.

Most vegetation indices can be divided into two general categories: ratios and linear combinations (Jackson and Huete 1991). The former uses the ratio of any two spectral bands or the ratio of sums, differences or products of any number of bands, such as Normalized Difference Vegetation Index (NDVI); while the latter uses linear combinations of two or more spectral bands, such as Tasseled Cap (Kauth-Thomas) Transformation. They are distinct in that, in spectral feature space, the vegetation isolines (i.e. a constant amount of vegetation with varying soil backgrounds) of ratio indices converge at the origin, while those of linear combination indices remain parallel to the soil line (i.e. the axis of bare soil spectral variation as a function of soil type and/or soil condition).

Many of the vegetation indices make use of the significant difference between red and near-infrared reflectance values associated with green vegetation. Reflectance values of the near-infrared band generally increase with increasing vegetation cover, whereas those of the red band generally behave in the opposite way (Huete and Jackson 1985). Thus, the combination of reflectance values from red and infrared bands of multispectral imagery can be used to characterize vegetation quantity and vigor. NDVI derives from this principle and is the most commonly used vegetation index for detecting living vegetation canopies (Rouse et al. 1974). It produces index values ranging from −1 to +1, where higher values indicate more, or healthier, vegetation in a pixel and vice versa. The formula for NDVI is:

$$NDVI = \frac{NIR-R}{NIR+R} \tag{26}$$

where, for both Landsat TM and IKONOS imagery, NIR refers to near-infrared band 4 and R refers to red band 3.

The Tasseled Cap (Kauth-Thomas) transformation is an example of linear combination indices which produces four orthogonal indices: brightness, greenness, yellowness and non-such using four Landsat MSS bands (Kauth and Thomas, 1976). Later, Crist and Cicone (1984b) applied the tasseled cap concept to Landsat TM data and produced three orthogonal indices: brightness, greenness and wetness, using all six reflective bands of Landsat TM. The equations are as follows:

$$\begin{aligned} B &= 0.3037TM1+0.2793TM2+0.4743TM3+0.5585TM4+0.5082TM5+0.1863TM7, \\ G &= -0.2848TM1-0.2435TM2-0.5436TM3+0.7243TM4+0.0840TM5-0.1800TM7, \\ W &= 0.1509TM1+0.1973TM2+0.3279TM3+0.3406TM4-0.7112TM5-0.4572TM7. \end{aligned} \tag{27}$$

Here, the brightness feature is defined by the intersection of the plane of vegetation and the plane of soils. Soil variation is two dimensional in the TM Tasseled Cap space and is not equivalent to the primary direction of soil reflectance variability (soil line). However, TM brightness does respond sensitively to change in soil characteristics, because its formula captures variation in total reflectance. It is less responsive to vegetation change. TM greenness is a vector perpendicular to brightness. It is computed to be maximally responsive to the combined effect of high absorption in the visible bands (due to plant pigments and photosynthetic activity) and high reflectance in the near-infrared (due to internal leaf structure and the resultant scattering of near-infrared radiation), which is similar to the contrasting of near-infrared and red bands in NDVI and is thus able to characterize green vegetation. The wetness feature is defined to correspond to the direction of soil moisture and plant moisture variation and is orthogonal to both brightness and greenness. In the three dimensional space of TM data, brightness and greenness define the plane of vegetation and brightness and wetness define the plane of soil.

Some VIs fail to predict vegetation isoline behavior because of the presence of varied soil signals from canopy gaps and different soil backgrounds under constant canopy cover are likely to produce different VI values (Colwell 1974). Huete et al. (1985) found that the sensitivity of VIs to soil background effects was greatest in canopies with intermediate levels of vegetation cover, where there is enough vegetation to scatter and transmit a significant amount of NIR flux to the soil surface, as well as enough canopy gaps to allow the soil-reflected NIR signal, which strongly resembles vegetation spectral signatures, to reach the sensor. Both NDVI and Tasseled Cap transformations are sensitive to soil background effects.

A series of soil-adjusted indices have been created to reduce soil background effects. The first Soil-Adjusted Vegetation Index (SAVI) was proposed by Huete (1988) using a soil-

adjustment factor L to account for first-order approximation of soil background effects by shifting the NIR-Red spectral space origin to a point where the isolines of intermediate densities of vegetation converge with the soil line:

$$\text{SAVI} = \frac{\rho_{\text{NIR}} - \rho_{\text{R}}}{\rho_{\text{NIR}} + \rho_{\text{R}} + \text{L}}(1 + L), \tag{28}$$

where the optimal value of L deceases with increasing vegetation density. L = 1 for very low vegetation densities, L= 0.5 for intermediate vegetation densities, L= 0.25 for high densities.

Qi et al. (1994) presented a Modified Soil Adjusted Vegetation Index (MSAVI) that replaced the general constant L in the SAVI equation with an empirical or inductive L function that was data related and could self-adjust its L value to an optimum. This modification was proved to be of advantage over SAVI and other indices. It produces higher (vegetation) signal to (soil) noise ratio. A study using IKONOS imagery showed that MSAVI was better able to detect small vegetation patches and overcome soil background effects to a better degree than NDVI. However, MSAVI was more vulnerable to shadow effect than NDVI. It classified shadowed areas more easily as "mixed" containing both vegetation and non-vegetation information (Van Delm and Gulinck 2009). MSAVI is defined as follows:

$$\text{MSAVI} = \frac{\rho_{\text{NIR}} - \rho_{\text{R}}}{\rho_{\text{NIR}} + \rho_{\text{R}} + \text{L}}(1 + L) \tag{29.1}$$

where L = 1-2γNDVI*WDVI, where γ is the primary soil line slope and WDVI is the weighted difference vegetation index (WDVI = NIR-γR). The inductive version of MSAVI is of this form:

$$\text{MSAVI} = \frac{2\rho_{\text{NIR}} + 1 - \sqrt{(2\rho_{\text{NIR}} + 1)^2 - 8(\rho_{\text{NIR}} - \rho_{\text{R}})}}{2} \tag{29.2}$$

which is based on the same principle as the previous empirical version and has almost the same vegetation sensitivity and soil noise reduction ability. It is also easier to apply to Landsat TM and IKONOS images, so the inductive version was used.

To determine whether soil background effects necessitate a soil-resistant vegetation index for my study goals of quantifying road-related tree crown mortality in the Lake Tahoe Basin, SAVI and MSAVI were compared with NDVI and K-T components to see if the soil-adjustment function of the former would provide improvement over the latter. These indices were implemented in models by ArcMap model builder and vegetation index images were generated. Comparison of the performance of these vegetation indices was based on their power of predicting field-measured LAI, using either a linear relationship or exponential relationship.

2.3.4 Predicting LAI from vegetation index

My approach for quantifying tree crown mortality used the difference between LAI of successive time periods (Figures 3 and 4). LAI can be estimated by remote sensing vegetation index (VI) using a linear or non-linear regression model calibrated with field LAI measurements (Section 2.2.1.2). Tree crown mortality based on LAI differencing can be validated by separate tree health survey data (Section 2.2.1.1).

VI data from Landsat or IKONOS were calibrated with LAI data, measured by the LAI-2000 Plant Canopy Analyzer (LI-COR 1992) on a 30×30m plot basis. A total of 94 plots were used for IKONOS data and 120 for Landsat data.

For IKONOS data, the 4-m pixels were resampled into 1 meter and the 30×30m square polygon features representing the field plots were used to calculate zonal statistics on the 1-m VI images with non-tree pixels assigned the VI value of soil. LAI values of the plots were related to

30×30m plot-level mean VI values to derive the regression equation for predicting LAI by VI. For Landsat data, the 30×30m pixels are exactly overlapped by LAI plots. Relating Landsat VI to field LAI was thus straightforward.

VIs reach a saturation level at high values of LAI (Hatfield et al. 1985) (Figure 8). A simple linear relationship is not sufficient for predicting LAI from VIs, although the linear regression results in VIs comparison (Section 3.2) did not reveal this saturation effect because the field data did not include sufficiently high LAI values (>8) to saturate VIs. Many studies have suggested the use of exponential relationships (Hatfield et al. 1985, Baret and Guyot 1991) such as the semi-empirical model by Baret and Guyot (1991). This model is formed by the following equation:

$$VI = VI_{\infty} + (VI_g - VI_{\infty})exp(-K_{VI} * LAI), \text{ or} \quad (30.1)$$

$$LAI = -\frac{1}{K_{VI}} Ln \frac{VI_{\infty} - VI}{VI_{\infty} - VI_g} \quad (30.2)$$

where,

VI_g = vegetation index corresponding to that of the bare soil,

VI_{∞} = asymptotic value of VI when LAI tends towards infinity (practically this limit is always reached for LAI greater than 8.0),

K_{VI} = coefficient which controls the slope of the relationship (equivalent to an extinction coefficient).

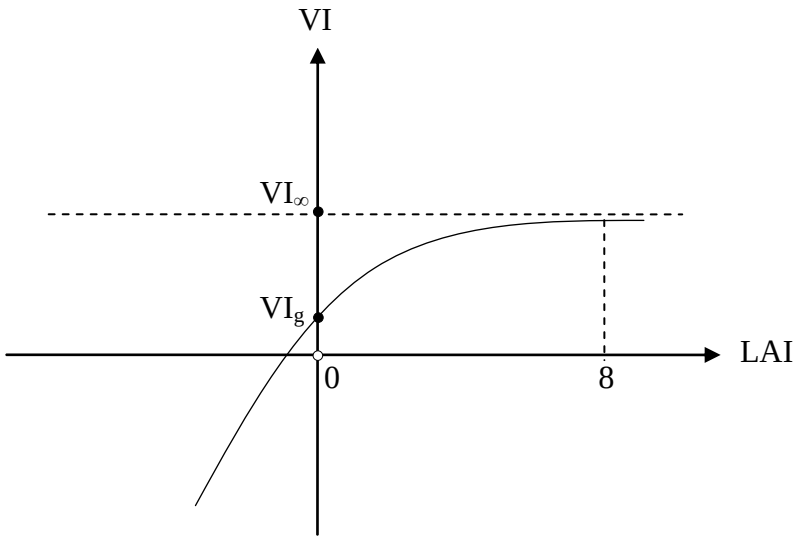

Figure 8. The theoretical non-linear relationship between VI and LAI.

This equation was calibrated with the field LAI data and image VI data. VI_∞ and K_{VI} are affected by leaf inclination angle and irradiance. Baret and Guyot (1991) obtained VI_∞ and K_{VI} for different average leaf inclinations by fitting the above model with a fixed value for VI_g. For conifer species, leaf inclination angle is hard to determine because of the clumping of conifer needles and irregularity in inclination angles. I therefore ignored the variation in leaf inclinations in the LAI plots containing different conifer species and aimed to obtain a set of general parameters (VI_∞ and K_{VI}) for VI-LAI transformation that are applicable to the major conifer species for the whole study area. Image data were used to identify VI_g, while VI_∞ and K_{VI} were empirically calibrated by fitting the non-linear equation (30.1) using field LAI data and image VI values. The calibrated equation (30.1) was transformed to equation (30.2) which was then used to predict LAI by VI.

VI_g was estimated as the mean VI value of non-tree pixels (using the LiDAR mask) within the LAI plots. These pixels were not necessarily "bare" soil, rather, they represented the actual ground surface uncovered by tree crowns or tall shrubs but possibly covered with debris or

small understory vegetation (e.g. grass, sagebrush). Because the field LAI measurements did not include low understory vegetation, a plot having a LAI of 0 contains no tree crowns, but can include some understory vegetation that contributes to the VI value. Therefore, the VI_g value obtained from the non-tree pixels, selected as described above, gives a better estimate of the actual VI value when LAI approaches 0 in equation (30.1).

Baret and Guyot (1991) found that soil-adjusted Vls could reduce the noise in relating VIs and LAI for low leaf area indices (i.e. LAI < 2-3). Our field plots have LAI ranging from 0.44 to 3.7 and 116 out of the total of 120 plots have LAI <=3. Therefore, soil-adjusted VIs including SAVI and MSAVI were also tested against NDVI using the same non-linear algorithm to see if they have stronger predictive power for LAI.

The calibrated VI-LAI relationships using the semi-empirical model (equation 30.2) are generalizable to other years for the same study area as long as there is insignificant year-to-year variation in soil background and other environmental conditions (e.g. solar irradiance, atmospheric conditions and satellite viewing geometry) (Baret and Guyot, 1991). Solar irradiance, satellite viewing geometry and leaf inclination affect the parameters VI_∞ and K_{VI}, but are constant for Landsat images for the same study area. For IKONOS, the issue of slight variation in viewing geometry was addressed in the image preprocessing stage. Soil background variation affects VI and consequently the VI-LAI relationship. But for the same study area, the cross-year variation in soil background can be ignored, and thus the VI-LAI relationship should not be affected from year to year. Therefore, the calibrated VI-LAI relationship from 2010 data can be used to retrieve historical LAI by VI from archival images.

2.3.5 Image Classification of Forest Health

Remote sensing classification maps for different years enabled a post-classification comparison analysis on road-related tree crown mortality that was essentially different from quantitative change detection approaches (e.g. NDVI /LAI Differencing). Image classification was used to test the potential to use multispectral imagery to distinguish pixels with salt-damaged vegetation from those with other types of canopy mortality, as well as those with healthy vegetation, so that the degree of salt damage and direction of change could be detected directly.

IKONOS images were used for classification of tree health status instead of Landsat TM for two reasons: (1) higher spatial resolution (4m), which enables fine-scale analysis of road-related effects; (2) higher radiometric resolution (11-bit), which captures much more subtle differences of radiometric intensity in the pixels or reflectance of the objects, compared to the 8-bit data of Landsat TM. Two IKONOS images from 25 September 2005 and 27 September 2009 were classified. A fuzzy supervised classification using all four multispectral bands (blue, green, red and near-infrared) was conducted in ERDAS IMAGINE with the Maximum Likelihood decision rule. Signature separability evaluation suggested that this four-dimensional feature space created the highest separability among classes. Among the four bands, the near-infrared band played the key role, accounting for 50% of the average separability among the signatures. Eight classes were defined: Salt Damaged Conifers, Healthy Conifers, Broadleaf Trees, Grassland, Water, Road, Construction, and Bare Soil. The selection of the signature pixels for the "Salt Damaged Conifers" class was especially conservative, given the goals of this study. Field survey plots with extensive salt damage in 2009 were targeted for selecting the 2009 signature of this class. Tree GPS coordinates and the orthorectified 1-m resolution panchromatic band were

used as ancillary data to help locate salt damaged tree crowns in the 4-m resolution multispectral image. Extracted individual pixels of such damaged tree crowns on the multispectral image were merged as the final signature for this class. As for the 2005 classification, I used 2006 field survey plots with extensive salt damage as reference to select the signature for the "Salt Damaged Conifers" class on the 2005 multispectral image. The 2006 ground reference data were the earliest available dataset. There was very little change in the salt-damaged plots even between 2006 and 2009. Signatures for the remaining classes other than "Salt Damaged Conifers" were visually selected from the imagery of each year. For the "Healthy Conifers" class, several generally healthy and dense conifer stands were chosen as the signature.

A fuzzy classification was used to assign three best classes to each pixel according to the Maximum Likelihood decision rule. Fuzzy classification takes into account that there are pixels of mixed make-up. For example, a 4-m multispectral pixel of IKONOS may contain 50% tree crown, 30% grass, and 20% bare soil. Fuzzy classification makes it possible to obtain information on what different constituent classes can be found in a mixed pixel. It also reveals that some classes might have certain similarity in the spectral constitution or overlap in the multidimensional spectral feature space. This is particularly the case for the tree classes: Salt Damaged Conifers, Healthy Conifers, and Broadleaf Trees. A signature separability test showed that the Healthy Conifers class had least divergence from Broadleaf Trees, according to Jefferies-Matusita or Transformed Divergence measures.

A fuzzy convolution tool in ERDAS was then operated to create a single classification layer by calculating the total weighted inverse distance of all the classes in a moving window of pixels using the output distance file. The center pixel in the window was assigned to the class with the largest total weighted inverse distance summed over the entire set of fuzzy classification

layers. Classes with a very small distance value remained unchanged while classes with higher distance values might change to a neighboring value if there was a sufficient number of neighboring pixels with that class value and small corresponding distance values. Fuzzy convolution helps create a context-based classification to reduce the "salt and pepper" effect, and makes full use of the information in the multiple classification layers extracted by the fuzzy classification (ERDAS 2010).

2.3.6 Change Detection and Tree Crown Mortality

The quantitative change detection approach used differences in estimated LAI between time periods to quantify tree crown mortality. Since NDVI was found to be the best predictor of LAI for the study area, change in LAI derived from NDVI was used to measure mortality for IKONOS and Landsat TM data (Sections 3.2 and 3.3).

For IKONOS data, tree crown mortality was evaluated as the LAI change from Sep. 25, 2005 to Sep. 27, 2009 at 6-m spatial resolution for the east shore of Lake Tahoe. Mortality was defined as the percentage of LAI decrease exceeding threshold values of 20% or 40%. Binary mortality data (mortality = 1, non-mortality = 0) were thus created, which were used in the logistic regression models to examine road-related effects. The percentage thresholds were used because the 6-m resolution approximates the size of tree crowns and any absolute change value in LAI of a tree is meaningless unless relative to the original LAI of this tree. For example, a tree with sparse foliage (e.g. Jeffrey pine) might have lower absolute decrease in LAI than a tree with dense foliage (e.g. white fir), but the former might have experienced higher degree mortality than the latter. The thresholds also account for noise or unwanted change caused by unmeasured factors. Two levels of thresholds were used and compared in order to see whether the model

using a more conservative threshold can reveal weaker or stronger effects of the predictor variables.

For Landsat TM data, mortality events were defined as $\Delta LAI < -0.2$ or $\Delta LAI < -0.4$ between time periods. Given the 30-m resolution of Landsat TM data, absolute LAI change values were used as the mortality thresholds instead of percentage thresholds because the former can capture single tree mortality among a patch of trees within a 30×30m pixel while the latter is likely to omit single tree mortality in a dense patch where the percentage decrease in the overall LAI can be very low. Therefore, the absolute thresholds are more suitable for detecting mortality at the plot level, compared to the percentage thresholds at the tree level. The 0.2 mortality threshold was selected because the mean LAI of field plots was approximately 2.0 and the mean LAI of all image pixels (forest or non-forest) was approximately 1.0. Much of the mortality from de-icing salt only affected a small proportion of the LAI, from field observation. However, this threshold was likely to be sensitive to small changes in LAI or random variation in the data. Therefore, the 0.4 mortality threshold was used as a comparison to see whether a more conservative threshold is more appropriate for examining road-related effects.

Compared to a quantitative measurement of mortality, post-classification change detection could provide a different approach to modeling road-related tree crown mortality if the classification method could isolate salt-damaged tree crowns directly. Due to the 2-m (half-pixel) difference in the scan and sample origins of the 2005 and 2009 IKONOS images (Sections 2.3.2.1 and 2.3.2.2), and the resulting 2-m true offset between IKONOS classification maps, a pixel-based post-classification change detection analysis was not conducted. Instead, classification results of 2005 and 2009 were summarized separately. The proportion of conifer pixels that were classified as “Salt Damaged Conifers” was used to define mortality. Mortality

percentage was summarized per 10-m distance zone from the roads. Road-related effects on tree mortality were revealed and compared between the years 2005 and 2009.

2.3.7 Validation Using Field Data

Tree crown mortality estimates from change detection were validated with ground reference data. Single year VIs were calibrated using field-measured LAI data (Section 2.2.1.2). The calibrated VI-LAI model (Section 2.3.4) was used to estimate LAI by VI for different years. The change in modeled LAI, used to define mortality (Section 2.3.6), was validated with the tree morphological and pathological survey data (Section 2.2.1.1).

In order to validate the plot-level crown mortality estimates in terms of ΔLAI, the original tree-level survey data, containing *DBH* measurements and tree health ratings for each tree, were transformed to a plot-level measure of "healthy canopy cover" through a *DBH-Canopy Cover* allometric model and "*Weighted Healthy Canopy Cover*" equation. The allometric model estimates crown radius by *DBH* using a linear equation per species (Gill et al. 2000):

$$crrad = b_0 + b_1 DBH \tag{31}$$

where *crrad* is the crown radius and b_0, b_1 are the species-specific parameters. Parameter values for different species were derived from Gill et al. (2000), with parameters for ponderosa pine used to model the ecologically and phylogenetically similar Jeffrey pine. Crown area can be easily calculated from crown radius. After crown area of each tree was calculated, the qualitative measurement of the health status of each tree in the field data was used to weight the raw crown area and the overall healthy canopy cover per plot was derived:

$$Healthy\ Canopy\ Cover = \sum A*100\% + \sum B*80\% + \sum C*30\% \tag{32}$$

Consequently healthy canopy cover change between different years was derived:

$$\Delta \text{ Healthy Canopy Cover} = \Delta \sum A * 100\% + \Delta \sum B * 80\% + \Delta \sum C * 30\% + \sum (A + B) * 5\% \quad (33)$$

where *Healthy Canopy Cover* is the estimation of healthy or effective portion of green area that a tree canopy contains and can be recorded on the remote sensing images. *A, B, C* refer to the field measured health status of each tree and designate in the equation the canopy area of each tree belonging to these health status classes. $\sum A$, $\sum B$, $\sum C$ are the sums of crown area of the trees in a plot belonging to the three classes, respectively. Health status class *A* was assigned to a tree with >89% of the crown in healthy condition, *B* to approximately 60-89% healthy crown, *C* to <50% healthy crown, and *D* to dead trees (Munck et al. 2010). The constant multiplier, 5%, is used in Equation 33 as an estimation of normal tree growth rate over a three-year period for healthy trees.

Equation (33) contains both quantitative (i.e. absolute tree death) and qualitative (i.e. health status change in living trees) aspects of field data. A decrease in $\sum A + \sum B + \sum C$ from 2006 to 2009 reflects the amount of trees that were alive in 2006 but dead in 2009 (marked as *D* or *DEAD*), that is, absolute tree death. The weighting method was used in consideration that *DBH* was not re-measured, given that the minimal growth in *DBH* of the conifers in three years cannot exceed the amount of measurement error. In addition, even if *DBH* had been re-measured very accurately, the weighting method would have had to be used to derive canopy change information because health status can decrease (i.e. healthy canopy cover can decrease) while *DBH* increases or remains constant. Therefore, the change of tree health status including tree death was chosen as the indicator of total healthy canopy cover change. This method made use of both qualitative and quantitative change information and thus was able to validate change

detection results (based on modeled LAI change) using tree health change (described by defoliation and discoloration) rather than using solely physical canopy cover change from measured tree death, on which many other studies (Collins and Woodcock 1996) were based.

The plots surveyed in 2006 and 2009 were examined to exclude outliers due to different surveyors' measurement errors, understory effects or geometric errors of recorded plot locations. For example, 92 of 132 trees in the plot *D-123* were assigned health status *B* in 2006 by a surveyor but status *A* in 2009 by another surveyor, which resulted in a large healthy canopy cover increase using equation (33). However, the LAI of this plot did not show any significant change. The plots *E-1030*, *E-114*, *D-3* and *W-8* were deleted because there were only a few trees in the plots. Most of the ground surface was covered by deciduous understory species such as willow, snowberry, ribes and amelanchier whose canopies change much more dramatically in the fall compared to conifers but they were not surveyed. Overall, thirty plots were used in the validation.

2.4 Statistical Analysis of Road-Related Effects on Tree Crown Mortality

Statistical modeling approaches including generalized linear models (GLMs; e.g. logistic regression) were used to model the effects of multiple underlying causes on tree crown mortality. Mortality probability, the response variable, was derived from remote sensing change detection and calibrated and validated by field data. Explanatory variables included road-related factors (i.e. de-icing salt application, distance from road, roadside topography and traffic) and a non-road-related factor (i.e. precipitation).

Stationary variables such as distance from road and roadside topography were examined in spatial analysis, while temporal variables including salt application, precipitation and traffic were

examined in analysis of changing patterns of roadside tree crown mortality over time. Spatial analyses were performed at both fine-scale (6-m) resolution using the 25 Sep. 2005 and 27 Sep. 2009 IKONOS images and broad-scale (30-m) resolution using the 25 Sep. 1993 and 26 Sep. 1999 Landsat TM images. Temporal analyses also included two levels. The first level compared wet years (1993-1999) with dry years (2003-2009). The second level analyzed the trend of mortality associated with de-icing salt, precipitation and traffic across the years from 1988 to 2010.

2.4.1 Spatial Analysis

2.4.1.1 Spatial Variables

According to the hypotheses of road-related effects (Section 1.4), I constructed spatial proxy variables for aerial deposition effects and soil uptake effects of de-icing salts on tree crown mortality. The field study of Munck et al. (2010) suggested a more significant mechanism of aerial deposition of de-icing salt on tree crowns by moving vehicles than that of root uptake of de-icing salt from soil, but these two mechanisms were not directly compared. Thus, two new variables were created based on roadside topography to model the degree to which either of these two mechanisms was associated with roadside tree crown mortality.

(1) Aerial deposition

The spatial proxy variable for aerial deposition models the combined, synergistic relationships among road distance, slope position (above or below the road) and slope contour with regard to potential de-icing salt effects. The new variable is defined as the profile area contained by the terrain curve, the horizontal line from road and the vertical line, divided by the square of distance, and then divided by distance (Equations 35.1, 35.2, and 35.3). Profile area is

the accumulated trapezoidal area above all the pixels along the nearest Euclidean distance route orthogonal to the road. It is calculated as

$$Profile\ Area = 6 \times [(n \times Road\ Elevation) - \sum_1^n Path\ Pixel\ Elevation]\ , \qquad (35.1)$$

where *n* is the number of path pixels from the destination tree pixel to the corresponding nearest road pixel. The constant "6" refers to the pixel resolution of cubic resampled image. By equation (35.1), downslope areas have positive profile area values, while upslope areas have negative values. Profile area divided by distance square measures the overall path curvature of terrain from road to roadside pixel (Equation 35.2).

$$Path\ Curvature = \frac{Profile\ Area}{Distance^2}. \qquad (35.2)$$

The chance of aerial deposition of de-icing salt to the destination tree pixel is proportional to the overall curvature of the path and inversely proportional to the path distance. Therefore, overall path curvature divided by distance gives the probability of aerial deposition (Equation 35.3).

$$Aerial\ Deposition\ Probability = \frac{Path\ Curvature}{Distance}$$

A pixel along a concave slope from the road will have higher chance of salt deposition from the road than a pixel along a convex slope (with same distance) (Figure 9). But if slope and distance are considered as separate variables at the level of an individual pixel, an opposite and wrong conclusion will be reached because of ignoring other intervening pixels along the path to the roadside.

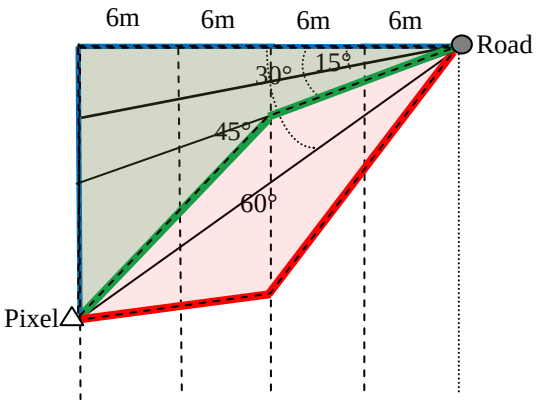

Figure 9. Illustration of the aerial deposition proxy variable.

(2) Soil uptake / flow accumulation

The previous field study by Nowak et al. (2008) observed that uptake of de-icing salt from soil might also be a factor for tree crown mortality, but the degree of its damage compared to direct aerial deposition of salt was uncertain, and not reflected in the data that were collected. In this remote sensing study, another proxy variable was derived to estimate the degree of salt accumulation at a pixel as mediated by water flow regime. The degree of salt accumulation at a pixel is estimated by the flow accumulation from roads. A flow accumulation raster was generated from LiDAR DEM after clipping out the upslope areas above roads and the watersheds unrelated to roads but contributing to the stream lines below roads (Figure 10). Therefore, only flows from roads were considered in the resulting flow accumulation variable. This variable was log transformed to have a normal distribution.

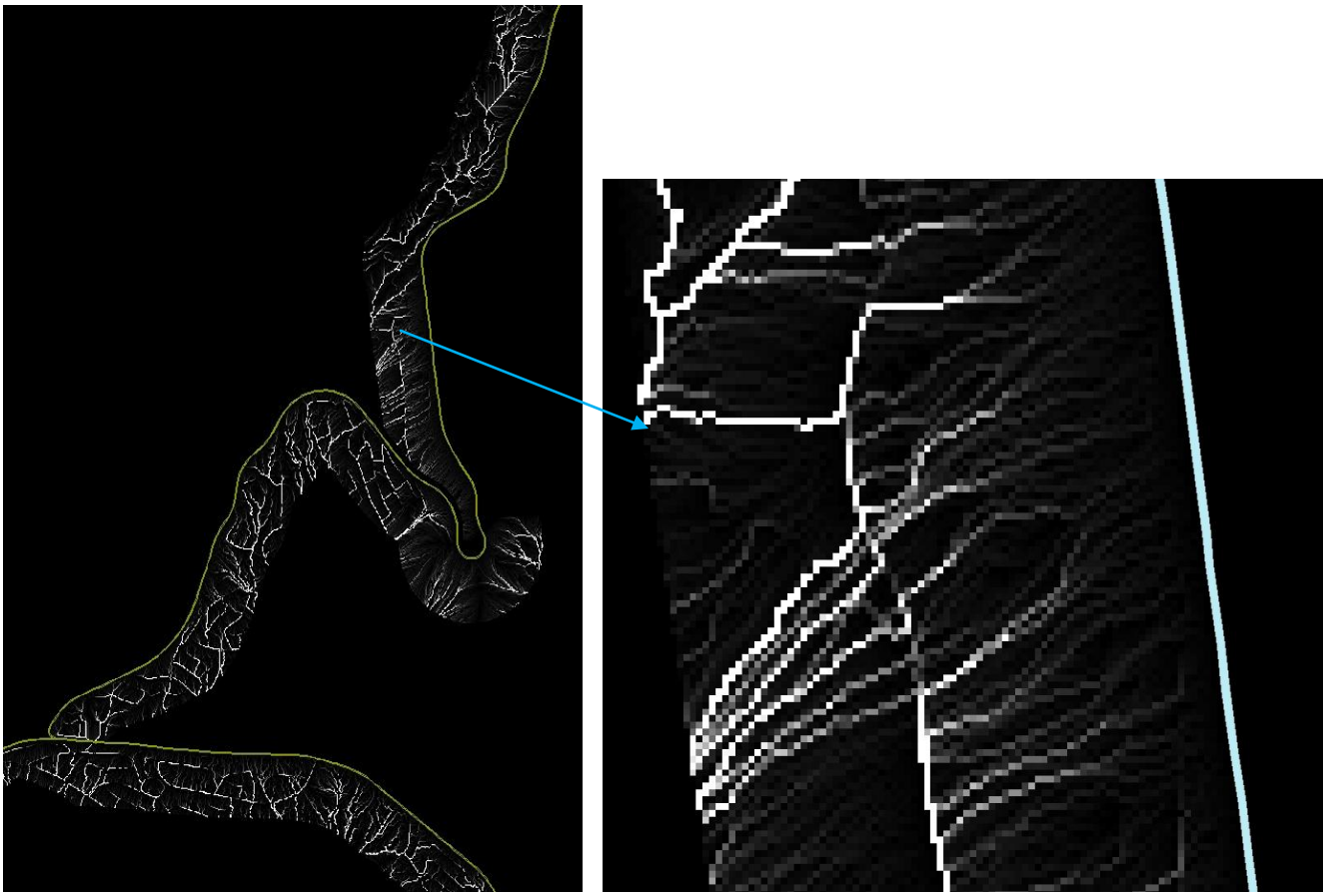

Figure 10. The spatial proxy variable for flow accumulation.

2.4.1.2 Fine-Scale Analysis using IKONOS

To achieve objectives (2) and (3) and test the corresponding hypotheses H1 and H2 (Section 1.4), a fine-scale analysis was conducted using IKONOS imagery by virtue of its 6-m spatial resolution (after resampling), which allows single-tree differentiation for larger crowns and is an appropriate resolution for statistically modeling de-icing salt effects associated with distance from road and roadside topography.

I first examined whether there was a threshold distance from road where road-related effects were no longer significant. Downslope and upslope areas were also compared to examine how distance from road interacted with roadside topography in controlling road-related mortality.

Furthermore, with the aid of the two spatial proxy variables created above, I used logistic regression to quantify how the two mechanisms of de-icing salt effects influenced tree crown mortality using the model:

$$\text{logit}(\pi) = \beta_0 + \beta_1 \, Aerial\ Deposition + \beta_2 \, log(Flow\ Accumulation), \quad (36)$$

where the flow accumulation variable was log transformed to meet logistic regression assumptions. The Akaike information criterion (AIC) and Bayesian information criterion (BIC) scores were used to select the best-fit model.

2.4.1.3 Broad-Scale Analysis using Landsat TM

Broad-scale spatial analysis was performed on 30-m resolution Landsat TM data. A pair of images from 25 Sep. 1993 and 26 Sep. 1999 was selected to explore the effects of two important road-related spatial variables, distance and slope, on the probability of tree crown mortality. Slope was a binary, categorical variable differentiating downslope (downslope = 1) from upslope (downslope = 0). 1993 to 1999 encompasses the wet years when the highest amount of de-icing salt was applied in record (Appendices C and E).

This broad-scale spatial analysis was based on the following logistic regression model:

$$\text{logit}(\pi) = \beta_0 + \beta_1 distance + \beta_2 downslope + \beta_3 distance \times downslope, \quad (37)$$

where

β_0 = log odds for mortality in upslope positions at distance 0 from road;

$\beta_0 + \beta_2$ = log odds for mortality in downslope positions at distance 0 from road;

$\beta_2 = (\beta_0 + \beta_2) - \beta_0$ = log of the odds ratio for mortality in downslope relative to upslope, at distance 0 from road;

$\beta_0 + \beta_1 D$ = log odds for mortality at D meters from road in upslope;

$(\beta_0 + \beta_2) + (\beta_1 + \beta_3) D$ = log odds for mortality at D meters from road in downslope;

$\beta_2 + \beta_3 D = [(\beta_0 + \beta_2) + (\beta_1 + \beta_3) D] - [\beta_0 + \beta_1 D]$ = log of the odds ratio for mortality in downslope versus upslope at distance D from road.

Finally, the rate of change in the log odds ratio with distance is

$$[(\beta_2 + \beta_3 D) - \beta_2] / D = \beta_3.$$

The parameter of the interaction term β_3 shows the effect of distance from road on the relative mortality probability/odds ratio at downslope versus upslope positions.

To test the hypothesis that mortality differs with distance class, the logistic regression was initially run with distance as a categorical variable with 20 levels, with each level having a 30m distance interval. The 0 – 30 m distance zone was the reference level.

Given the 30-m resolution of the samples, the 0–60m and 0–120m zones were tested separately using model (37), when the continuous distance (pixel center to road edge) was used as a numerical explanatory variable. The 0 – 60 m zone was used to test how road distance and roadside topography interact in affecting mortality probability. The square of distance was also tested to assess if the effects of distance were linear or non-linear. The 0–120m zone was used to check if road-related effects extend to beyond 60m because of the suggestive trend found in this zone in the sample data (Table 9, Figure 19).

For Landsat analyses at 30-m resolution, the distance and downslope / upslope variables were used instead of the aerial deposition variable and flow accumulation variable, which are only capable of being used with high-resolution imagery such as IKONOS. Similarly, AIC and BIC scores were used to compare the full model with reduced models.

2.4.2 Temporal Analysis

Archival Landsat TM imagery permits a long-term analysis of forest mortality. I implemented change detection using a stack of images from 1988 to 2010. Raw images were preprocessed and transformed to LAI. A database with LAI change over the 22 years was generated, which informed the dynamic history and trend of Lake Tahoe Basin forest mortality and revegetation. The yearly LAI change data were related to distance from road, upslope /downslope, de-icing salt application, precipitation, and traffic data. I classified those small patches of forest (i.e. 30×30m pixels) that have experienced a mortality event (i.e. negative LAI change exceeding a threshold value -0.2 or -0.4) and used logistic regression to model the probability of a mortality event as a function of the above predictor variables.

Two levels of temporal analyses were performed. First, the pair of anniversary images from 21 Sep. 2003 and 21 Sep. 2009 was compared with the 1993-1999 image pair in the temporal analysis to see the effect of different amounts of salt applied and precipitation on tree mortality probability. The 1993 to 1999 period contrasts with the period from 2003 to 2009 when significantly less de-icing salt was applied due to either the relatively drier climate or NDOT's recent mitigation efforts in salt application (Appendix C). They contrast significantly in precipitation as well (Appendix E). An indicator variable was created for each of the two periods, with the 1993 to 1999 period coded *salt* = 1 (high salt application) and the 2003 to 2009 period coded *salt* = 0 (low salt application). The logistical regression model was formulated as

$$\text{logit}(\pi) = \beta_0 + \beta_1 distance + \beta_2 salt + \beta_3 distance \times salt, \quad (38)$$

in which the interaction term tests the hypothesis that the effects of distance from the road are apparent only in years of high salt application, but are negligible or are not associated with de-icing salt in other years.

At the second level, a stack of images from 1988 to 2010 were used to generate an annual LAI change dataset, excluding years 1989, 1994, and 1997 when suitable images were not available due to cloud or snow cover. Change data from 1988 to 1989, from 1989 to 1990, from 1993 to 1994, from 1994 to 1995, from 1996 to 1997, and from 1997 to 1998 were therefore missing. This dataset allowed long-term analysis of the effects of de-icing salt application, precipitation and traffic on the dynamics of tree crown mortality. First, scatterplots were created to explore the relationships between mortality and salt application, precipitation, and traffic, respectively. Salt application data in the scatterplots were the summary data for each year on all road sections, while in the latter statistical analyses salt data were specific to different road sections (Appendix C), so were the traffic data. Therefore, the scatterplots are shown only for exploratory purpose. Statistical findings were based on the regression analyses using more detailed data.

Using logistic regression, I aimed to test the hypothesis that temporal variation in roadside tree crown mortality is explained by the amount of de-icing salt applied, traffic volume, and climate together. An increasing trend of roadside tree crown mortality was hypothesized to be positively associated with increasing amount of salt applied, after traffic and climate have been accounted for. Interactions between these explanatory variables are also possible. The full logistic model used was

$$\text{logit}(\pi) = \beta_0 + \beta_1 salt + \beta_2 precipitation + \beta_3 traffic + \beta_4 salt \times precipitation + \beta_5 salt \times traffic. \quad (39)$$

Based on the spatial analysis results, only samples from the de-icing salt influenced zone (0–60m) were included in the above model. Traffic data (*MADT*) were only available from 1999 to 2009 (Appendix D).

3 Results

3.1 Evaluation of Topographic Correction Methods

The Sun-Crown-Sensor model (Section 2.3.2.4) made significant improvement over the Sun-Canopy-Sensor model and Sun-Terrain-Sensor model in depicting the correlation between terrain-regulated illumination on tree crowns and observed radiance in red band ($r = 0.58 > 0.56 > 0.54$) (Figures 11 (a), (b), and (c)). The near-infrared band had more scattered reflectance and weaker correlation with terrain-regulated illumination on tree crowns (Figures 11 (d), (e), and (f)). Equation (19) still performed better than other equations in near-infrared band, but the difference in *r* values was relatively small ($r = 0.422 > 0.415 > 0.395$).

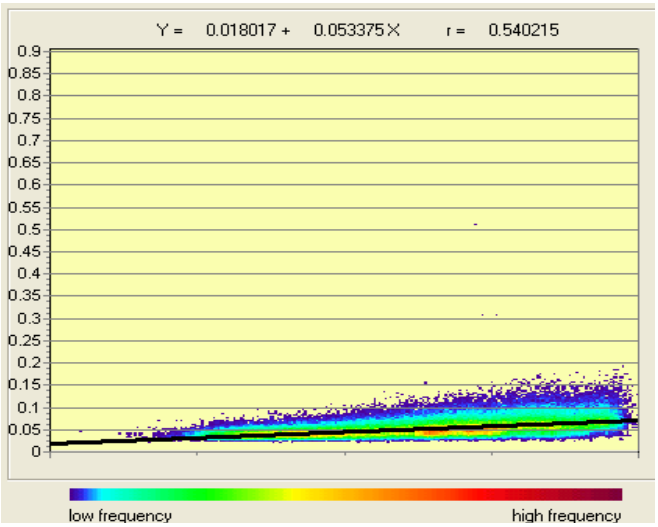

(a)

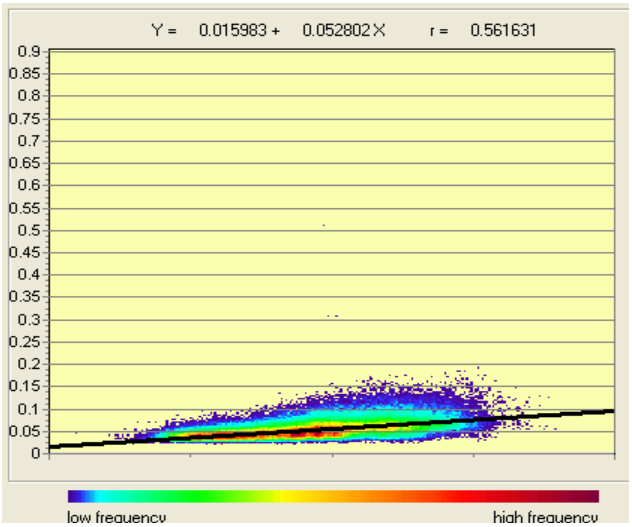

(b)

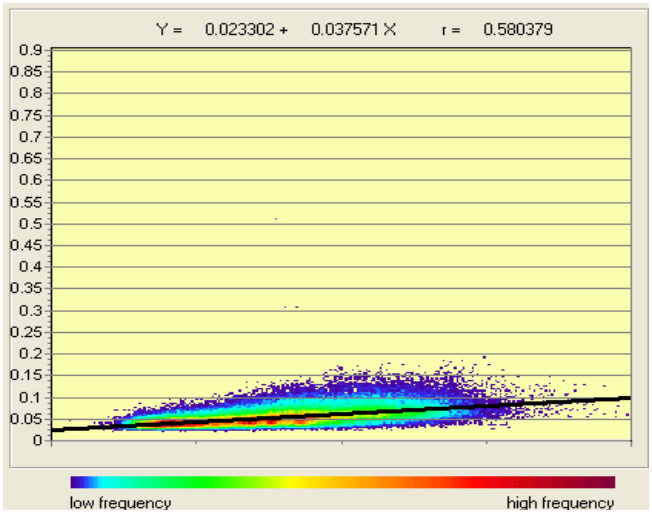

(c)

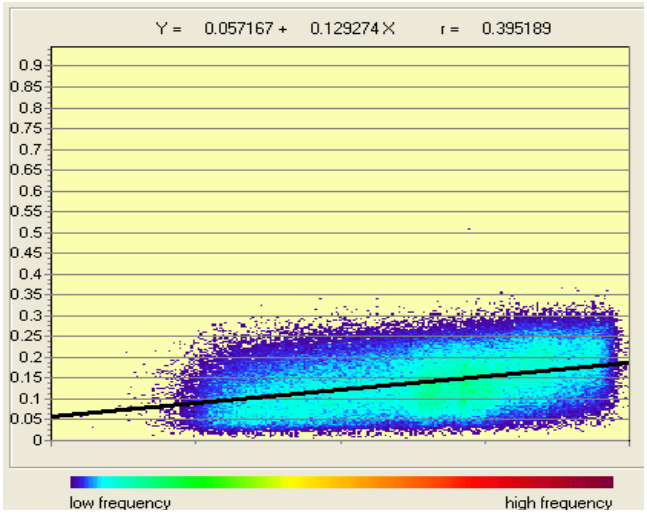

(d)

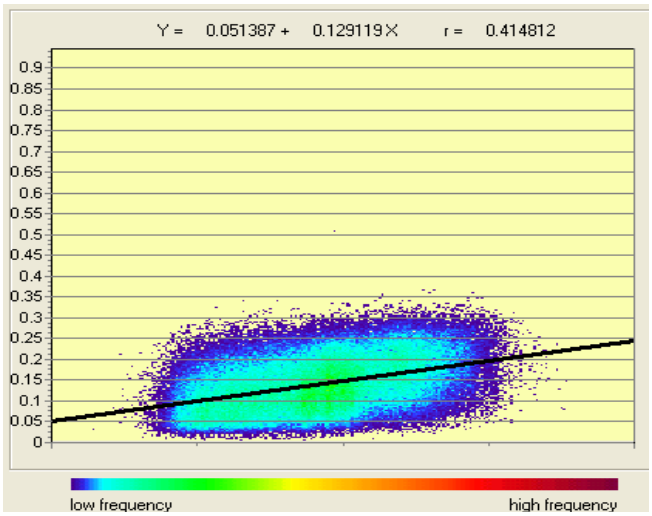

(e)

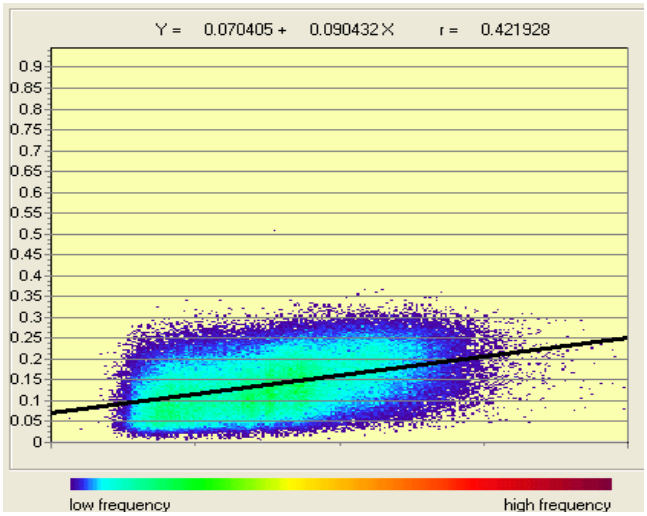

(f)

Figure 11. Comparison of alternative approaches to deriving C parameter, for red band: (a) based on the Sun-Terrain-Sensor model, X axis is the $cos\, i$ (range: 0 ~ 1) image of 2009-09-27; (b) based on the Sun-Canopy-Sensor model, X axis is the $\frac{cos\, i}{cos\, \alpha}$ (range: 0 ~ 1.5) image of 2009-09-27; (c) based on the Sun-Crown-Sensor model, X axis is the $\frac{cos\, i}{cos\, i_s}$ (range: 0 ~ 2) image of 2009-09-27; for near-infrared band: (d) based on the Sun-Terrain-Sensor model; (e) based on the Sun-Canopy-Sensor model; (f) based on the Sun-Crown-Sensor model. A LiDAR tree crown mask was used and a total of 161736 pixels with more than 13/16 (80%) tree crown coverage were used to derive C. This can exclude bare pixels and minimize the influence of soil background on the relationship and highlight the variation of reflectance as a function of sun-crown-sensor geometry. Tall shrubs and deciduous species were also excluded to obtain a better specific C parameter for conifers.

In the model evaluation using test data, the Sun-Crown-Sensor model had the highest R^2 (0.4674) and its +C version outperformed other models by having the highest *EF* (0.3784), lowest *RMSE* (0.287) and lowest δ_ρ (0.0917) in topographically correcting the test image (Table 1, Figure 12). The red band of the 2009-09-27 IKONOS imagery after the SCnS+C topographic correction showed significant decrease in terrain effects, compared to the raw image (Appendix F).

Table 1. Evaluation of the Topographic Correction Models on the Test Site

Model Type		*Equation*		*Data Noise:* 0.3640			
		Y	*X*	r^2	*RMSE*	*EF*	δ_ρ
Sun Terrain Sensor	Cosine Correction	$\frac{\rho}{\rho_0}$	$\frac{1}{\cos\theta z}\cos i$	0.3910	0.3573	0.0364	0.3211
	C-Correction	$\frac{\rho}{\rho_0}$	$\frac{\cos i+C}{\cos\theta z+C}$, $C=\frac{b}{m}$ from $\rho = b + m\cos i$	0.3910	0.3321	0.1678	0.1928
Sun Canopy Sensor	SCS	$\frac{\rho}{\rho_0}$	$\frac{1}{\cos\theta z}\frac{\cos i}{\cos\alpha}$	0.4280	0.3172	0.2408	0.2035
	SCS+C	$\frac{\rho}{\rho_0}$	$\frac{\cos i+C}{\cos\theta z\cos\alpha+C}$, $C=\frac{b}{m}$ from $\rho = b + m\cos i$	0.4284	0.3014	0.3143	0.1251
	Modified SCS+C	$\frac{\rho}{\rho_0}$	$\frac{\cos i+C}{\cos\theta z\cos\alpha+C}$, $C=\frac{b}{m}$ from $\rho = b + m\frac{\cos i}{\cos\alpha}$	0.4284	0.3012	0.3154	0.1285
Sun Crown Sensor	SCnS	$\frac{\rho}{\rho_0}$	$\frac{\cos\theta_s}{\cos\theta_z}\frac{\cos i}{\cos i_s}$	0.4674	0.3288	0.1841	0.1949
	SCnS+C	$\frac{\rho}{\rho_0}$	$\frac{\cos\theta_s\cos i+C}{\cos\theta_z\cos i_s+C}$, $C=\frac{b}{m}$ from $\rho = b + m\frac{\cos i}{\cos i_s}$	0.4557	0.2870	0.3784	0.0917

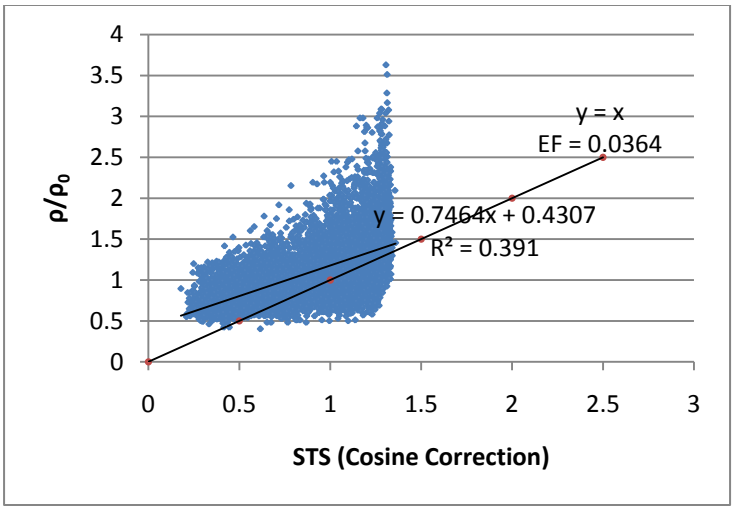
ρ/ρ0
y = x
EF = 0.0364
y = 0.7464x + 0.4307
R² = 0.391
STS (Cosine Correction)

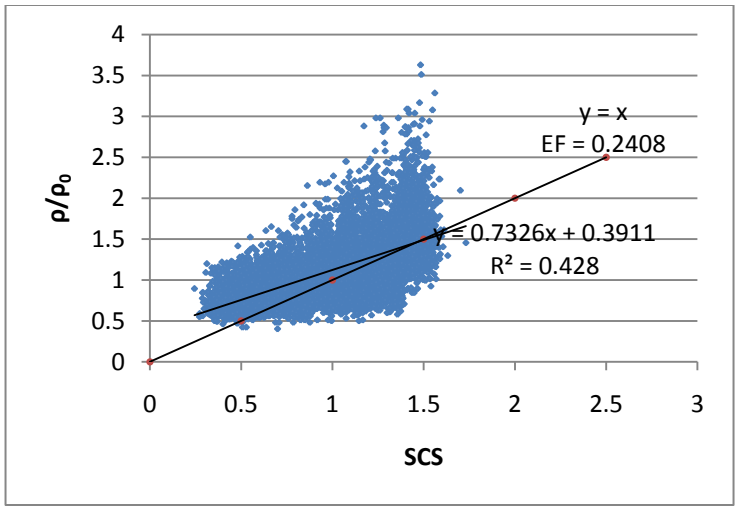
ρ/ρ0
y = x
EF = 0.2408
y = 0.7326x + 0.3911
R² = 0.428
SCS

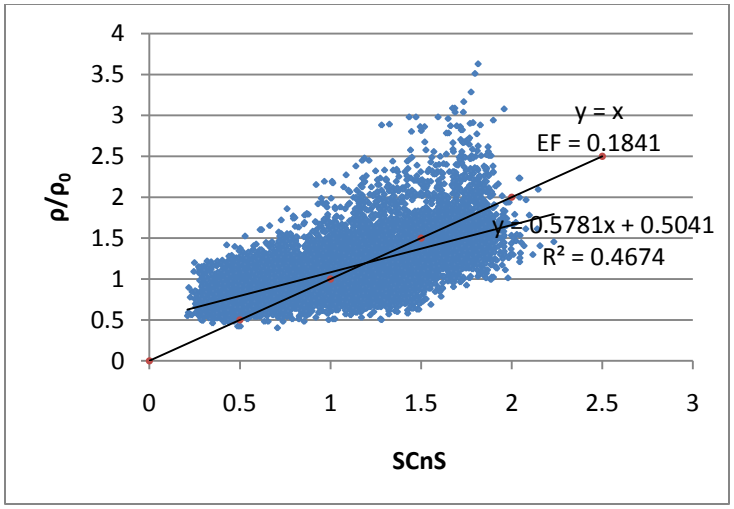
ρ/ρ0
y = x
EF = 0.1841
y = 0.5781x + 0.5041
R² = 0.4674
SCnS

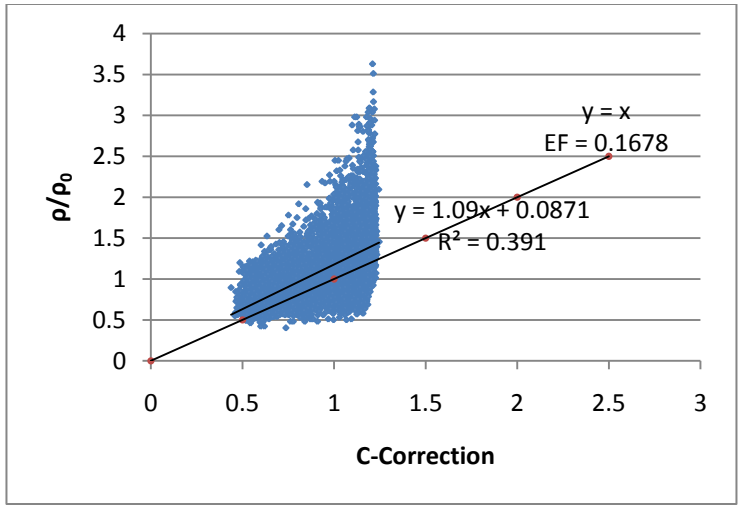
ρ/ρ0
y = x
EF = 0.1678
y = 1.09x + 0.0871
R² = 0.391
C-Correction

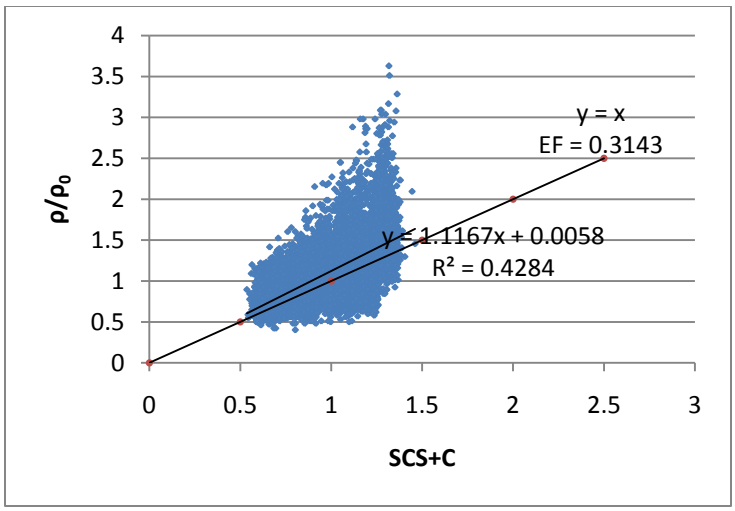
ρ/ρ0
y = x
EF = 0.3143
y = 1.1167x + 0.0058
R² = 0.4284
SCS+C

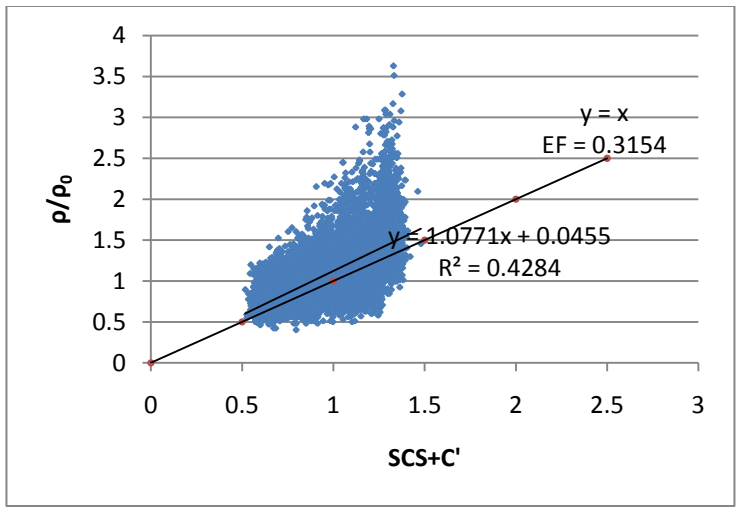
ρ/ρ0
y = x
EF = 0.3154
y = 1.0771x + 0.0455
R² = 0.4284
SCS+C'

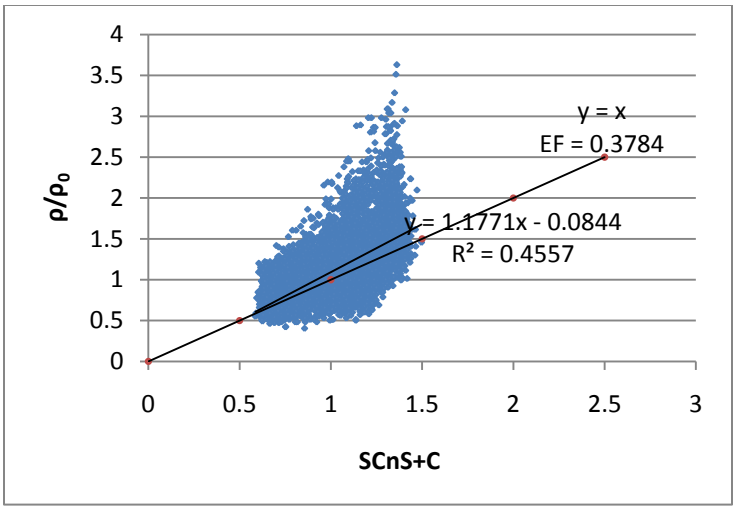

Figure 12. Regression line and line of perfect fit for different topographic correction models using the test site data. ρ/ρ_0 is the observed reflectance on terrain normalized by the flat pixel reflectance (Section 2.3.2.4 (6)).

3.2 Evaluation of Different Vegetation Indices

When NDVI, SAVI (L=0.5 or L=0.25), MSAVI and the Tasseled-Cap indices were used to fit a linear function, all the indices had significant relationships with field measured LAI (Figure 13 and Table 2). NDVI was the best predictor (R^2 = 0.7542), followed by SAVI (L=0.25) and Tasseled Cap indices. The soil-adjusted VIs, esp. SAVI (L=0.5) and MSAVI, did not prove any advantage in adjusting soil background effects or it suggested that soil background effects were not important in this study. Among the three Tasseled Cap indices, Greenness was the only significant predictor (*p-value* = 0.001); Wetness (*p-value* = 0.915) and Brightness (*p-value* = 0.434) were both not useful in estimating LAI.

The comparison of vegetation indices when fitting the exponential relationship (Equation 30.1) using field measured LAI is shown in the next section.

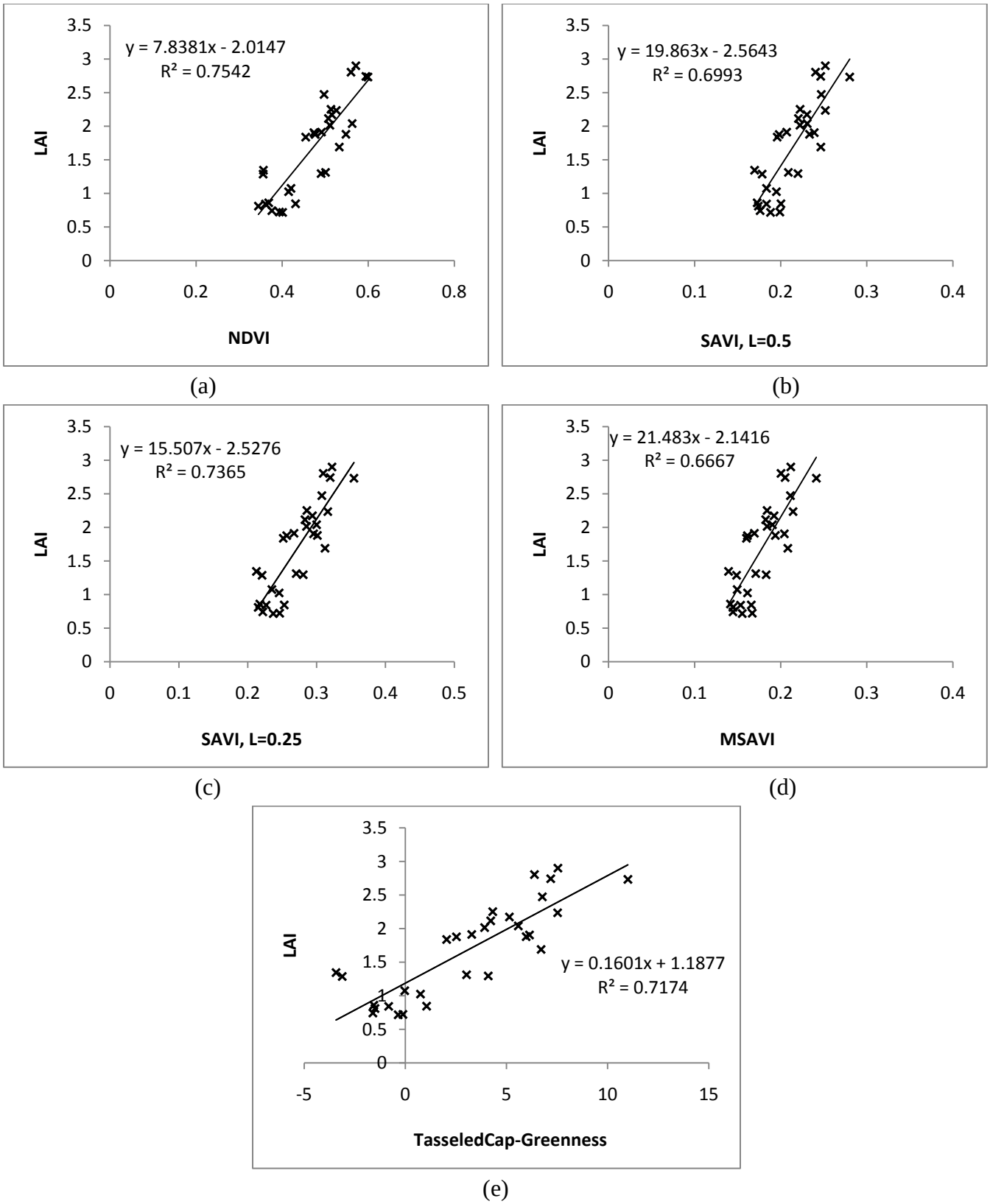

Figure 13. Relationships between LAI and (a) NDVI, (b) (c) SAVI, (d) MSAVI, (e) Tasseled Cap Greenness.

Table 2. Multiple Regression results using LAI as dependent variable and the 3 Tasseled Cap indices as independent variables.

Coefficients	*Value*	*Std. Error*	*t value*	*P-value*
Intercept	2.3530	1.1604	2.0278	0.0529
Brightness	-0.0124	0.0156	-0.7956	0.4335
Greenness	0.1384	0.0384	3.5994	0.0013
Wetness	-0.0030	0.0275	-0.1077	0.9151
Degrees of freedom: 28		Residual standard error: 0.038985		
Multiple R-Squared: 0.7338		Adjusted R-squared: 0.7031		

3.3 Modeled VI-LAI Relationship

When the VI-LAI relationships were calibrated with field measured LAI for IKONOS and Landsat TM data using the non-linear semi-empirical model (Equation 30.1), NDVI yielded the most reasonable values for parameters VI_∞ and K_{VI} when checked with image data (Tables 3 and 4). When the soil-adjusted vegetation indices were used in the model, either negative K_{VI} values or VI_∞ values lower than the VI_g (soil VI) were obtained (Table 5). Therefore, only NDVI was used in the model to estimate LAI in this study.

Table 3. Nonlinear regression for NDVI using IKONOS data. NDVIg was identified and fixed.

Parameters	Value	Std. Error	t-value	p-value
$NDVI_g$	0.206			
$NDVI_\infty$	0.7290	0.1431	5.093	< 0.0001
K_{VI}	0.2113	0.0733	2.882	0.005
Degrees of freedom: 92		*Residual standard error*: 0.0359		

Table 4. Nonlinear regression for NDVI using Landsat data. NDVIg was identified and fixed.

Parameters	Value	Std. Error	t-value	p-value
$NDVI_g$	0.257			
$NDVI_\infty$	0.7609	0.1374	5.536	< 0.0001
K_{VI}	0.3454	0.1359	2.542	0.017
Degrees of freedom: 28		*Residual standard error*: 0.0390		

Table 5. Nonlinear regression for other VIs using Landsat data. VIg was identified and fixed.

Parameters	Value	Std. Error	t-value	p-value
$MSAVI_q$	0.156			
$MSAVI_\infty$	0.1510	0.0040	37.930	< 0.0001
K_{VI}	-0.9271	0.2872	-3.227	0.004
Degrees of freedom: 28		*Residual standard error*:	0.0165	
SAVI (L=0.5)	0.175			
$SAVI_\infty$	0.1470	0.0190	7.723	< 0.0001
K_{VI}	-0.4898	0.1971	-2.485	0.02
Degrees of freedom: 28		*Residual standard error*:	0.0165	
SAVI (L=0.25)	0.199			
$SAVI_\infty$	-0.0970	0.4102	-0.237	> 0.5
K_{VI}	-0.1280	0.1543	-0.829	0.4
Degrees of freedom: 28		*Residual standard error*:	0.0201	

From Tables 3 and 4, the following equation was used to transform IKONOS NDVI to LAI:

$$LAI = -\frac{1}{0.211} Ln \frac{0.729 - NDVI}{0.729 - 0.206},$$

and equation

$$LAI = -\frac{1}{0.345} Ln \frac{0.761 - NDVI}{0.761 - 0.257}$$

was used to transform Landsat NDVI to LAI.

3.4 Quantitative Change Detection Results

A dataset of yearly change detection results as measured by quantitative LAI change was generated using Landsat TM images from 1990 to 2010 for long-term temporal analysis. LAI change images from 1993 to 1999 encompassing wet years with high salt application and from 2003 to 2009 encompassing dry years with low salt application were also created using Landsat TM anniversary images for broad-scale spatial analysis and wet-dry year comparison (Figure 14).

A 4-year change in LAI from 2005 to 2009 was generated using a pair of IKONOS images for fine-scale spatial analysis (Figure 15).

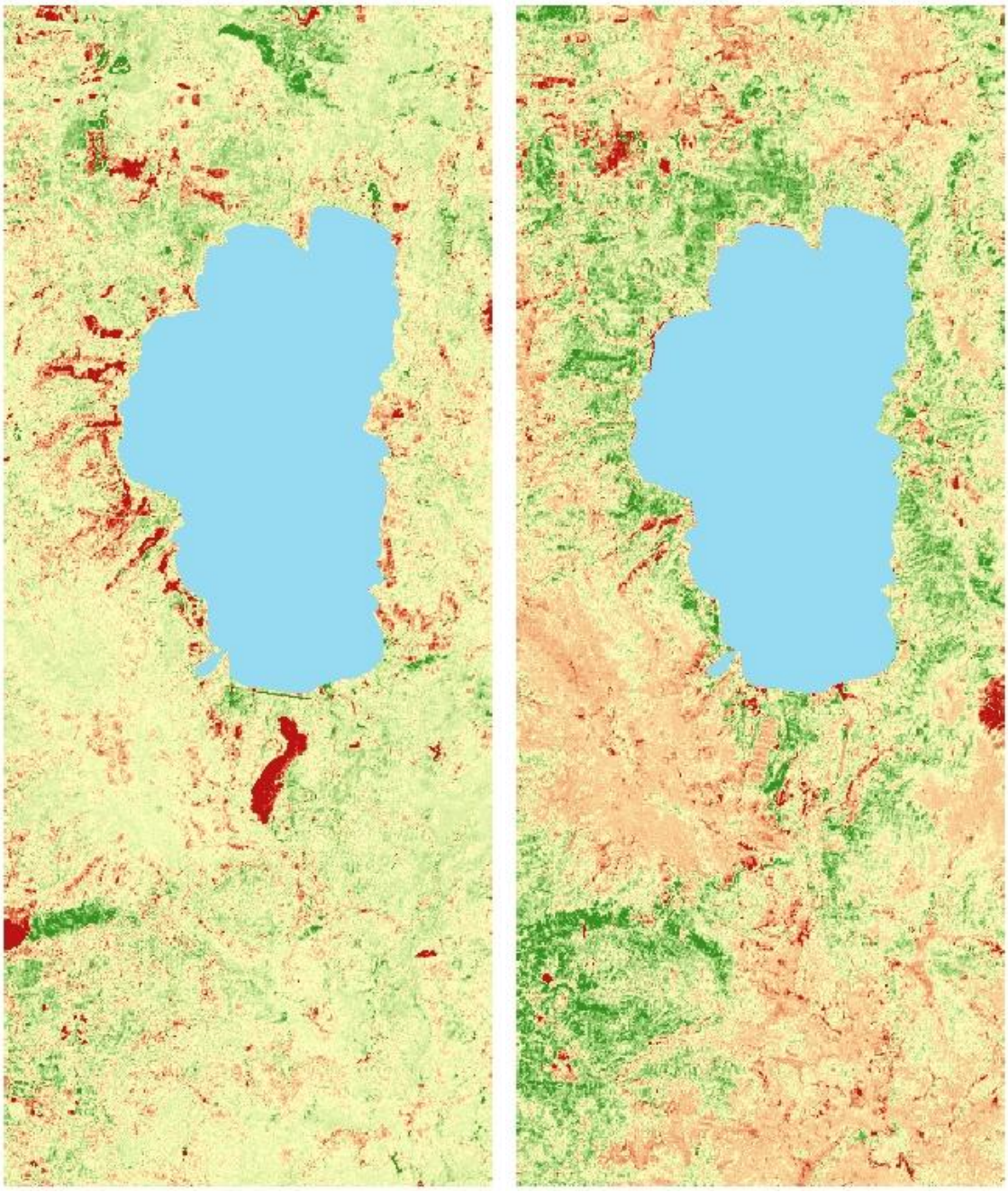

(a) (b)

Figure 14. LAI change: (a) from 25 Sep. 1993 to 26 Sep. 1999 (wet years with high salt application), (b) from 21 Sep. 2003 to 21 Sep. 2009 (dry years with low salt application) for the whole Lake Tahoe Basin using Landsat TM images. Red represents decrease in LAI and green represents increase in LAI.

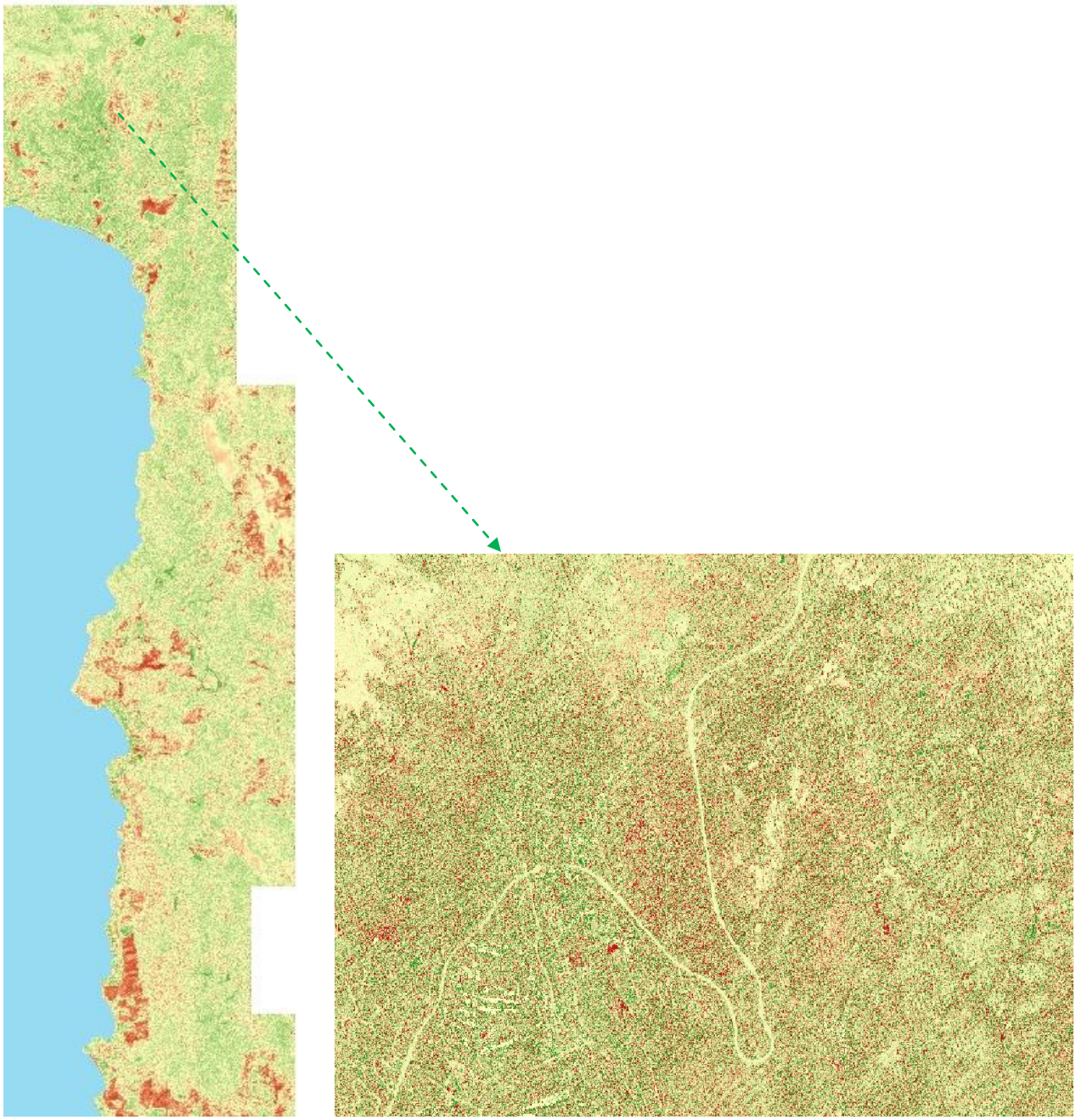

(a) (b)

Figure 15. LAI change from 25 Sep. 2005 to 27 Sep. 2009: (a) for the Nevada portion of the Lake Tahoe Basin using IKONOS images, (b) for the area around Mt. Rose highway near Incline Village. Red represents decrease in LAI and green represents increase in LAI.

3.5 Classification Results

Classification maps for 2005 and 2009 show that trees classified as salt-damaged were widely dispersed throughout the Basin and their quantity was much lower than healthy trees (Figure 16). From 2005 to 2009, there was a decrease in the proportion of damaged trees and a corresponding increase in the proportion of healthy trees (Figures 16a and 16b). However, there was a greater proportion of mortality near roads in 2009 than in 2005, especially within the 0-30m zone (Figure 16c).

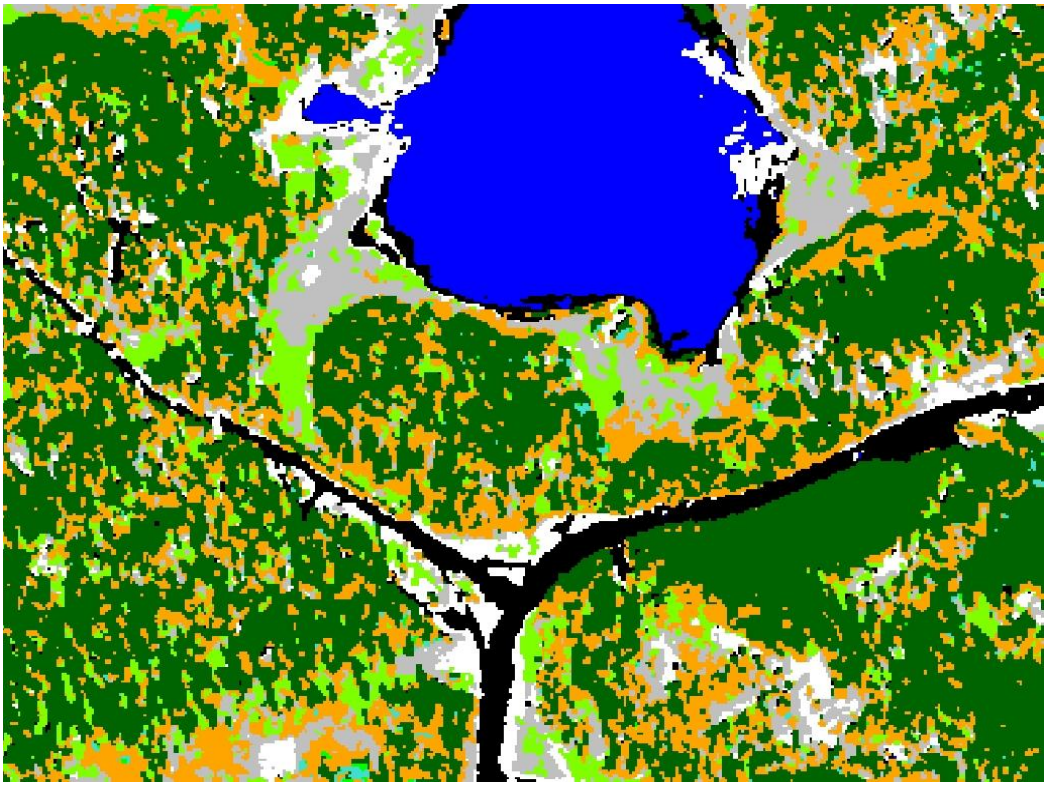

(a) Sep. 25, 2005 Classification (Spooner Lake)

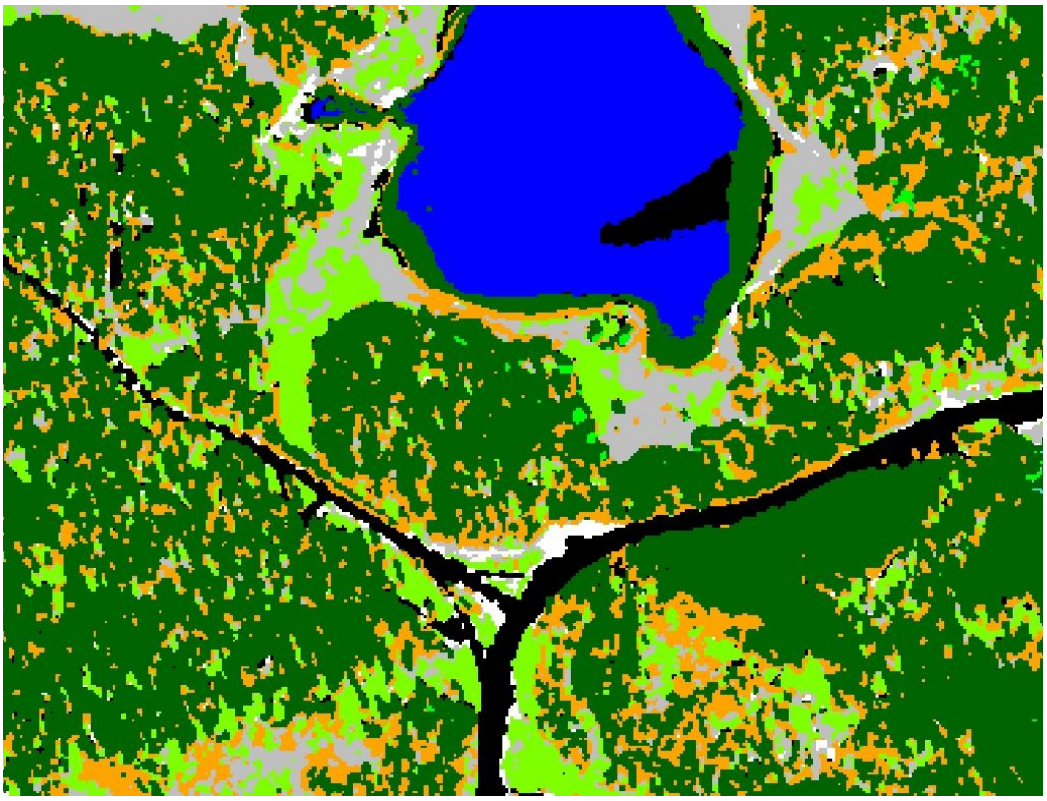

(b) Sep. 27, 2009 Classification (Spooner Lake)

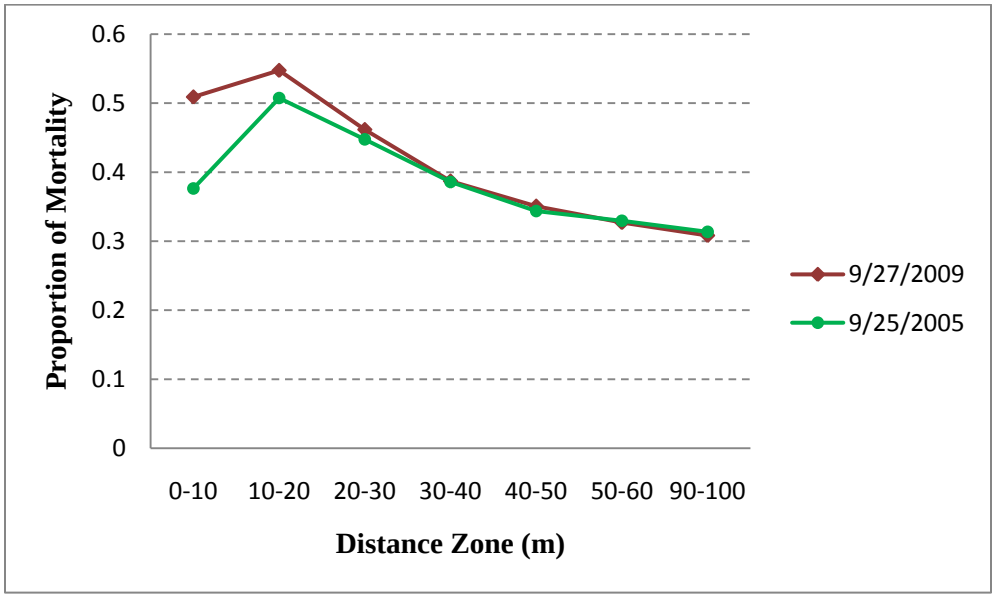

(c) Proportion of mortality per distance zone (whole study area)

Figure 16. Multispectral fuzzy classification results: (a) Sep. 25, 2005, (b) Sep. 27, 2009, and (c) post-classification comparison on the proportion of mortality per distance zone from the road. The colors on the classification map are interpreted as follows: orange = trees with damage; dark green = healthy trees; light green = grassland or shrubland; gray = bare soil; blue = water; and black = road.

3.6 Validation of Remote Sensing Estimated Mortality

LAI change derived from remote sensing was reasonably well correlated with estimates of healthy canopy cover change using field surveys (Figure 17). From 2006 to 2009, most of the field plots were detected by remote sensing to have decreased LAI, but the modeled healthy canopy cover from field surveys (Section 2.3.7) showed many plots had positive changes. Nevertheless, these relationships suggested that remote sensing estimated LAI change in the validation sites was consistent with the canopy health pattern observed in the field.

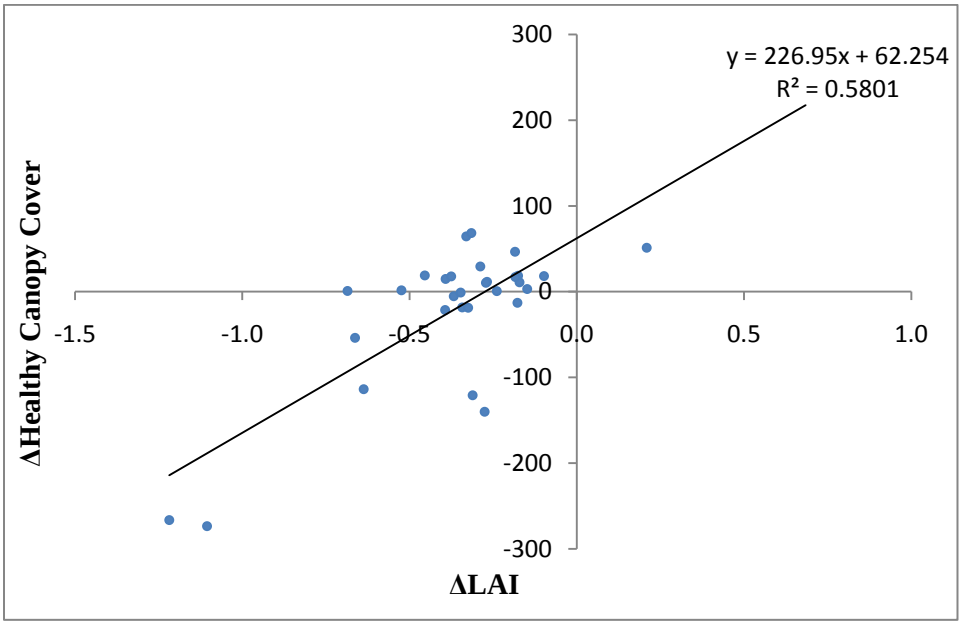

Figure 17. Relationship between observed ΔHealthy Canopy Cover and ΔLAI derived from 2006 and 2009 Landsat TM images.

3.7 Spatial Patterns of Tree Crown Mortality

3.7.1 Fine Scale

From the IKONOS sample data, there was a decreasing trend of mortality probability with increasing distance from road especially within the 0-100m vicinity (Figure 18). The trend leveled off after 150m. For downslope areas, there was a shorter distance zone of 0-30m where

the decrease of mortality was most strikingly evident. Upslope areas generally had higher mortality probability than downslope areas.

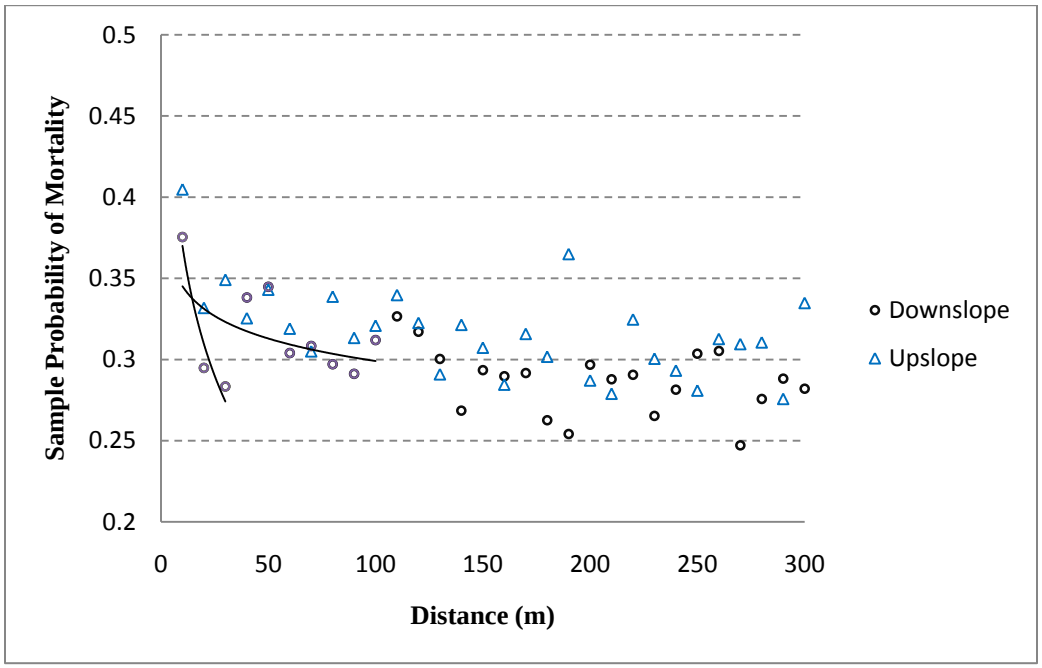

(a)

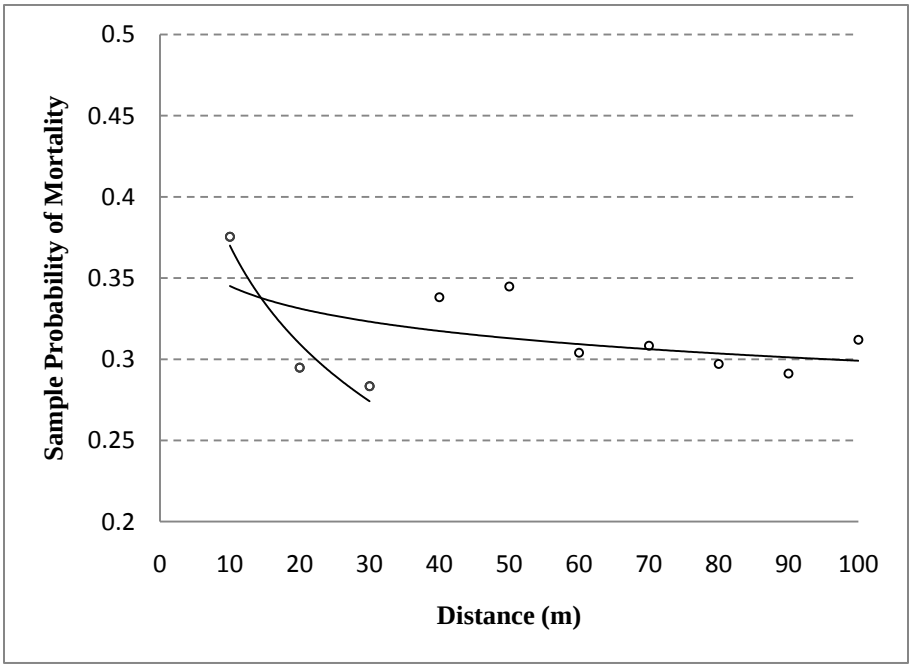

(b)

Figure 18. Scatterplots of sample probability of mortality (threshold=-40%) versus distance for data grouped by intervals of distance using the 2005 to 2009 IKONOS change data. (a) shows

data from the 0–300m zone from the road; (b) shows the trends in the 0–30m and 0–100m downslope regions.

The results of logistic regression of the probability of mortality as a function of distance and up or down slope position were used for explanatory purpose (Table 6). Only samples from 0–100m were included as suggested by Figure 18 to explore road-related effects. The interaction term *distance* × *downslope* was not retained in the final model (*p-value* = 0.76 and 0.44 for the -20% and -40% mortality thresholds, respectively). The mortality probability was negatively associated with both distance from road and downslope positions (Table 6). Because a higher probability of mortality generally existed in upslope positions after accounting for distance, which cannot be explained by road-related effects, only samples from downslope were used in later analyses to examine road-related effects.

Table 6. Logistic regression model to assess the effects of distance and slope (downslope=1, upslope=0) on tree mortality within 0–100m zone, using 2005–2009 IKONOS data.

Mortality Threshold	Variable	Coefficient	Std. error	*z*-statistic	*p*-value
<-20% ΔLAI	*Intercept*	-0.211	0.042	-5.063	0.000
	distance	-0.0006	0.0006	-0.923	0.358
	downslope	-0.0840	0.0338	-2.486	0.013
	Deviance = 19570.24		DF = 14326		
<-40% ΔLAI	*Intercept*	-0.634	0.044	-14.413	0.000
	distance	-0.0013	0.0007	-2.017	0.043
	downslope	-0.0933	0.0358	-2.602	0.009
	Deviance = 17961.56		DF = 14326		

When the two proxy variables for de-icing salt effects (i.e. aerial deposition and flow accumulation) were used in the model, a clear effect of increasing mortality probability associated with increasing aerial deposition and flow accumulation of de-icing salt was revealed

for downslope areas (Table 7). Interpretation of aerial deposition effects can be partitioned into the relative influences of slope steepness, distance from road and path curvature, the three components of the aerial deposition proxy variable (Figure 9). For example, a tree on a 60° slope was 1.57 times (95% CI: 1.14 to 2.16) more likely to be damaged relative to a tree on a 30° slope, at 12m from the road. On a 45° slope, a tree at 12m distance from the road was 1.22 times (95% CI: 1.06 to 1.40) more likely to be damaged relative to a tree that was 24m from the road. At 24m from the road, a tree after a concave slope was 2.47 times (95% CI: 1.31 to 4.67) more likely to have mortality than that after a convex slope.

Flow accumulation effects were statistically significant but weak. The odds ratio of mortality was 1.05 (95% CI: 1.01 to 1.10) with every 10 times of pixels' flow contribution, 1.11 (95% CI: 1.02 to 1.21) with every 100 times of pixels' flow contribution, and 1.17 (95% CI: 1.02 to 1.33) with every 1000 times of pixels' flow contribution.

Table 7. Logistic regression model to assess de-icing salt effects via two mechanisms on tree mortality within 0–100m downslope zone using 2005-2009 data. Mortality was defined by two thresholds, 20% and 40% decrease in LAI.

Mortality Threshold	Variable	Coefficient	Std. error	*z*-statistic	*p*-value
<-20% ΔLAI	*Intercept*	-0.504	0.067	-7.555	0.000
	Aerial deposition	0.0094	0.0034	2.789	0.005
	Flow accumulation(log)	0.0223	0.0097	2.293	0.011
	Deviance = 9910.096		DF = 7293		
<-40% ΔLAI	*Intercept*	-0.956	0.072	-13.327	0.000
	Aerial deposition	0.0112	0.0035	3.225	0.001
	Flow accumulation(log)	0.0177	0.0104	1.700	0.089
	Deviance = 9027.807		DF = 7293		

To assess whether the 0–30m downslope zone near road is most sensitive to de-icing salt effects, as suggested in Figure 18, the model was refit with samples from this zone. Aerial deposition effects became more evident (mortality threshold <-40%), but the effect of flow accumulation was no longer evident (Table 8). The odds ratio of mortality was 1.99 (95% CI: 1.32 to 3.01) in the 0–30m zone with an average increase by 50 unit in aerial deposition, which is equivalent to a change from on a 30° slope to on a 60° slope at 12m from the road. This was slightly higher than the 1.75 (95% CI: 1.25 to 2.46) odds ratio with the same amount of increase in aerial deposition in the 0–100m zone.

Table 8. Logistic regression model to assess de-icing salt effects via two mechanisms on tree mortality within 0–30m zone using 2005–2009 data. Mortality was defined by two thresholds, 20% and 40% decrease in LAI.

Mortality Threshold	Variable	Coefficient	Std. error	*z*-statistic	*p*-value
<-20% ΔLAI	*Intercept*	-0.471	0.115	-4.112	0.000
	Aerial deposition	0.0099	0.0040	2.463	0.014
	Flow accumulation(log)	0.0059	0.0187	0.315	0.749
	Deviance = 2651.384	DF = 1956			
<-40% ΔLAI	*Intercept*	-0.911	0.123	-7.415	0.000
	Aerial deposition	0.0141	0.0042	3.321	0.001
	Flow accumulation(log)	-0.0130	0.0201	-0.647	0.516
	Deviance = 2384.293	DF = 1956	AIC = 2390.29	BIC = 2407.03	
<-40% ΔLAI	*Intercept*	-0.978	0.065	-15.076	0.000
	Aerial deposition	0.0138	0.0042	3.279	0.001
	Deviance = 2384.709	DF = 1957	AIC = 2388.71	BIC = 2399.87	

3.7.2 Broad Scale

A clear trend of decreasing mortality probability with increasing distance from road was observed within 120m of the road, and especially within 60m from the road (Figure 19). There was a slight increase in mortality probability after 60m.

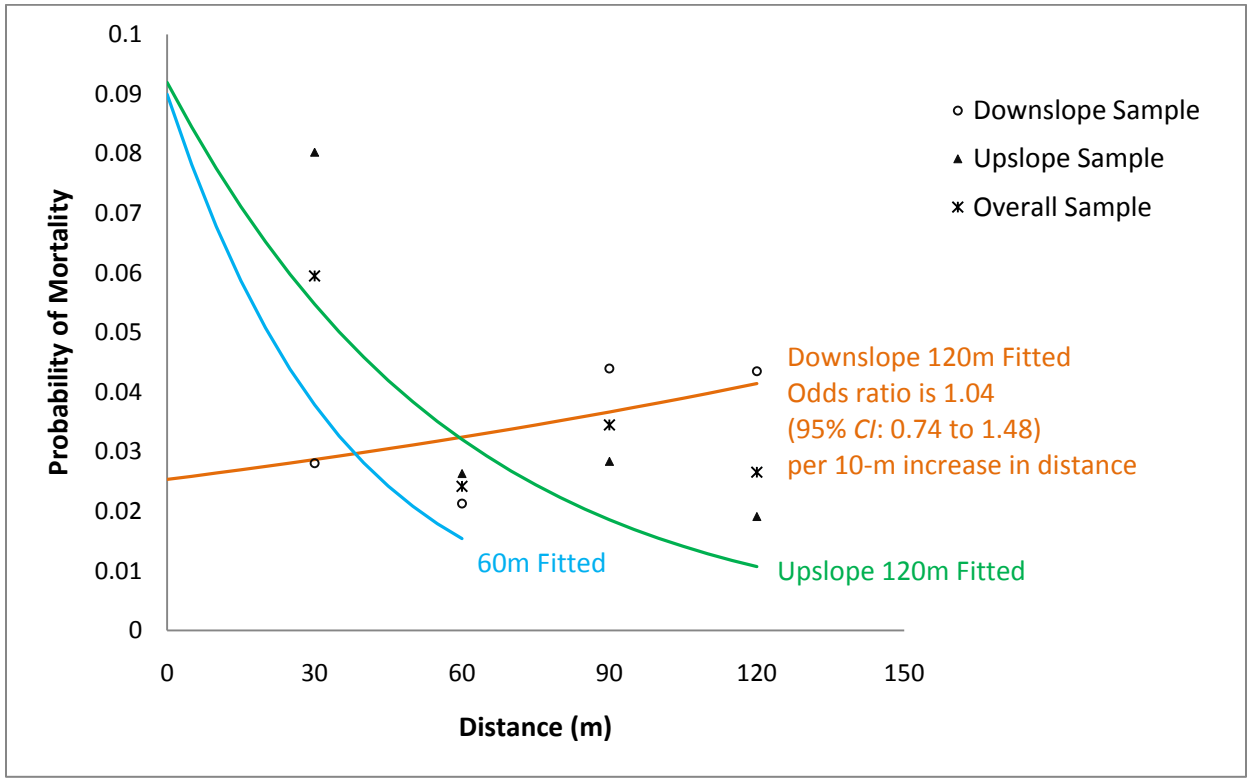

Figure 19. Fits of logistic regression models for probability of mortality at different distance zones and scatterplots of sample mortality probability using 1993–1999 data. Mortality threshold = -0.4 (ΔLAI).

When distance was used as a categorical variable, the only distance zone that had significantly (*p-value* ≤ 0.05) different mortality probability relative to the 0–30m zone was 30–60m (Table 9). The odds of mortality for the 0–30m zone where the trees are more likely to have de-icing salt contact was estimated to be 2.6 times the odds of mortality for the more distant 30–60m zone (95% CI: 1.1 times to 6.2 times). There was also suggestive but inconclusive evidence of decreasing mortality probability in the 60–90m and 90–120m zones. Zones beyond 120m

were not significantly different from the roadside zone (0–30m), and were thus excluded from following analyses.

Table 9. Logistic regression model to assess the effects of different distance classes on tree mortality (threshold=-0.4) rate using 1993–1999 data.

Variable	Coefficient	Std. error	*z*-statistic	*p*-value
Intercept	-3.054	0.272	-11.233	0.000
DIST60	-0.959	0.441	-2.177	0.029
DIST90	-0.570	0.443	-1.287	0.197
DIST120	-0.782	0.488	-1.605	0.107
DIST150	0.373	0.349	1.068	0.285
DIST180	0.341	0.363	0.941	0.347
DIST210	0.072	0.387	0.186	0.063
DIST240	0.306	0.357	0.855	0.390
DIST270	-0.244	0.415	-0.588	0.555
DIST300	0.103	0.407	0.254	0.803
DIST330	-0.066	0.396	-0.167	0.865
DIST360	-0.170	0.416	-0.408	0.682
DIST390	-0.258	0.447	-0.577	0.562
DIST420	-0.786	0.522	-1.507	0.131
DIST450	0.051	0.408	0.125	0.896
DIST480	-0.029	0.419	-0.068	0.944
DIST510	0.182	0.399	0.456	0.646
DIST540	-0.918	0.568	-1.618	0.105
DIST570	-0.183	0.432	-0.424	0.674
DIST600	-0.639	0.525	-1.218	0.222
Downslope	0.630	0.158	3.989	0.000
Deviance = 1677.719		Degrees of freedom = 4579		

When distance was used as a continuous variable and only samples from 0–60m zone were included, the mortality threshold -0.4 was more suitable than -0.2 in revealing road-related effects (Tables 10a and 10b). The hypothesized interaction term between *distance* and *downslope* was not retained in the final model (*p-value* = 0.68). Mortality in downslope areas versus upslope areas was not significantly different (Tables 10a and 10b). Therefore, only distance was further examined as the explanatory variable. Including the quadratic term $distance^2$ did not make much

improvement over the first-order distance only model (Table 10b). Although the AIC score decreased slightly from 199.776 to 198.357, the BIC score increased from 208.57 to 211.548. Moreover, both *distance* and $distance^2$ had *p*-values larger than 0.05 (Table 10b). BIC's stronger penalization for the number of parameters and the high *p*-values when the quadratic term was included suggested that mortality was nearly linearly related to distance from road and the *distance* only model should be selected. The effect of every 10-m increase in distance from road edge was estimated to be a 26.5% (95% *CI*: 4.8% to 43.2%) decrease in probability of mortality, for trees within 60m of the road (Figure 20).

Table 10a. Logistic regression model to assess the effects of distance and slope on tree mortality (threshold=-0.2) rate using 1993–1999 data, within the 0–60m zone from the road.

Variable	Coefficient	Std. error	*z*-statistic	*p*-value
Intercept	-1.606	0.294	-5.460	0.000
distance	-0.0149	0.0084	-1.762	0.078
downslope	0.4736	0.1206	-1.812	0.070
Deviance = 370.052	DF= 597			

Table 10b. Logistic regression model to assess the effects of distance and slope on tree mortality (threshold=-0.4) rate using 1993–1999 data, within the 0–60m zone from the road.

Variable	Coefficient	Std. error	*z*-statistic	*p*-value
Intercept	-2.070	0.403	-5.141	0.000
distance	-0.0304	0.0132	-2.312	0.021
downslope	-0.7627	0.4785	-1.594	0.111
Deviance = 192.990	DF = 597	AIC = 198.990	BIC = 212.181	
Intercept	-3.277	0.723	-4.530	0.000
distance	0.069236	0.059737	1.159	0.246
$distance^2$	-0.001837	0.001085	-1.693	0.091
Deviance = 192.357	DF = 597	AIC = 198.357	BIC = 211.548	
Intercept	-2.314	0.383	-6.039	0.000
distance	-0.0307	0.0132	-2.336	0.019

Deviance = 195.776	DF = 598	AIC = 199.776	BIC = 208.570

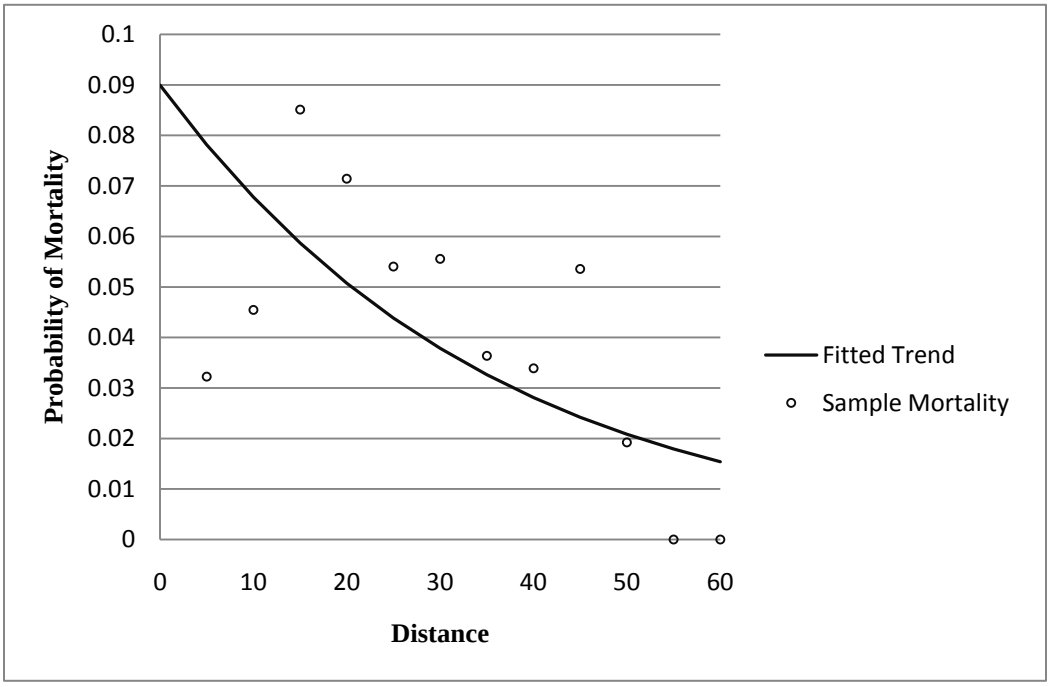

Figure 20. Fit of logistic regression model for mortality, with distance as explanatory variable to examine road-related effects within 60m of the road.

When considering all samples from within the 0–120m zone, there was strong evidence of an interaction effect between distance and slope (Table 11). The odds of mortality were associated with distance differently for downslope than for upslope. The resulting logistic model was as follows:

$$\text{logit}(\hat{\pi}) = -2.29 - 0.0186\textit{distance} - 1.3596\textit{downslope} + 0.0229\textit{distance} \times \textit{downslope}$$

For downslope (downslope=1), the model became: logit ($\hat{\pi}$) = -3.65 + 0.004234*distance*. The odds ratio was 1.043 (95% *CI*: 0.735 to 1.480) with every 10m increase in distance from road. This was not a significant increasing trend since the confidence interval included 1.

For upslope (downslope=0), the model became: logit ($\hat{\pi}$) = -2.29 – 0.018637*distance*. The odds ratio was 0.830 (95% *CI*: 0.727 to 0.947) with every 10m increase in distance from road. A

distinct trend of decreasing mortality with increasing distance from the road remained from the 0–60m zone to 0–120m zone for upslope trees (Figure 19).

Table 11. Logistic regression model to assess the effects of distance and slope (with interaction term) on tree mortality (threshold=-0.4) rate using 1993–1999 data.

Variable	Coefficient	Std. error	*z*-statistic	*p*-value
Intercept	-2.290	0.345	-6.633	0.000
distance	-0.018637	0.006750	-2.761	0.006
downslope	-1.359618	0.675879	-2.012	0.044
distance×*downslope*	0.022871	0.011097	2.061	0.039
Deviance = 318.309		Degrees of freedom = 1054		

3.8 Temporal Patterns of Tree Crown Mortality

3.8.1 Comparison between wet years and dry years

There was strong evidence of an interaction effect between *salt* and *distance* (Table 12). In years of high salt application (1993–1999), i.e. *salt* = 1, the model became: logit ($\hat{\pi}$) = -2.314 - 0.031*distance*, which was the same as the model in Table 10b. As discussed before, this model clearly captured the effects of distance on mortality and suggested the existence of de-icing salt caused tree crown damage. In years of low salt application (2003–2009), i.e. *salt* = 0, the model was: logit ($\hat{\pi}$) = -2.299 + 0.029*distance*, which estimated the effect of distance to be an increase in the odds of mortality by a multiplicative factor of exp (0.029×10) = 1.336 (95% *CI*: 1.259 to 1.419), if distance increases 10 meters.

The odds ratio of mortality from 1993 to 1999 (wetter years) relative to from 2003 to 2009 (drier years) was approximately 0.98 at 0m from road, 0.54 at 10m from road, 0.30 at 20m

from road, and so on. Generally, wet years had lower levels of mortality than dry years across the Basin (Figure 14).

Table 12. Logistic regression model to assess the effects of distance (0–60m) and wet (salt=1)/dry (salt=0) years on tree mortality (threshold=-0.4) rate using 1993–1999 and 2003–2009 change data.

Variable	Coefficient	Std. Error	*z*-statistic	*p*-value
Intercept	-2.299	0.255	-9.025	0.000
distance	0.029	0.006	4.528	0.000
salt	-0.015	0.460	-0.033	0.974
distance×*salt*	-0.060	0.015	-4.085	0.000
Deviance = 795.928		DF = 1196		

3.8.2 Long-term trend from 1990 to 2010

The time series data from 1990 to 2010 showed positive correlations between mortality and salt and between mortality and precipitation, and a negative correlation between mortality and traffic (Figure 21). There was a possible one-year delay of tree crown mortality response to salt application as shown in the "lag scatterplot" of Figure 21b compared to Figure 21a.

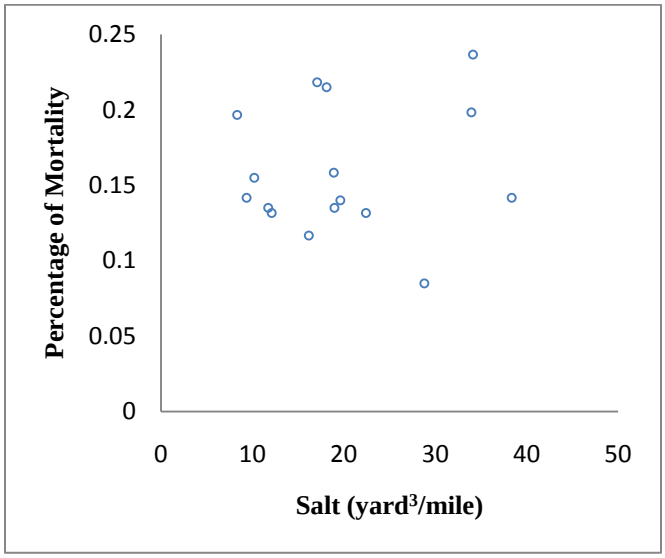

(a)

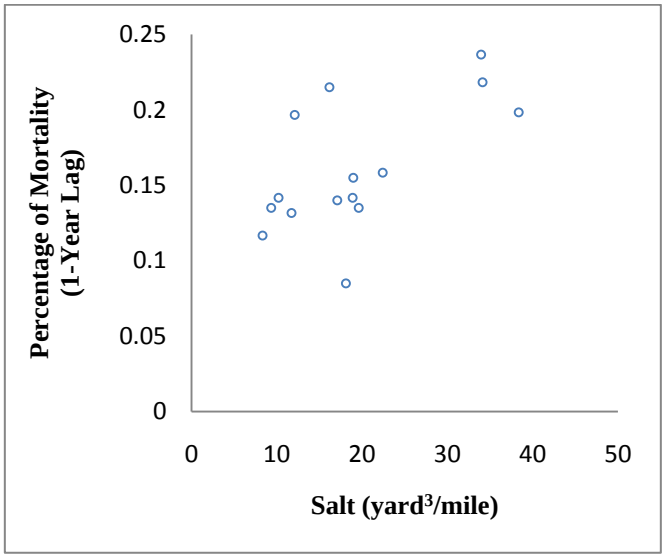

(b)

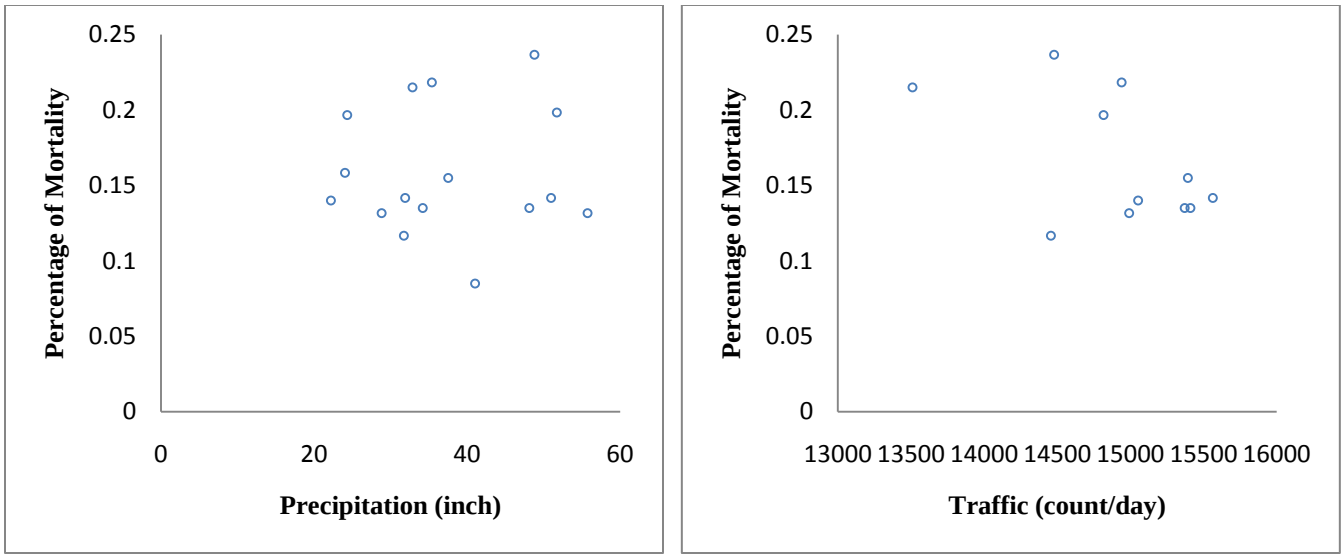

(c) (d)

Figure 21. Scatterplots of mortality proportion as a function of (a), (b) salt application (1990–2010), (c) precipitation (1990–2010), and (d) traffic (1999–2009 *MADT*), respectively. In (b), there is 1-year lag in response of mortality to salt application.

When the traffic data (*MADT*) from 1999 to 2009 together with salt and precipitation data were used to fit the full model (39), *salt* and *precipitation* had significant interaction (*p*-value = 0.030) and *MADT* had strong additive effect (*p*-value < 0.001) (Table 13a). From 1999 to 2009, *MADT* only varied from 13511 to 15564. The year-to-year average change in *MADT* was about 200. An increase in winter daily traffic by 200 count/day was only associated with a 4.2% (95% *CI*: 1.9% to 6.4%) decrease in the odds of mortality. Therefore, I focused on examining the interaction effect between *salt* and *precipitation*:

$$\text{logit}(\pi) = \beta_0 + \beta_1 salt + \beta_2 precipitation + \beta_3 salt \times precipitation.$$

The drop-in-deviance test on the interaction term gave *LRT* = 5.20, and *p*-value = 0.022, which suggested *salt* and *precipitation* had significant interaction effect (Table 13b). The influence of salt application on the odds ratio of mortality was dependent on precipitation. In wetter years, every 10 yard^3/mile increase in salt application had stronger effect on the odds of

mortality (Figure 22a). De-icing salt effects were more distinct in wet years than in dry years (Figure 22b).

No matter whether precipitation or traffic was included in the model or not, salt application was consistently the strongest explanatory variable. Without considering other factors (i.e. simple regression with *salt* as the only variable), a median increase in the amount of salt applied by 10 yard^3/mile was estimated to cause 7.8% (95% *CI*: 3.1% to 12.6%) increase in the odds of mortality.

Table 13a. The full model to test the effects of salt, precipitation and *MADT* in de-icing salt effect prone area (0–60m) using 1999–2009 data.

Variable	Coefficient	Std. Error	*z*-statistic	*p*-value
Intercept	1.8915	0.9061	2.087	0.037
salt	-0.0189	0.0134	-1.418	0.156
precipitation	-0.0119	0.0064	-1.870	0.061
MADT	-2.14E-04	5.96E-05	-3.597	0.000
salt×*precipitation*	6.83E-04	3.14E-04	2.171	0.030
Deviance = 5891.636	DF= 6595			

Table 13b. The best supported model to test the interaction effects of salt and precipitation in de-icing salt effect prone area (0–60m) using 1990–2010 data.

Variable	Coefficient	Std. Error	*z*-statistic	*p*-value
Intercept	-1.326	0.216	-6.148	0.000
salt	-0.014296	0.010152	-1.408	0.159
precipitation	-0.012680	0.005432	-2.334	0.020
salt×*precipitation*	0.000518	0.000227	2.280	0.023
Deviance = 8378.506	DF = 9596	AIC = 8386.506	BIC = 8415.184	

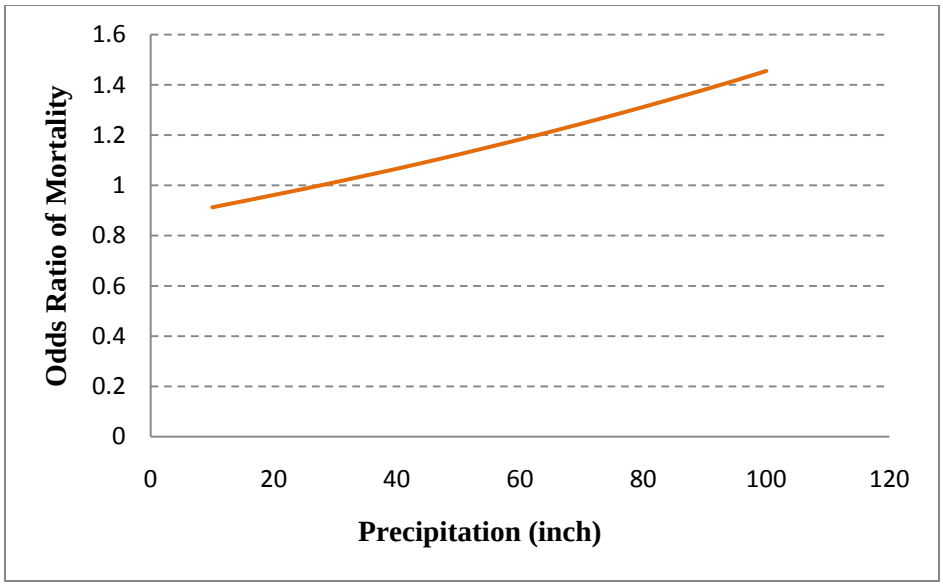

(a)

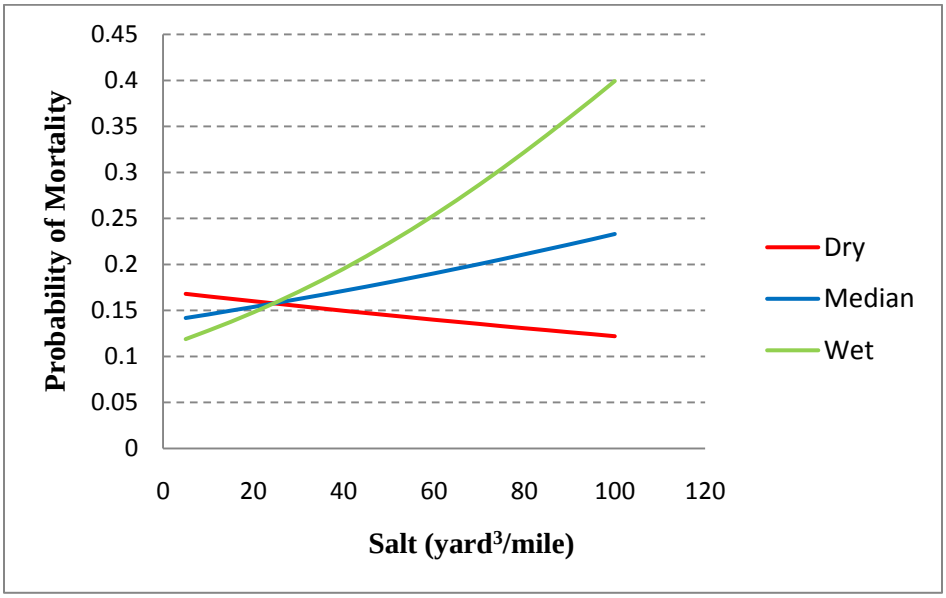

(b)

Figure 22. Interaction effects between salt and precipitation: (a) the odds ratio of mortality with every 10 yard^3/mile increase in salt application; (b) the effects of salt application on the probability of mortality during dry, median and wet years.

4 Discussion

4.1 Topographic Correction of Remote Sensing Imagery

Although some vegetation indices such as NDVI cancel out topographic effects by per-pixel normalization in their equations, there is still significant influence of diffuse irradiance from atmospheric and terrain sources that cannot be addressed by vegetation indices alone. In other words, any topographic correction method that uses a single multiplicative correcting factor for all spectral bands (e.g. Cosine Correction) has no effect on simple ratio-based vegetation indices (e.g. NDVI), but the C-Correction, SCS+C and SCnS+C correction methods incorporate band-specific *C* parameters to account for diffuse irradiance; therefore these transformations should be performed before calculating vegetation indices.

Visible bands (blue, green and red) of both Landsat TM5 and IKONOS are within the range of 0.45~0.69 μm wavelength, which is strongly absorbed by green canopy. Irradiance of these bands at the ground is therefore limited to that coming directly from the sun and sky through canopy gaps. Thus, tree crowns play a more important role than the ground surface in the reflectance of visible bands, and the Sun-Crown-Sensor model demonstrates an advantage. However, vegetation canopy (esp. conifers) without high canopy closure will scatter and transmit a significant amount of near-infrared (0.76~0.90 μm for both Landsat TM5 and IKONOS) flux to the ground surface underneath the canopy as well as through canopy gaps. The ground surface subsequently reflects part of this scattered and transmitted flux back to the sensor (Huete 1988). Therefore, terrain does have increased influence for near-infrared (NIR) band especially when the canopy closure is low (for coarse resolution imagery) or tree crowns have low LAI (for high resolution imagery) which violates the assumptions of Sun-Canopy-Sensor or Sun-Crown-Sensor model. Although the regressions in Figure 11 use tree pixels (> 80% covered by tree crown

according to LiDAR tree crown mask), many of them are not dense tree crowns (esp. Jeffrey pine) which allow enough transmission of the near-infrared flux to the ground. That is why the Sun-Crown-Sensor model only shows marginal advantage in the NIR band. This is in accordance with the finding of Gu and Gillespie (1998) that the Sun-Canopy-Sensor model is more appropriate than the Sun-Terrain-Sensor model for canopies of 50% or higher canopy closure on Landsat imagery. Due to the complex contribution of near-infrared reflectance from terrain background and from tree crowns, none of the equations can depict the correlation for near-infrared bands better than for visible bands. Nevertheless, the obvious advantage of the Sun-Crown-Sensor model over the other two in the visible bands supports the using of the Sun-Crown-Sensor model in this study.

In Table 1, the Sun-Crown-Sensor model (without C) had the highest R^2 but a low EF statistic. This was because the original Sun-Crown-Sensor model explained most of the data variance associated with terrain-regulated illumination on tree crowns (i.e. $\frac{cos\, i}{cos\, i_s}$) in equation (19), which gave high R^2, and the diffusive effects of atmosphere were largely captured in the parameter $C = b/m$ of equation (19), which was not included in the original SCnS model (Equation (15)) and thus a low EF was obtained, indicating consistently biased over-estimation. Therefore, it was not surprising that when the atmospheric effects contained in C was accounted for in the SCnS+C model, it had the best performance as measured by R^2, RMSE, EF, and δ_ρ together. So, the SCnS model and the C parameter based on it should be combined in practice to have the best topographic correction results.

The SCnS+C model is recommended for topographic correction of forest images and its utility can be further tested in applications where other types of vegetation cover and terrain conditions are considered.

4.2 Different Vegetation Indices

Using ground reference data collected at two different points of time to calibrate change detection is hampered by time and sampling method. Single year vegetation indices provide a way to circumvent the problem, because single year ground reference data are much easier to obtain and the sampling method can be modified at any time without the need to recalibrate with previous year's data. The calibrated relationships between current vegetation indices and actual forest canopy attributes (e.g. LAI, healthy canopy cover, and foliage biomass) can be generalized to the same study area for previous years, given that there is little temporal variation in soil background and other environmental conditions for the same location and only the characteristics of canopy itself change over time including density, structure, species composition and greenness. Although the LAI data were obtained in a single year, they already contain such canopy variations across different plots as if they were the variations in the same canopy across different years.

In the comparison of the four vegetation indices, results did not show any advantage of the soil adjusted VIs over NDVI, no matter whether linear functions or exponential functions were fitted. When the linear model was used, NDVI had the most significant relationship with field LAI data. MSAVI and SAVI (L=0.5), which were intended to correct for soil background effects and enhance the power of predicting LAI, did not show better performance than other soil-sensitive indices. However, SAVI and MSAVI might outperform soil-sensitive vegetation indices in studies that encompass different soil types. There is not much variation in soil types in the relatively uniform areas near roads in the Lake Tahoe basin, especially when ground reference data were collected in easy-accessible locations where soils are similar. Moreover, many other random effects such as understory (e.g. grass) noises and LAI measurement errors

might cancel each other out. The multiple regression using the three Tasseled Cap indices revealed that Greenness was the only significant predictor for estimating LAI, while Wetness and Brightness were both insignificant. This strongly contrasts with Collins and Woodcook's (1996) conclusion at the same study area that change in Tasseled Cap Wetness (i.e. MKT Wetness) was the most reliable single indicator of forest change.

When the suitability of these indices was evaluated by fitting the non-linear relationship between VI and LAI using the semi-empirical model, NDVI yielded the most reasonable values for parameters VI_∞ and K_{VI}, while other indices resulted in negative K_{VI} values or VI_∞ smaller than VI_g that were useless. Therefore, the semi-empirical model using NDVI was chosen to transform remote sensing data to LAI data in this study.

White et al. (1997) also showed that NDVI provided the best estimate of LAI but decreased in predictive ability with decreasing spatial resolution as a result of pixel aggregation and averaging. Therefore, for IKONOS image, averaging the original 4×4m pixels at a 30×30m plot level in order to be related to LAI data might undermine the accuracy of LAI estimation. In addition, satellite-derived vegetation indices are optical measures of canopy greenness, a composite property of leaf chlorophyll content, leaf area, canopy cover and structure, but they have often been employed as proxies for individual vegetation attributes such as canopy cover or LAI. These attributes as a portion of the composite canopy property, when used individually, are only moderately correlated with vegetation indices (Glenn et al. 2008). Therefore, using vegetation indices to estimate these parameters (e.g. LAI) separately is subject to uncertainty, although the final VI-LAI model used in this study was well-calibrated.

The objective of this evaluation was not to test the advantage of a vegetation index in theory or in model, but to look for the practically suitable one for the actual conditions in this study area. NDVI, therefore, can be said to be the most suitable vegetation index in the context of this study, and is recommended for future monitoring of forest mortality associated with de-icing compounds along roads.

4.3 Different Change Detection Methods

The quantitatively estimated mortality from LAI change included mortality caused by many different factors including, but not limited to, de-icing salt damage (road-related), disease, insects, and drought (non-road-related). To isolate the component of tree crown mortality that was road-related, statistical analyses had to be applied to examine if a significant relationship between tree crown mortality and road-related variables could be found. These statistical analysis approaches are discussed in sections 4.5 and 4.6.

Comparing the quantitative change detection using IKONOS data with that using Landsat TM data, the disadvantages of IKONOS change detection include the sensitivity to subtle environmental variables such as topographic features and mutual shadowing among tree crowns, and the images' non-nadir collection angles which caused slight misalignment of tree crowns between two years (Sections 2.3.2.1 and 2.3.2.2). Although thorough image preprocessing techniques were employed to minimize the geometric and radiometric noises, some uncertainty might still exist. However, IKONOS data showed its significant advantage in discovering de-icing salt effects by virtue of its high resolution, especially with the aid of the two newly created spatial proxy variables for aerial deposition and flow accumulation of de-icing salt (Section 4.5.1). Landsat TM data were much more resistant to geometric and radiometric errors, but its

coarser resolution was not appropriate for fine-scale analysis on road-related effects. However, the historical records of Landsat TM data permitted long-term temporal analyses on the dynamics of roadside tree mortality, and together with historical salt application data they were able to reveal the effects of de-icing salt application on tree crown mortality in a convincing manner (Section 4.6). In summary, the long-term temporal analysis using Landsat TM data and the fine-scale spatial analysis using IKONOS data were complementary to each other in confirming road-related effects on tree crown mortality.

In the post-classification comparison approach, the analysis of de-icing salt effects would be much simpler if the spectral signature of de-icing salt damage could be directly identified in the multiple spectral bands. Unfortunately, IKONOS classification failed to differentiate de-icing salt damage from other mortality factors. The classification results showed that trees classified as salt-damaged were widely dispersed throughout the Basin. However, de-icing salt damage should only exist near roads according to field studies. This suggests that tree crown mortality can be well extracted by classification using IKONOS images, but whether it is caused by de-icing salt or by other factors cannot be distinguished. The spectral characteristics of de-icing salt damage might not have significant differences from other kinds of tree crown damage, or the four coarse-spectral-resolution bands of IKONOS (similar to Landsat TM data) might not be appropriate or sufficient to capture the subtle variation in spectral response of different damage types. Hyperspectral remote sensing data should be used instead of multispectral data (White et al. 2007) in the future if one attempts to classify de-icing salt caused tree crowns mortality directly.

Nevertheless, the classification results were informative. Trees were generally healthier in 2009 than in 2005. Many trees had changed from being unhealthy to healthy in this 4-year period. This was consistent with the fact that there was a prolonged extensive drought before

2005 (from 2000 to 2004). Therefore, trees in 2005 were generally under the stress of drought and more mortality occurred across the Basin. Several years after the drought, the forest likely experienced increased growth, regeneration and canopy vigor. However, the higher proportion of mortality near roads in 2009 than in 2005 especially within the 0–30m zone was very likely due to significantly higher amounts of de-icing salt applied in 2009 (18.1 $yard^3$/mile) than in 2005 (11.7 $yard^3$/mile) (Appendix C). This phenomenon was also consistent with that found in quantitative change detection analyses. It can be inferred that de-icing salt effects controlled mortality in close vicinity to roads while drought affected mortality at a broad-scale across the Basin.

4.4 Calibration and Validation

4.4.1 Calibration

Most field data only allow for calibration of drastic change (e.g. clear-cut, drastic beetle attack) but not of fine-scale tree health change. For example, the field morphological and pathological data (Section 2.2.1.1) only recorded crown damage ratings and health status of trees categorically. My variable of interest was tree crown mortality, with the component of road-related mortality (e.g. caused by de-icing salt) especially subtle, because the observable symptoms of de-icing salt damage on tree crowns mainly include loss of photosynthetic materials (yellowing) in the tips of needles. The categorical field mortality data were, therefore, not suitable for calibrating quantitative change detection, but only sufficient for the purpose of validation. In this context, the field survey strategy in 2010 was modified to measure LAI quantitatively (Section 2.2.1.2). The calibrated VI-LAI relations were used to transform individual years' VI to LAI. ΔLAI was the predictor of tree crown mortality which was validated by field morphological and pathological data. Although the LAI data were obtained in a single

year, the sampling design ensured that the data contained variations in canopy attributes across different plots as if they were the variations in the same canopy across different years. Therefore, the VI-LAI relationship calibrated using these LAI data can explain variations in tree crown status both across sites and across years.

If digital change detection results (e.g. ΔNDVI, MKT components) instead of single-year vegetation indices had been calibrated directly using field mortality data, there would have been more challenges. Collins and Woodcock (1996) suggested that the exact relationships between change detection components (refer to digital MKT components) and field-observed mortality were quite variable between different pairs of images. Recalibration of change components to field measured mortality between different scenes or between different multi-temporal datasets covering the same area was recommended. This requires that multiple years of corresponding field datasets should be available for calibrating each change detection dataset, which undermines the generalizability of remote sensing in historical change detection where precise calibration datasets are often not available retrospectively. Even for a single pair of images, using ground reference data collected at two different points of time corresponding to the pair of images to calibrate change detection of tree health was hampered by field sampling method. Thus, my approach for calibration and validation as shown in Figures (3) or (4) provided a way to circumvent the problems of calibrating multi-temporal change detection.

4.4.2 Validation

The growth rate model did not work better than using a constant growth rate in the validation. This was probably because equation (34) calculated the maximum diameter growth without considering competition, disease and other site-specific parameters and therefore

overestimation could occur. The increase in canopy cover of living trees from 2006 to 2009, without considering other factors, calculated by this method ranged from 3% to 20% for all plots. The average rate was 10%. This was similar to the estimated constant growth rate 5% used in equation (33) for some plots. Most plots had larger growth rates which might be overestimated by equation (34).

An issue with the validation field data was that we only measured tree DBH. Estimating canopy cover or foliage biomass from DBH by allometric models was inherently hampered by the variation in crown morphology associated with tree density, physiology, geography and many other factors. So, future field survey should include measuring crown radius or canopy cover directly or using radiometer to measure LAI for multiple years, in order to validate remote sensing estimated LAI change. In addition, to accurately measure growth rate, timber core samples should be obtained from living trees and their DBH growth in the past can be retrieved by measuring the width of annual growth rings.

Plot size was also another issue with the field data. We designed the plots as 30m×30m squares that could exactly correspond to pixels on Landsat TM image. Pixel-size plots might be too small, and thus too sensitive to the misregistration between Landsat images. Justice and Townshend (1981) suggested the plot size to be P (1+2L), P is pixel size and L is the positional accuracy of the geometric registration in terms of pixels. Therefore, 60×60m should be a better plot size for the Landsat TM data.

In addition, we measured all trees (>10cm DBH) in a plot and canopy cover was derived by summing the crown area regardless of canopy overlap, while satellite sensors can only sense the outer layer of canopy. The overall aboveground biomass will be inherently underestimated by

optical sensors. Thus errors could occur when using overestimated field data to validate underestimated remote sensing results. This was likely the reason, in addition to the imperfectness of the field validation dataset, why remote sensing estimated ΔLAI from 2006 to 2009 had negative values for most validation sites but the modeled canopy cover or foliage biomass from field data increased at many sites.

4.5 Spatial Pattern of Tree Crown Mortality Associated with Roads

4.5.1 Fine Scale

The clear trend of tree crown mortality within 100m of roads was consistent with the finding from field studies that de-icing salt effects existed mainly within 101 feet ≈ 30m from road (Munck et al. 2010). It was surprising that upslope areas had higher mortality probability than downslope areas irrespective of distance from road (Figure 18, Table 6). This should be associated with factors other than de-icing salt effects, since both mechanisms of de-icing salt dispersal (i.e. aerial deposition and flow accumulation) are limited in upslope areas.

The two proxy variables for aerial deposition and flow accumulation of de-icing salt proved their advantage in revealing de-icing salt effects on tree crown mortality. The aerial deposition mechanism had strong significant effects, while the flow accumulation mechanism was only weakly associated with tree mortality. The mortality threshold of -20% ΔLAI was better than -40% in modeling de-icing salt effects especially for the flow accumulation mechanism, which implied that de-icing salt damage through soil uptake was associated with smaller degrees of tree crown mortality. On the contrary, the -40% threshold value revealed stronger aerial deposition effects, which suggested that direct aerial deposition of de-icing salt onto tree crowns near road damaged trees to a larger degree.

The fact that flow accumulation near roads was usually very low relative to more distant downslope areas could explain why the effect of flow accumulation of de-icing salt was unobservable within 30m of the road, but more distinct at a broader scale (0–100m). Comparing Table 7 and Table 8, an inference can be drawn that de-icing salt effects via aerial deposition mechanism was stronger in the 0–30m zone than in more distant zone, while the effect of soil uptake of de-icing salt was only observable in a broader zone where the accumulation of salt through water flow was high enough to show significant effects. Overall, the effects of aerial deposition of salts played a major role in roadside tree crown mortality, whereas the flow accumulation mechanism was statistically significant but only exerted weak effects.

4.5.2 Broad Scale

The small increase in mortality probability from 60m to 120m (Figure 19), especially for downslope, was a hint that a decreasing trend of mortality probability with increasing distance from road mainly existed within 60m of the road and the trend was likely masked by other stronger factors that were not measured. This agrees with the field findings of very limited de-icing salt symptoms beyond 30m from road and increased mortality caused by other factors such as diseases (Munck et al. 2010). This trend was also apparent using the higher resolution IKONOS imagery (Figure 18) where there was a similar abrupt increase of mortality after the drastic decrease, once when distance from the road had exceeded 30 m.

The logistic regression results provided strong circumstantial evidence of de-icing salt effects on tree crown mortality, and pointed to aerial deposition of salt spray as the most likely mechanism. The effect of distance on mortality was largely linear in the close vicinity of road (0–60m). The chance of spread of de-icing salt onto roadside tree crowns, especially through

aerial deposition mechanism, is also considered to be inversely proportional to increasing distance from road. Trees closer to the road are more susceptible to de-icing salt. Trees farther away are more likely to be protected by the front trees from aerial spray of salt. It is necessary to note that although the sample mortality and modeled mortality probability in Figure 20 were estimated for every 10m interval of distance (measured from pixel center) for better illustration, the 30-m resolution of Landsat TM data may cause some uncertainty in analyses below 30-m scale.

When considering the broader zone (0–120m), the odds of mortality were not significantly affected by the distance from road in downslope areas. Combining the results from previous 0–60m zone analysis, it can be said that mortality probability near roads (0–60m) follows the hypothesis of de-icing salt effects but it is no longer significantly higher than that farther from roads after 60m in downslope areas. As found in the fine-scale analysis, de-icing salt effects via flow accumulation in downslope area was significant in the 0–100m zone, but not observable within 30m due to too low flow accumulation values. It suggests that flow accumulation of de-icing salt and its effect tends to be higher in farther distance and therefore compensates the decreased effect from aerial deposition of de-icing salt. This can explain the abrupt increase in mortality beyond 60m following the decease within 60m which altered the overall trend within 120m in downslope areas.

In upslope areas there was no de-icing salt contact through flow accumulation and only aerial deposition was possible. Thus the trend of mortality observed in upslope was consistent with aerial mechanisms for road-related mortality and contrasted with the trend in downslope areas within the 120m zone. Within 0–60m from road, the difference in mortality probability between downslope and upslope was not significant (Table 10b), but from 0–120m, the

probability of mortality was higher in downslope than in upslope. For example, according to the fitted model, at 90m from road, the odds ratio of mortality in downslope relative to upslope is exp(-3.65+0.004234×90)/exp(-2.29-0.018637×90) = 2.01. It is suggestive evidence that some additional de-icing salt effects may exist in more distant downslope areas through the flow accumulation mechanism. This is in accordance with the findings in the fine-scale analysis that de-icing salt effects through flow accumulation was stronger in more distant (>30m) downslope areas and compensates the decreased aerial salt deposition effect, although the 2005–2009 IKONOS change detection data did not show more mortality in downslope than in upslope sites. With the Landsat TM dataset, it can only be suggested but not concluded that the maximum zone of de-icing salt effects may extend beyond 60m to 120m from the road in downslope areas.

4.6 Temporal Patterns of Tree Crown Mortality Associated with Roads

In the first level of temporal analysis, the odds of mortality were estimated to increase by 1.336 (95% *CI*: 1.259 to 1.419) with every 10 m increase in distance from the road, in dry years of low salt application. This contradicted the distinct negative effect of road distance in wet years when large amounts of salt were applied. Thus the positive road-related trend in these dry years was not likely associated with de-icing salt effects. Nowak et al. (2008) and Munck et al. (2010) found that there was an increasing trend of mortality caused by factors including diseases but excluding de-icing salt with increasing distance from road, which was antagonistic rather than synergistic to salt damage. Trees were more likely to be damaged by something other than salt especially in dry years. Therefore, this result suggested that de-icing salt effects were weak and masked by other stronger factors in dry years with much less salt application.

In wet years, the significantly higher level of precipitation may strengthen tree vigor and decrease trees' vulnerability to damage. Thus it is not surprising that wet years had lower

mortality probability then dry years even in the salt-affected zone near road. On the other hand, more snowfall in wet years leads to more splash generation and snow ploughing (Blomqvist and Johansson, 1999), which increases the probability of aerial deposition of de-icing salt onto roadside ground and tree crowns and therefore increases de-icing salt damage. The generally lower mortality or higher tree vigor across the Basin in combination with the stronger de-icing salt damage near roads in wet years rendered the distance-controlled pattern of mortality especially distinct and strongly suggested the existence of de-icing salt effects. When de-icing salt effects were negligible in dry years, other damaging agents drove the spatial pattern of mortality along roads and precipitation, on the other hand, determined the general degree of mortality across the Basin.

In the long-term temporal analysis, a clear effect of de-icing salt on mortality probability was revealed, while the interpretation for precipitation and traffic was more complicated. Although the *MADT* data were measured for winter seasons, they could not represent the exact traffic situation during snowing days when traffic could influence de-icing salt effects especially through the aerial deposition mechanism. Moreover, the facts that *MADT* data only spanned 10 years and the year-to-year variation was only approximately 200 (count/day) while the range was from 13511 to 15564, limited the sample size and data distribution for a long-term temporal analysis. That was why *MADT* showed statistically significant but very weak negative effects on roadside tree crown mortality. The traffic variable was not further analyzed.

The final best-supported logistic regression model revealed a significant interaction effect between salt application and precipitation (Figure 22). De-icing salt effects were more distinct in wet years than in dry years. In dry years (e.g. precipitation < 30 inches) the effects of salt were not observable. Other stronger damaging factors under the stress of drought might mask the

weak salt effects because of lower salt applications in dry winters. This was consistent with the previous findings from the wet-dry comparison using the two image pairs. In summary, the temporal analyses clearly suggested that de-icing salt damage on tree crowns were evident when high amounts of salt were applied and other damaging agents were weak due to stronger tree vigor associated with higher precipitation.

In addition, I noted that conifers retain foliage for several years, so foliage produced in the current year that is salt damaged will be observed and recorded for at least 1 (and likely 2 or 3) more years and thus there is a carry-over effect coupled with the sequence of dry-wet years (low-high salt damage) (Munck et al. 2010). Figure 21 showed obvious delay (about 1 year) of response in mortality to variation in salt application (annual summary data), which was very likely caused by the carry-over effect. Precipitation also had similar lag effects on mortality. Further examinations on these phenomena are needed in future studies to discriminate and quantify immediate effects and lagged effects of salt damage on conifer tree crowns.

Overall, convincing evidence of de-icing salt effects was found in the results of temporal analysis. Salt application was consistently the strongest explanatory variable, regardless of whether precipitation or traffic was considered.

4.7 Management Implications

The remote sensing methodologies and observed spatial and temporal patterns of tree crown mortality suggest several management implications.

1) Landsat TM images are a useful remote sensing data source for retrieving historical road-related forest mortality and monitoring future tree health change in a broad-scale

and long-term context. Higher resolution imagery is necessary for examining fine-scale patterns of de-icing salt effects, although it is more costly and requires considerable efforts in data preprocessing. Robust remote sensing protocols for monitoring road-related tree crown mortality will adopt a multi-scale approach, adopting imagery from remote sensing platforms with varying spatial and temporal resolution.

2) Aerial deposition of de-icing salt onto tree crowns by moving vehicles has a much stronger effect than does flow accumulation. It affects tree health mostly within 30m of the road. Therefore, tree species that are more resistant to de-icing salt damage could be planted as a barrier within the 0–30m zone from roads to protect other trees behind it. Taller trees could be planted on concave slopes.

3) De-icing salt application is a significant factor for roadside tree crown mortality. Road management should continue efforts to decrease the amount of de-icing salt used in winter or to use less deleterious alternative materials.

4) Trees at the roadside are generally healthier but salt damage is more distinct in wet years than in dry years. Under the stress of drought, other mortality agents become stronger although de-icing salt damage is not observable as such by remote sensing. This implies mitigation strategies should be focused on de-icing salt effects in wet years while paying more attention to other damaging factors in dry years, in order to maintain roadside tree health and the ecological and aesthetic values of the Lake Tahoe Basin.

5 Conclusions

This study introduced several innovations in remote sensing methodologies and demonstrated the utility of applying remote sensing techniques to detect road-related effects on tree crown mortality. Several conclusions regarding remote sensing methods and tree mortality in the Lake Tahoe Basin were drawn:

1) **The Sun-Crown-Sensor (+C) topographic correction methods are theoretically well-founded and outperformed other commonly used methods in correcting for radiometric distortions caused by terrain in forest satellite images.** The Sun-Crown-Sensor model considers different viewing angles and is generally applicable to IKONOS, Landsat TM and other multispectral images with forest as the major land cover type. The C parameter derived based on the Sun-Crown-Sensor geometry also significantly improved model accuracy compared to the original C-correction. Combining the new Sun-Crown-Sensor model and the new method of deriving C, the Sun-Crown-Sensor+C topographic correction method is recommended for radiometrically correcting forest images.

2) **LiDAR proved its utility as important ancillary data in this study.** The high resolution and geometric accuracy of LiDAR DEM data greatly improved the accuracy in orthorectifying IKONOS images, and a novel method was developed to create a projected tree crown mask from LiDAR DEM and DSM data that helped focus the analyses on tree crowns.

3) **NDVI was consistently ranked as the best vegetation index for predicting LAI and ΔLAI was an appropriate predictor of tree crown mortality in this study.** The

collection of LAI field data enabled calibrating remote sensing data into quantitative LAI of physical meaning. Change in LAI was used to define tree crown mortality. The more qualitative forest morphologic and pathological survey data were used to validate remote sensing estimated mortality.

4) **Quantitative change detection by LAI differencing using multispectral images was successful in discovering road-related effects (including de-icing salt effects) on tree crown mortality**. Qualitative change detection by classifying multispectral images was not able to detect the spectral signature of de-icing salt damage on tree crowns directly. Hyperspectral remote sensing data are needed in future studies if the objective is to directly classify tree crown mortality caused by de-icing salt.

5) **Using IKONOS images and the two spatial proxy variables, a significant effect of increasing mortality associated with increasing aerial deposition of de-icing salt was revealed.** Aerial deposition was the primary mechanism of de-icing salt effects which was most distinct within 30m of the road, whereas flow accumulation effect tended to be statistically significant at more distant locations (30–100m) although the actual effect was very weak relative to aerial deposition.

6) **The spatial analysis using Landsat TM images revealed that a decreasing trend of mortality with increasing distance from road mainly existed within 60m of the road but may extend beyond 60m to 120m from the road in downslope areas.** This agreed with the findings by IKONOS analysis and suggested the maximum zone of de-icing salt effects was within 120m of the road.

7) **The temporal analysis using Landsat TM images provided convincing evidence of de-icing salt effects on the probability of mortality.** Mortality increased with increasing amount of salt applied. The more precipitation there was, the more distinct the effects of de-icing salt were observed.

8) **The temporal analysis with salt application data complemented the spatial analysis in confirming that both the spatial pattern and temporal pattern of tree crown mortality near the roads were largely related to de-icing salt.**

6 Literature Cited

Asner, G. P., and A. S. Warner. 2003. Canopy shadow in IKONOS satellite observations of tropical forests and savannas. Remote Sensing of Environment 87:521-533.

Baret, F., and G. Guyot. 1991. Potentials and limits of vegetation indexes for LAI and APAR assessment. Remote Sensing of Environment 35:161-173.

Blomqvist, G., and E. L. Johansson. 1999. Airborne spreading and deposition of de-icing salt-a case study. Science of the Total Environment 235:161–168.

Bragg, D. C. 2001. Potential relative increment (PRI): a new method to empirically derive optimal tree diameter growth. Ecological Modeling 137:77–92.

Bryson, G. M., and A. V. Barker. 2002. Sodium accumulation in soils and plants along Massachusetts roadsides. Communications in Soil Science and Plant Analysis 33:67-78.

Canty, M. J., and A. A. Nielsen. 2008. Automatic radiometric normalization of multitemporal satellite imagery with the iteratively re-weighted MAD transformation. Remote Sensing of Environment 112:1025-1036.

Canty, M. J. 2011. The MAD MAN user's manual (Google Docs). Assessed January 2011. <http://mcanty.homepage.t-online.de/ >

Chavez, P. S. 1988. An improved dark-object subtraction technique for atmospheric scattering correction of multispectral data. Remote Sensing of Environment 24:459-479.

Chen, J., P. Gong, C. He, R. Pu, and P. Shi. 2003. Land-use/land-cover change detection using improved change-vector analysis. Photogrammetric Engineering and Remote Sensing 69:369-379.

Civco, D. L. 1989. Topographic normalization of Landsat Thematic Mapper digital imagery. Photogrammetric Engineering and Remote Sensing 55:1303–1309.

Clark, D. B., C. S. Castro, L. D. A. Alvarado, and J. M. Read. 2004. Quantifying mortality of tropical rain forest trees using high-spatial-resolution satellite data. Ecology Letters 7:52-59.

Colby, J. D. 1991. Topographic normalization in rugged terrain. Photogrammetric Engineering and Remote Sensing 57:531-537.

Collins, J. B., and C. E. Woodcock. 1996. An assessment of several linear change detection techniques for mapping forest mortality using multitemporal Landsat TM data. Remote Sensing of Environment 55:66-77.

Colwell, J. E. 1974. Vegetation canopy reflectance. Remote Sensing of Environment 3:175-183.

Coppin, P., I. Jonckheere, K. Nackaerts, and B. Muys. 2004. Digital change detection methods in ecosystem monitoring: a review. International Journal of Remote Sensing 25:1565-1596.

Crist, E. P., and R. C. Cicone. 1984a. Application of the Tasseled Cap concept to simulated thematic mapper data. Photogrammetric Engineering and Remote Sensing 50:343-353.

Crist, E. P., and R. C. Cicone. 1984b. A physically-based transformation of Thematic Mapper data-the TM Tasseled Cap. IEEE Transactions on Geoscience and Remote Sensing 22:256-263.

Du, Y., P. M. Teillet, and J. Cihlar. 2002. Radiometric normalization of multitemporal high-resolution satellite images with quality control for land cover change detection. Remote Sensing of Environment 82:123-134.

ERDAS, Inc. 2010. ERDAS IMAGINE 2010 Help. ERDAS, Inc., Norcross, Georgia, USA.

Forney, W., L. Richards, K. D. Adams, T. B. Minor, T. G. Rowe, J. L. Smith, and C. G. Raumann. 2001. Land Use Change and Effects on Water Quality and Ecosystem Health in the Lake Tahoe Basin, Nevada and California. USDI US Geological Survey, Open-File Report 01-418.

GeoEye, Inc. 2011. Product specifications. GeoEye, Inc., Herndon, Virginia, USA. Assessed September 2008. <http://www.geoeye.com/CorpSite/products-and-services/imagery-collection/satellite-imagery-products/product-specifications.aspx>.

Giesen, J. 2011. Sun-earth distance Java applet. Assessed March 2010. <http://www.geoastro.de/sundistance/index.htm>

Gill, S. J., G. S. Biging, and E. C. Murph. 2000. Modeling conifer tree crown radius and estimating canopy cover. Forest Ecology and Management 126:405-416.

Glenn, E. P., A. R. Huete, P. L. Nagler, and S. G. Nelson. 2008. Relationship between remotely-sensed vegetation indices, canopy attributes and plant physiological processes: what vegetation indices can and cannot tell us about the landscape. Sensors 8:2136-2160.

Gu, D., and A. Gillespie. 1998. Topographic normalization of Landsat TM images of forest based on subpixel sun-canopy-sensor geometry. Remote Sensing of Environment 64:166–175.

Guo, Q., M. Kelly, P. Gong, and D. Liu. 2007. An object-based classification approach in mapping tree mortality using high spatial resolution imagery. GISciences & Remote Sensing 44:24-47.

Hatfield, J. L., E. T. Kanemasu, C. Asrar, R. D. Jackson, P. J. Pinter, R. J. Reginato, and S. B. Ldso. 1985. Leaf-area estimates from spectral measurements over various planting dates of wheat. International Journal of Remote Sensing 6:167-175.

Huete, A. R. 1988. A soil-adjusted vegetation index (SAVI*).* Remote Sensing of Environment 25:295-309.

Huete, A. R., R. D. Jackson, and D. F. Post. 1985. Spectral response of a plant canopy with different soil backgrounds. Remote Sensing of Environment 17:37-53.

Jackson R. D., and A. R. Huete. 1991. Interpreting Vegetation Indexes. Preventive Veterinary Medicine 11:185-200.

Jenkins, J. C., D. C. Chojnacky, L. S. Heath, and R. A. Birdsey. 2003. Comprehensive Database of Diameter-based Biomass Regressions for North American Tree Species. USDA General Technical Report NE-319.

Jensen, J. R. 2005. Introductory digital image processing: a remote sensing perspective. Pearson Education, Inc. 210-220; 310-322; 474-491.

Kliejunas, J., M. Marosy, and J. Pronos. 1989. Conifer damage and mortality associated with highway de-icing and snow removal in the Lake Tahoe area. Forest Pest Management Report 89-11, USDA Forest Service, Pacific Southwest Region, Forest Pest Management Report No. 89-11.

Kauth, R. J., and G. S. Thomas. 1976. The Tasseled Cap-a graphic description of the spectral-temporal development of agricultural crops as seen by Landsat. Proceedings, Symposium on Machine Processing of Remotely Sensed Data, West Lafayette, IN: LARS, 41-45.

Key, C. H., and N. C. Benson. 2006. Landscape Assessment (LA): Sampling and Analysis Methods. USDA Forest Service, General Technical Report RMRS-GTR-164-CD.

LI-COR, Inc. 1992. LAI-2000 plant canopy analyzer instruction manual. LI-COR Inc., Lincoln, Nebraska, USA.

Liu, D., M. Kelly, and P. Gong. 2006. A spatial-temporal approach to monitoring forest disease spread using multi-temporal high spatial resolution imagery. Remote Sensing of Environment 101:167-180.

Lutes, J. 2004. Accuracy Analysis of Rational Polynomial Coefficients for IKONOS Imagery. Proceedings of ASPRS 2004 Conference, Denver, May 23-28, 2004.

Macomber, S. A., and C. E. Woodcock. 1994. Mapping and monitoring conifer mortality using remote sensing in the Lake Tahoe Basin. Remote Sensing of the Environment 50:255-266.

Manley, P. N., J. A. Fites-Kaufman, M. G. Barbour, M. D. Schlesinger, and D. M. Rizzo. 2000. Biological integrity. Pages 403-598 *in* D. D. Murphy and C. M. Knopp, editors. The Lake Tahoe Watershed Assessment. USDA Forest Service General Technical Report 175, Lake Tahoe Basin Management Unit, South Shore, California, USA.

Marshall, J. P. 1984. Evaluation of vegetation damage along Nevada highways in the Lake Tahoe Basin. Forest Pest Report 84-3. USDA Forest Service Boise Field Office, Boise, Idaho.

Massoth, H. 1978. Salt toxicity to conifers in the Lake Tahoe Basin. MS Thesis. University of Nevada, Reno.

Mayer, D. G., and D. G. Butler. 1993. Statistical validation. Ecological Modelling 68:21–32.

Meyer, P. 1992. Empirical quality assessment: effect of resampling on geometric and radiometric data quality using a region-based approach. Remote Sensing Laboratories, Department of Geography, University of Zurich-Irchel, Zurich, Switzerland.

Muchoney, D. M., and B. N. Haack. 1994. Change detection for monitoring forest defoliation. Photogrammetric Engineering and Remote Sensing 60:1243-1251.

Munck, I. A., C.M. Bennett, K.S. Camilli, and R. S. Nowak. 2010. Long-term impact of de-icing salts on tree health in the Lake Tahoe Basin: environmental influences and interactions with insects and diseases. Forest Ecology and Management 260: 1218–1229.

Nevada Department of Transportation (NDOT). 2010. NDOT Annual Traffic Report. Nevada department of transportation traffic information division in cooperation with the U.S. department of transportation federal highway administration, Carson City, Nevada, USA.

Nielsen, A. A. 2007. The regularized iteratively reweighted MAD method for change detection in multi- and hyperspectral data. IEEE Transactions on Image Processing 16:463-478.

OpenTopography Facility. 2011. Lake Tahoe Basin LiDAR. Accessed April 2011. <http://opentopo.sdsc.edu/gridsphere/gridsphere?gs_action=lidarDataset&cid=geonlidarframeportlet&opentopoID=OTLAS.032011.26910.1>

Qi, J., A. Chehbouni, A. R. Huete, Y. H. Kerr, and S. Sorooshian. 1994. A modified soil adjusted vegetation index. Remote Sensing of Environment 48:119-126.

Resource Concepts, Inc. (RCI). 1990. Roadside Erosion Control and Revegetation Needs Associated With the Use of De-Icing Salt Within the Lake Tahoe Basin. Report to Nevada/California Department of Transportation.

Riano, D., E. Chuvieco, J. Salas, and I. Aguado. 2003. Assessment of different topographic corrections in Landsat-TM data for mapping vegetation types. IEEE transactions on geoscience and remote sensing 41:1056-1061.

Rouse, J. W., R. H. Haas, J. A. Schell, and D. W. Deering. 1974. Monitoring Vegetation Systems in the Great Plains with ERTS. Proceedings, 3rd Earth Resource Technology Satellite (ERTS) symposium, Vol. 1, 48-62.

Scharpf, R. F., and M. Srago. 1974. Conifer damage and death associated with the use of highway deicing salt in the Lake Tahoe Basin of California and Nevada. USDA Forest Service-Forest Pest Control Technical Report 1.

Singh, A. 1989. Digital change detection techniques using remotely-sensed data. International Journal of Remote Sensing 10:989-1003.

Soenen, S. A., D. R. Peddle, and C. A. Coburn. 2005. SCS+C: A Modified Sun-Canopy-Sensor Topographic Correction in Forested Terrain. IEEE Transactions on Geoscience and Remote Sensing 43:2148-2159.

Song, C., C. E. Woodcock, K. C. Seto, M. P. Lenney, and S. A. Macomber. 2001. Classification and change detection using Landsat TM data: When and how to correct atmospheric effects. Remote Sensing of Environment 75:230-244.

Tahoe Regional Planning Agency (TRPA). 2008. Regional Transportation Plan-Mobility 2030. Accessed October 2008. < http://www.trpa.org/documents/docdwnlds/rtp_final.pdf>.

Taylor, M. 2011. IKONOS planetary reflectance and mean solar exoatmospheric irradiance. GeoEye, Inc., Herndon, Virginia, USA.

Teillet P. M., B. Guindon, and D. G. Goodenough. 1982. On the slope-aspect correction of multispectral scanner data. Canadian Journal of Remote Sensing 8:84-106.

USDI US Geological Survey (USGS). 2008. Landsat missions. Accessed October 2008. <http://landsat.usgs.gov/>.

USDI US Geological Survey (USGS). 2009a. National elevation dataset. Accessed September 2009. <http://ned.usgs.gov/>.

USDI US Geological Survey (USGS). 2009b. LANDFIRE data distribution site. Accessed December 2009. <http://landfire.cr.usgs.gov/viewer/>.

Van Delm, A., and H. Gulinck. 2009. Classification and quantification of green in the expanding urban and semi-urban complex: application of detailed field data and IKONOS-imagery. Ecological Indicators 11:52-60.

Walker, R. F., R. M. Fecko, W. B. Frederick, D. W. Johnson, and W. W. Miller. 2007. Forest health impacts of bark beetles, dwarf mistletoe, and blister rust in a Lake Tahoe Basin mixed conifer stand. Western North American Naturalist 67:562-571.

Western Regional Climate Center (WRCC), Desert Research Institute. 2008. Tahoe, California-Climate Summary (1903-2010 climate data). Accessed October 2008. <http://www.wrcc.dri.edu/cgi-bin/cliMAIN.pl?ca8758>.

White, J. C., N. C. Coops, T. Hilker, M. A. Wulder, and A. L. Carroll. 2007. Detecting mountain pine beetle red attack damage with EO-1 Hyperion moisture indices. International Journal of Remote Sensing 28:2111-2121.

White, J. D., S. W. Running, R. Nemani, R. E. Keane, and K. C. Ryan. 1997. Measurement and remote sensing of leaf area index in Rocky Mountain montane ecosystems. Canadian Journal of Forest Research 27:1714–1727.

Wulder, M. A., C. C. Dymond, J. C. White, D. G. Leckie, and A. L. Carroll. 2006. Surveying mountain pine beetle damage of forests: A review of remote sensing opportunities. Forest Ecology and Management 221:27-41.

Appendix A: Criteria for Selecting LAI Field Plots

The following is the list of criteria for selecting LAI field plots:

(1) There must be an opening with bigger than 60-m diameter near each plot for reference readings. Because forest canopy is tall, the above reference readings have to be made in an open site. A big enough opening makes sure that no radiation from adjacent vegetation is sensed by the lowest angle (74.1°) of the LAI-2000 sensor. Measurements are most accurate when taken under overcast sky conditions; under clear-sky conditions, scattering from direct radiation incident on canopy foliage results in underestimates of LAI. Due to the scarcity of overcast weathers in the Lake Tahoe Basin in summer and fall, measurements can only be taken during early morning or late evening when the sun approached the horizon. Therefore, a short distance from the reference open site to the sampling plot ensures there is enough time for repeated measurements between the open site and sampling plot.

(2) Plots should contain as little understory vegetation as possible. Understory vegetation is difficult to measure using the LI-COR sensor because it is usually below the lowest view angle (20° from horizon) of the equipment. Pure conifer plots enhance the relationship between LAI values and remote sensing data by minimizing noise caused by potentially different responses of LAI-2000 sensor and satellite sensor to variation in plant spectral properties.

(3) Plots should contain no dead trees retaining needles (yellow or still green) so that the measured LAI is the photosynthetically active leaf area index. Healthy tree plots also

make it possible to calibrate the 2009-09-27 IKONOS data with LAI measured in Sep. and Oct. 2010.

(4) Plots should be sampled across a sufficiently long gradient of tree density values, such that the regression against remote sensing vegetation indices will be robust across a broad range.

(5) Plots should vary in species composition such that the field data are more representative for the whole study area.

(6) Plots should be distributed at different elevations and with different slopes and aspects so that the data are more representative.

Appendix B: Satellite Images

Table B.1. All Landsat TM and IKONOS images used in this study.

Image Date	Scene Center Longitude/Latitude	Satellite	Sensor	Image ID
11-Sep-1988	120.1/38.9	Landsat 5	TM	L5043033_03319880911
03-Oct-1990	120.1/38.9	Landsat 5	TM	L5043033_03319901003
06-Oct-1991	120.1/38.9	Landsat 5	TM	L5043033_03319911006
22-Sep-1992	120.1/38.9	Landsat 5	TM	L5043033_03319920922
25-Sep-1993	120.1/38.9	Landsat 5	TM	L5043033_03319930925
15-Sep-1995	120.1/38.9	Landsat 5	TM	L5043033_03319950915
03-Oct-1996	120.1/38.9	Landsat 5	TM	L5043033_03319961003
09-Oct-1998	120.1/38.9	Landsat 5	TM	L5043033_03319981009
26-Sep-1999	120.1/38.9	Landsat 5	TM	L5043033_03319990926
12-Sep-2000	120.1/38.9	Landsat 5	TM	L5043033_03320000912
15-Sep-2001	120.1/38.9	Landsat 5	TM	L5043033_03320010915
02-Sep-2002	120.1/38.9	Landsat 5	TM	L5043033_03320020902
21-Sep-2003	120.1/38.9	Landsat 5	TM	L5043033_03320030921
23-Sep-2004	120.1/38.9	Landsat 5	TM	L5043033_03320040923
12-Oct-2005	120.1/38.9	Landsat 5	TM	L5043033_03320051012
29-Sep-2006	120.1/38.9	Landsat 5	TM	L5043033_03320060929
02-Oct-2007	120.1/38.9	Landsat 5	TM	L5043033_03320071002
18-Sep-2008	120.1/38.9	Landsat 5	TM	L5043033_03320080918
21-Sep-2009	120.1/38.9	Landsat 5	TM	L5043033_03320090921
24-Sep-2010	120.1/38.9	Landsat 5	TM	L5043033_03320100924
25-Sep-2005	-119.9/39.1	IKONOS	IKONOS-2	2005092519042390000010110092
27-Sep-2009	-119.9/39.1	IKONOS	IKONOS-2	2009092718555930000011612413

Appendix C: Salt Application Data

Table C.1. Average salt applied per mile on six major route sections (Yard^3/Mile)

Fiscal Year	US-50 DO	SR-28 DO	SR-28 CC	SR-28 WA	SR-207 DO	SR-431 WA	Grand Total
	13 (miles)	1.23	3.95	10.99	3.2	6.5	
1988-1989	20.7	19.0	12.4	13.0	32.4	40.3	21.8
1989-1990	16.3	22.1	10.2	3.8	15.7	6.5	10.5
1990-1991	24.8	39.2	17.9	12.8	25.3	32.8	22.4
1991-1992	21.8	28.6	12.9	9.8	14.9	33.5	18.9
1992-1993	49.0	49.9	34.5	26.5	35.7	42.3	38.4
1993-1994	34.4	36.4	26.2	22.1	18.6	35.0	28.6
1994-1995	41.4	108.9	36.5	19.2	41.3	90.3	44.2
1995-1996	28.9	88.8	40.4	22.5	38.0	50.4	33.9
1996-1997	18.4	33.7	19.7	20.6	23.5	35.7	23.0
1997-1998	38.0	61.7	23.5	17.7	34.5	43.3	31.9
1998-1999	40.5	75.3	37.3	22.9	22.2	37.7	34.1
1999-2000	24.5	26.0	7.7	8.1	16.9	23.0	17.1
2000-2001	30.3	38.8	9.1	6.5	23.6	23.1	19.6
2001-2002	23.4	24.9	9.5	16.2	11.8	24.7	19.0
2002-2003	12.7	22.8	7.0	3.1	12.5	16.6	10.2
2003-2004	11.3	13.6	4.6	5.3	8.0	16.0	9.4
2004-2005	16.4	13.4	5.1	6.9	9.3	16.5	11.7
2005-2006	14.9	13.9	2.3	5.7	11.3	24.3	12.1
2006-2007	7.0	10.9	4.0	6.2	16.3	13.7	8.3
2007-2008	20.8	37.8	9.8	12.8	15.7	13.9	16.2
2008-2009	19.8	17.8	10.9	13.4	23.0	25.1	18.1
2009-2010	28.7	46.1	23.0	22.9	48.9	31.8	28.8

Appendix D: Traffic Data

Table D.1. Mean Monthly Average Daily Traffic (*MADT*) in snowing season (November – April) from 1999 to 2009.

Year	SR-431	SR-28	US-50 Tahoe	US-50 Carson	MEAN
1999	8109	12104	28603	9100	14479
2000	8293	12115	29744	9610	14940
2001	8961	12246	28885	10119	15053
2002	9414	12299	29019	10753	15371
2003	9611	12149	29052	10760	15393
2004	9870	12147	29013	11225	15564
2005	9680	11765	29332	10866	15411
2006	9856	11469	28231	10412	14992
2007	10013	11377	27525	10352	14817
2008	9936	10882	26609	10401	14457
2009	9687	10100	24504	9753	13511

Appendix E: Weather Data

Table E.1. Precipitation (inch) per water year (Oct. to next Sep.) from 1988 to 2010.

Water Year	Mt. Rose	Marlette Lake	Heavenly Valley	MEAN
1988-1989	57	36.5	34	42.5
1989-1990	35.2	23.9	22.7	27.3
1990-1991	36.7	22.9	26.9	28.8
1991-1992	29	19.3	23.8	24.0
1992-1993	70.6	43	39.3	51.0
1993-1994	34	23	24.3	27.1
1994-1995	90.8	52.3	53.6	65.6
1995-1996	73.4	41.4	40.4	51.7
1996-1997	80.1	46	42.9	56.3
1997-1998	65.1	50.5	43.8	53.1
1998-1999	64.2	41.4	40.8	48.8
1999-2000	46.6	30.9	28.7	35.4
2000-2001	26.3	20	20.3	22.2
2001-2002	47.2	29.6	25.8	34.2
2002-2003	51.4	29.9	31.3	37.5
2003-2004	45.7	23.8	26.2	31.9
2004-2005	62	40.6	41.8	48.1
2005-2006	80.4	44.2	42.6	55.7
2006-2007	32.4	18.5	22.1	24.3
2007-2008	42.8	26.4	26	31.7
2008-2009	48	22.2	28.4	32.9
2009-2010	54.4	34.3	34.4	41.0

Appendix F: The Sun-Crown-Sensor + C Topographic Correction Result

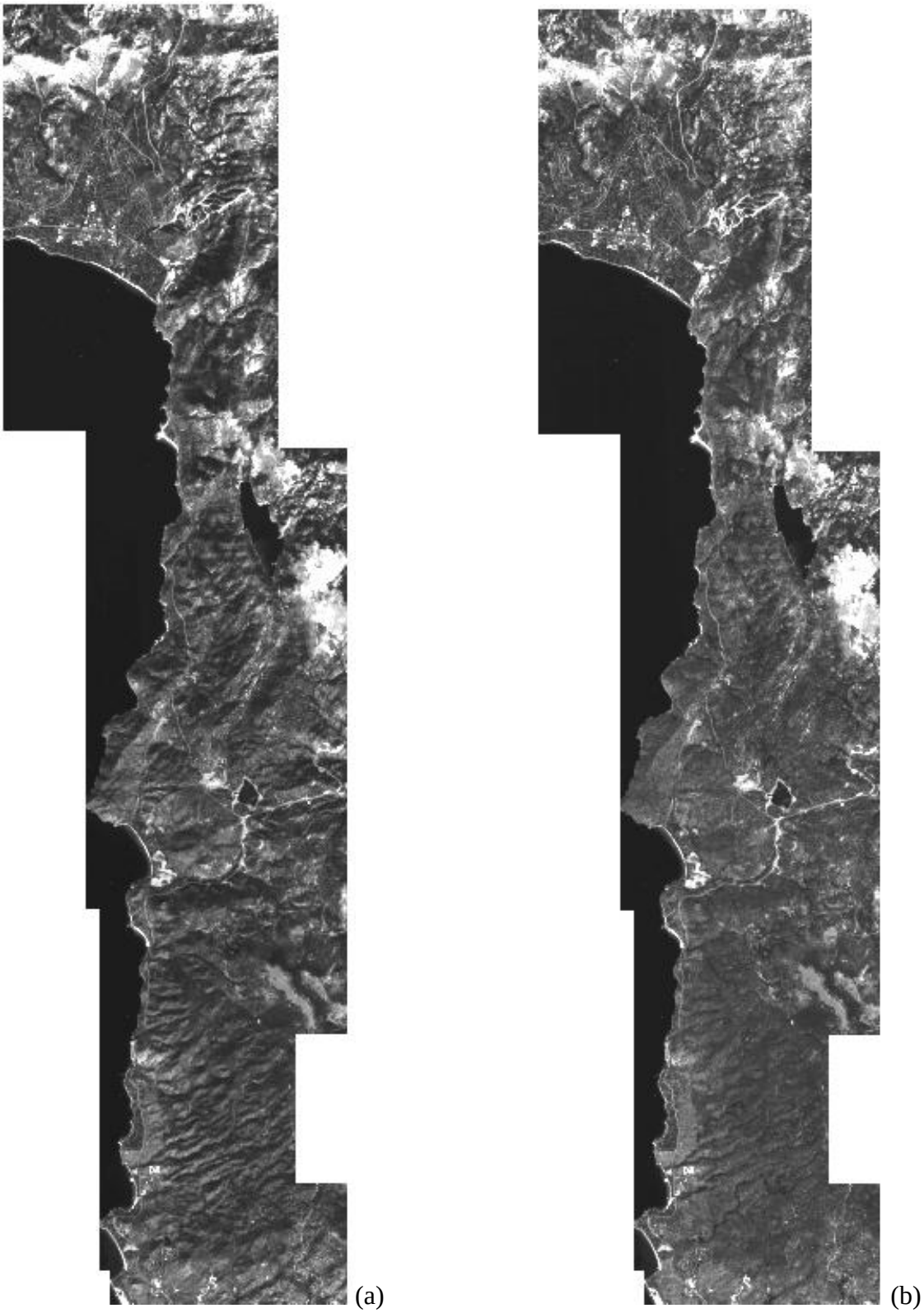

(a) (b)

Figure F. 1. The Sun-Crown-Sensor + C topographic correction on the red band of the 27 Sep. 2009 IKONOS image: (a) before correction, (b) after correction.

Nevada Department of Transportation
Rudy Malfabon, P.E. Director
Ken Chambers, Research Division Chief
(775) 888-7220
kchambers@dot.nv.gov
1263 South Stewart Street
Carson City, Nevada 89712